Evolution and Dynamical Processes of Solitary Precipitation Bands Within the Comma-Head of Northeast United States Cyclones

A Dissertation Presented

by

David Novak

to

The Graduate School

in Partial Fulfillment of the

Requirements

for the Degree of

Doctor of Philosophy

in

Marine and Atmospheric Science

Stony Brook University

August 2009

Stony Brook University

The Graduate School

David Novak

We, the dissertation committee for the above candidate for the

Doctor of Philosophy degree, hereby recommend

acceptance of this dissertation.

Dr. Brian A. Colle
Advisor
School of Marine and Atmospheric Sciences, Stony Brook University

Dr. Minghua Zhang
Chairperson, Professor, and Director of ITPA
School of Marine and Atmospheric Sciences, Stony Brook University

Dr. Edmund K. M. Chang
Professor
School of Marine and Atmospheric Sciences, Stony Brook University

Dr. Marvin A. Geller
Professor
School of Marine and Atmospheric Sciences, Stony Brook University

Dr. David Schultz
Professor
Finnish Meteorological Institute, Helsinki, Finland

This dissertation is accepted by the Graduate School

Lawrence Martin
Dean of the Graduate School

Abstract of the Dissertation

Evolution and Dynamical Processes of Solitary Precipitation Bands Within the Comma-Head of Northeast United States Cyclones

by

David Novak

Doctor of Philosophy

in

Marine and Atmospheric Science

Stony Brook University

2009

Intense solitary precipitation bands are frequently observed in the comma-head sector of extratropical cyclones. Limited observations and coarse resolution analyses have prohibited investigation of the mesoscale forcing and stability evolution during band life cycle in the past. This thesis uses unique Dual-Doppler observations, high-resolution analyses, model simulations, and Potential Vorticity (PV) inversions to explore the evolution and dynamical processes of solitary precipitation bands.

Analysis of 36 banded events through case study and composite approaches reveals a common cyclone evolution and associated band life cycle. A majority of banded events develop in the left-exit region of an upper jet, in an area of concentrated upper-PV advection along the poleward edge of an upper PV hook. Band formation occurs as midlevel frontogenesis rapidly increases along a mesoscale trough that extends poleward of the 700-hPa low. This trough is the vertical extension of the surface warm-occlusion.

At the same time, conditional stability near 500 hPa is reduced due to differential horizontal temperature advection in moist southwest flow ahead of the approaching upper trough. The high-resolution analyses show that although conditional, conditional symmetric, and inertial instabilities may be present, shallow layers of conditional instability are present more often during band formation than layers of conditional symmetric instability, contrary to previous research using coarser analyses. Band maturity is marked by increasing conditional stability, which is offset by an increase in frontogenetical forcing. Model simulations with varying degrees of latent heating reveal that latent heating associated with the band itself is critical to the development and maintenance of the frontogenetical forcing for the band. Band dissipation occurs as the frontogenesis weakens and the conditional stability is restored. PV inversions show that the band is susceptible to changes in the meso-α scale flow associated with the formation of diabatic PV anomalies east of the band, which contribute to frontolysis and band dissipation.

A set of 22 null events where single band formation was absent in the comma-head were examined. Although exhibiting similar synoptic patterns, null events were characterized by weaker frontogenesis, larger conditional and symmetric stability, and less coupling with upper-level forcing for ascent.

Table of Contents

List of Figures

Chapter 1 **Page**

Chapter 2

Chapter 3

Chapter 4

List of Tables

Chapter 2

Chapter 3

Chapter 4

Acknowledgements

I would like to thank my advisor, Dr. Brian A. Colle, for his guidance, teaching, and many motivating discussions. I would like to thank Dr. David Schultz for serving as the external member on my dissertation committee and for a thorough review of my dissertation with many important suggestions for improvement. I thank Dr. Sandra Yuter (North Carolina State University) for providing WSR-88D dual-Doppler synthesis data. I would also like to thank my internal committee members Dr. Edmund Chang, Dr. Marvin Geller, and Dr. Minghua Zhang for their reviews of my dissertation, suggestions for improvement, and for teaching me the dynamics of the oceans and atmosphere.

I would also like to thank my colleagues, friends, and family who have encouraged me in times of hardship and celebrated with me in times of success. Finally, I want to express my deep appreciation for my wife, Elizabeth, who first encouraged me to pursue a Ph.D, and has been with me every step of the way.

Chapter I:

Introduction

1.1 Background

Understanding the physical processes responsible for mesoscale precipitation systems and their predictability is a key research objective for improving cool-season quantitative precipitation forecasts (QPF) (Ralph et al. 2005). Meso-β scale precipitation bands resulting from frontal circulations have proven difficult to forecast (Weismuller and Zubrick 1998; Nicosia and Grumm 1999), because most operational models do not have adequate grid spacing to explicitly resolve these bands, and uncertainties in model physics and initial conditions limit their predictability. Precipitation bands have dramatic effects on the intensity, timing, and subsequent accumulation of precipitation, especially during the cool season, when the occurrence of snowbands often results in intense snowfall and extreme snowfall gradients (Kocin and Uccellini 2004, 177–186). Therefore, improved understanding of the evolution and dynamical processes of mesoscale bands can advance cool-season QPF skill.

The northeast United States (U.S.) is an attractive region for studying mesoscale bands, since intense bands associated with cyclones frequently occur in this region during the cool season (Novak et al. 2004). Furthermore, the northeast U.S. observational network includes Doppler radars (Klazura and Imy 1993), aircraft soundings (Moninger et al. 2003), integrated precipitable water vapor sensors (Gutman et al. 2004), and wind profilers (Stensrud et al. 2006). Such observational assets facilitate analysis and model validation of banded features.

This thesis uses the unique high-resolution observations of the northeast U.S. in concert with high-resolution gridded analyses and model simulations to explore the evolution and dynamical processes of solitary precipitation bands in the comma-head region of developing extratropical cyclones. The remaining portion of this chapter reviews mesoscale band types, band processes, and band prediction, and outlines the study goals and approach.

a. Mesoscale band types

Although the banded nature of precipitation within extratropical cyclones was recognized as early as the 1920s with the advent of the Norwegian cyclone model (Bjerknes and Solberg 1922), bands on scales less than 100 km in width were not documented until observational (radar) capabilities improved in the 1950s-60s (e.g., Knettner 1959; Elliott and Hovind 1964). The Cyclonic Extratropical Storms (CYCLES) project used radar, aircraft, sounding, and precipitation observations to survey the mesoscale structure of rainfall in 11 occluded cyclones affecting western Washington state (Houze et al. 1976; Hobbs et al. 1980). Six types of mesoscale bands were defined by Houze et al. (1976):

> *"Warm frontal*. Bands approximately 50 km in width oriented parallel to the warm front and found toward the leading edge of a frontal cloud shield.
>
> *Warm sector*. Bands typically 50 km in width, found south of the intersection of the surface warm and cold fronts and tending to be parallel to cold fronts.
>
> *Cold frontal: wide*. Bands approximately 50 km in width oriented parallel to the cold front and found toward the trailing edge of a frontal cloud shield.
>
> *Cold frontal: narrow*. Extremely narrow band (~5 km in width) coinciding with surface cold front.
>
> *Wave*. Bands occurring in a very regular pattern similar to waves, typically 10-20 km wide.
>
> *Post frontal*. Rainbands located in the convective cloud field behind a frontal cloud shield."

Hobbs (1978) subsequently developed a schematic which placed these bands relative to surface fronts and surface cyclone positions (Fig.1.1).

Elaborating on the band classification scheme of Houze et al. (1976), Hobbs (1978) summarized the dynamical and microphysical structures associated with the different types of rainbands. Narrow cold frontal bands were found along the immediate cold frontal zone, associated with boundary layer convergence along the leading edge of the front. Wide cold frontal bands were found behind the surface cold front in a convectively stable environment. In contrast, warm sector rainbands were found to be convective, generally propagating away from the surface cold front. Hobbs (1978) additionally identified prefrontal cold-surge bands as being associated with pulses of cold air ahead of the primary cold front in an occlusion. This feature would later be termed a Cold Front Aloft (CFA) by Hobbs (1990).

Novak et al. (2004) provided a band classification scheme and band climatology for the northeast U.S using radar data over five cool seasons (1996–2001). Although bands were observed ahead of the surface cyclone and associated surface fronts as in Houze et al. (1976), a band was more frequently observed in the comma-head portion of a developing cyclone not directly associated with any surface front (Novak et al. 2004, their Table 2). These bands were termed "single bands." The single-banded structure was defined as a linear radar reflectivity feature 20–100 km in width and greater than 250 km in length, which maintains a minimum intensity of 30 dBZ along a majority of its length for at least 2 h. An example of the single-banded structure is shown in Fig. 1.2. This structure may locally exhibit multi-banded features that merge into a single dominant band axis (Novak et al. 2004). Novak et al. (2004) found ~7 single-banded events in the comma-heads of northeast U.S. cyclones (their northwest class) per season. The single-banded structure has also been observed in Atlantic Canada (Reuter and Yau 1990; Stewart 1991), and the central U.S. (Martin 1998a,b; Moore et al. 2005), and it is the primary focus of this work.

The single band is most similar in description to warm frontal bands, as they have similar scales, both are aligned nearly parallel to the thermal wind, and both occur on the cold side of a frontal boundary. Indeed, 19% of the single bands identified by Novak et.

al. (2004) were found in the eastern quadrant of the cyclone, consistent with the warm frontal band location (i.e., Fig. 1.1). However, Novak et al. (2004) note a slow pivoting motion with many single-banded events in the comma head, while warm frontal bands have a motion associated with the cloud-layer wind (Hobbs 1978, p754). Thus the primary descriptive distinctions between the single bands studied here and the warm frontal bands described by Houze et al. (1976) are their typical movements and locations within the cyclone.

b. Band processes

The radar, thermodynamic, and kinematic observations of the CYCLES project afforded opportunity to explore processes responsible for mesoscale bands. Initial work focused on kinematic and microphysical aspects of the band types, associating bands with the development of shallow convective elements, termed “generating cells” (e.g., Wexler and Atlas 1959; Hobbs 1978), and subsequent ice crystal fall out and growth due to deposition and aggregation in the presence of a mesoscale updraft (Rutledge and Hobbs 1983). This process is shown schematically for a warm frontal rainband in Fig. 1.3).

A key question raised by the CYCLES work was what physical processes were responsible for the mesoscale updraft, especially for bands occurring behind the cold front, ahead of the warm front, or in the occluded quadrant of cyclones where the environment is often stable to upright convection. Theoretical work by Emanuel (1985), Thorpe and Emanuel (1985), Xu (1989a,b), and Xu (1992) showed that intense single cores of ascent can form through a coupled relationship between frontogenesis and moist symmetric stability, whereby the ascending branch of a frontal circulation is dramatically narrowed and enhanced when there is weak moist symmetric stability on the warm side of a frontal boundary. For example, in an idealized study using a viscous semigeostrophic model, Xu (1992) showed that a single narrow ascent core is simulated when small symmetric stability [measured in terms of small saturation equivalent potential vorticity [EPV; Hoskins (1974); Schultz and Schumacher (1999, p. 2715)] is present on the warm side of a sloping axis of frontogenesis (Fig. 1.4a). Xu (1992) also showed that when the symmetric stability is further reduced, the ascent core breaks into multiple intense ascent cores (Fig. 1.4b). Idealized experiments by Xu (1989a,b) suggest that the distinction between single and multiple bands is dependent not only on the magnitude of negative EPV, but also the magnitude and areal extent of the frontogenesis, the eddy viscosity, and sufficient moisture.

Recent observational studies of single band formation have highlighted synoptic environments which support the band “ingredients” of frontogenesis, weak moist symmetric stability, and sufficient moisture. In a study of three northeast U.S. snowstorms Nicosia and Grumm (1999) showed that midlevel deformation north of the developing midlevel cyclone contributed to strong frontogenesis, coincident with the observed single-banded structures (Fig. 1.5a). Similarly, Novak et al. (2004) found single-band formation to be associated with cyclogenesis, as the development of a closed midlevel circulation supported deformation and associated frontogenesis to the northwest of the surface cyclone (Fig. 1.5b) – a frontogenesis location favored for cyclones in large-scale diffluent flow (Schultz et al. 1998). These results are also consistent with the case study work of Martin (1998a,b), Banacos (2003), and Moore et al. (2005), who have documented deformation and frontogenesis in the comma-head sector of central U.S. cyclones (Fig. 1.5c) associated with the cyclonically turning portion of the warm conveyor belt (Carlson 1980; Schultz 2001), or alternatively the trough of warm air aloft (trowal) airstream (Martin 1998a,b; Grim et al. 2007; Han et al. 2007). Observational studies have also shown that bands tend to form where a layer of weak moist symmetric stability lies just above the frontogenesis maximum (e.g., Trapp et al. 2001; Novak et al. 2004), as depicted in Fig. 1.5d. These results highlight band formation associated with the coupling of frontogenetical forcing with weak moist symmetric stability.

Although a basic understanding of the fundamental processes responsible for band formation within the comma-head portion of cyclones has been established, questions remain concerning how changes in forcing, stability, and moisture relate to band life cycle. For example, band dissipation has been hypothesized to be a consequence of increasing symmetric stability (Nicosia and Grumm 1999), and weakening forcing for ascent (Novak et al. 2004); however, the limited temporal and spatial resolution of past studies has precluded testing these hypotheses. There is also limited knowledge of the three-dimensional band structure and its evolution. For instance, previous studies have stated that bands form on the warm side of a midlevel frontogenesis maximum (Sanders and Bosart 1985; Jurewicz and Evans 2004; Moore et al. 2005; see also Fig. 1.5c). These statements are supported by idealized frontal studies employing the Sawyer–Eliassen equation (Sawyer 1956; Eliassen 1962), which show the strongest ascent 50–200 km to the warm side of the frontogenesis maximum (e.g., Emanuel 1985; Thorpe and Emanuel 1985; Xu 1992). However, these studies have used frontogenetical forcing maximized near the surface (Thorpe and Emanuel 1985; Xu 1992), without a slope (Emanuel 1985), or at a point (Hakim and Keyser 2001), whereas observed frontal zones often exhibit a deep (300–400-hPa) sloping layer of frontogenesis.. Additionally, meso-gamma scale processes such as hydrometeor advection may shift the precipitation band relative to the frontogenesis maximum. High-resolution observations and model simulations could improve our understanding of the evolution of cool-season mesoscale bands.

Moist processes, in particular latent heat release (LHR), are critical to cyclone development (e.g., Reed and Kuo 1988; Davis 1992; Stoelinga 1996), and such processes may also be critical to band evolution. For example, Han et al. (2007) demonstrated in the modeling of two central U.S. cases that the frontogenetical forcing for ascent due to diabatic processes within the trowal (e.g., Godson 1951; Martin 1998a,b) was at least twice as large as horizontal deformation. In a potential vorticity (PV) perspective, occluded cyclones often exhibit a PV “hook” (Martin 1999; Thorncroft et al. 1993). This PV distribution supports large-scale forcing for ascent in the occluded quadrant of the cyclone through rotation of the lower-tropospheric baroclinic zone (i.e., rotational frontogenesis) (Martin 1999; Posselt and Martin 2004). Posselt and Martin (2004) showed that LHR in the northwest quadrant of the cyclone enhances development of the PV hook through the diabatic redistribution of PV (Fig. 1.6). In this process PV is generated (diluted) below (above) the level of maximum heating due to associated changes in stability and vorticity (Fig. 1.7, see also Raymond 1992). Posselt and Martin (2004) focused on the upper-level diabatic dilution of PV, but diabatically-generated PV anomalies at lower levels would be present (as in Fig. 1.7). Indeed, diabatically-generated PV anomalies are common features of extratropical cyclones (e.g., Davis 1992; Stoelinga 1996; Wernli et al. 2002; Moore and Montgomery 2004), and they may affect the mesoscale precipitation distribution (e.g., Brennan and Lackmann 2005; Moore et al. 2008). Thus it is important to understand the relation of the evolution of upper-level and diabatically-generated PV anomalies to the evolution of the band.

On the frontal scale, idealized studies have shown that LHR from a precipitation band may influence the band's formation and evolution (Thorpe and Emanuel 1985; Cho and Chan 1991; Xu 1992; Davies 1999). The diabatically-generated PV anomalies created by the band may induce a horizontal circulation (Hoskins et al. 1985; see also Fig. 1.7) that may be frontogenetical. Although this feedback is presumably active within a snowband of an extratropical cyclone, the role of the band's latent heating on its own evolution has not been quantified. It is also not apparent if or how this feedback is disrupted during band dissipation.

The vertical and horizontal distribution of moisture may also play a critical role in band evolution by its modification of the stability. Conceptual models of the synoptic environment of band formation by Nicosia and Grumm (1999) and Moore et al. (2005) (Figs. 1.5a and 1.5c, respectively) have highlighted a region of EPV reduction southeast of the frontogenesis maximum and associated band, in a layer associated with the midlevel dry slot. This location is consistent with the results of Cao and Cho (1995) and Cho and Cao (1998), who showed that negative EPV can be generated in regions where the thermal wind vector points in the same direction as the moisture gradient. However, banding events can occur well displaced (>200 km) from the dry slot, or form hours before a robust dry slot develops (Clark et al. 2002). Thus, it is unclear if the dry slot is even relevant to band formation, and if not, how the stability is reduced.

Although band formation is generally associated with weak moist symmetric stability, instabilities such as Conditional Symmetric Instability (CSI; Bennetts and Hoskins 1979; Schultz and Schumacher 1999), conditional instability (CI), and inertial instability (II) may be present (e.g., Jurewicz and Evans 2004; Schultz and Knox 2005; Morales 2008). Additionally, multiple instabilities may coexist, as discussed by Bennetts and Sharp (1982), Schultz and Schumacher (1999, section 5), Jascourt et al. (1988), and Schultz and Knox (2005). To date, the spectrum of instabilities present during band evolution has not been quantified.

c. Band prediction

The advent of high-resolution modeling provides an opportunity to explore the structural and dynamical evolution of a mesoscale band on scales not readily observed. High-resolution modeling of observed mesoscale banding events in the comma-head portion of cyclones has been rare (e.g., Baxter and Graves 2006; Han et al. 2007). Past modeling studies exploring the evolution of frontogenesis (Moore et al. 2005; Han et al. 2007), stability reduction (Cao and Cho 1995; Nicosia and Grumm 1999; Clark et al. 2002), and moisture sources (Moore et al. 2005) in the comma head portion of cyclones have used horizontal grid spacing coarser than 25 km. At these coarse resolutions the mesoscale forcing may not be fully resolved, and the ability of a model to simulate the release of moist symmetric instability is compromised (Knight and Hobbs 1988; Persson and Warner 1993; Schultz and Schumacher 1999). Also, these resolutions are not sufficient to resolve sharp gradients in moisture observed within the warm-frontal region of cyclones (e.g., Grim et al. 2007). Thus, the first sub-5 km grid spacing simulation of a real banded case will be attempted in this thesis to examine the structure and evolution of a mesoscale band.

Distinguishing between cases that exhibit heavy precipitation in the comma-head not organized into a narrow band, versus those that exhibit single banding is an operational forecast challenge. Novak et al. (2004) showed that cases in which a midlevel closed low fails to form do not have banding in the comma-head, given the limited deformation and frontogenesis in this sector of the cyclone. However, not all cases that form a closed midlevel low develop bands in the comma-head. Greenstein et al. (2006) studied precipitation patterns of 20 heavy snow cases in the northeast U.S. during the 2002–2005 cool seasons using mosaic radar data and the North American Regional Reanalysis (NARR; Mesinger et al. 2006). Although not explicitly restricted to the comma-head region, Greenstein (2006) found that single-banded events (his “classic” type) had stronger and deeper frontogenesis and weaker conditional stability than events exhibiting more uniform reflectivity shields. Whether this finding can be shown for a larger set of cases with higher spatial and temporal resolution data is unknown. Thus, investigation of cases that form a closed midlevel low but fail to develop a band is needed.

1.2 Study goals and approach

This study will utilize high-resolution observational and modeling capabilities to explore the evolution and dynamical processes of solitary precipitation bands. Specific questions addressed in this thesis are:

(1) What is the observed structure and evolution of a band during its life cycle?
(2) How does the frontogenesis, stability, and moisture change during band life cycle?
(3) What processes regulate the evolution of the midlevel frontogenesis and stability during band life cycle?
(4) What influence does latent heating associated with the band have on band evolution?
(5) Can a high-resolution model simulate the structure and evolution of an intense band?
(6) How does the frontogenesis and stability evolution differ between cyclones with closed midlevel circulations that develop bands and those cyclones that do not?
(7) What is the spectrum of cyclone types that produce intense single bands?

The thesis is composed of three components. The first component aims to improve our understanding of the structure and evolution of single-banded events using high-resolution observations and model simulations of the 25 December 2002 snowstorm (chapter 2). The second component investigates the role of moist processes in regulating mesoscale snowband life-cycle in the 25 Dec 2002 snowstorm and two additional northeast U.S. cyclones using piecewise potential vorticity (PV) inversion, modeling experiments, and potential temperature tendency budgets (chapter 3). The third component draws on a dataset of 36 banded events and 22 nonbanded (null) events to generalize the case study results through climatological and composite techniques (chapter 4). A discussion and synthesis of the key results and suggested future work is provided in chapter 5.

Figures

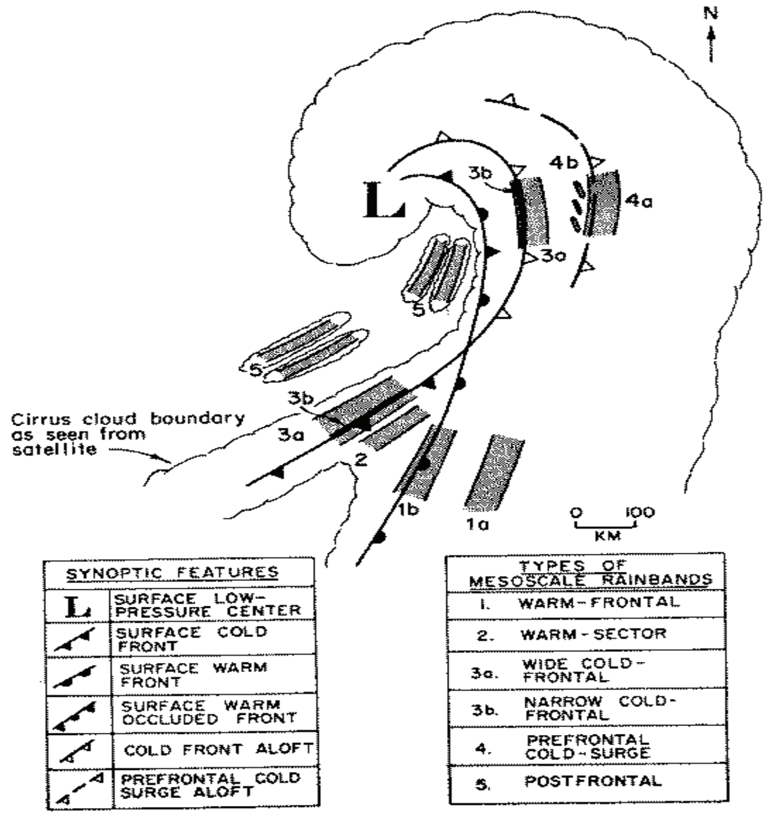

Figure 1.1 Schematic from Hobbs (1978, Fig. 6) illustrating the types of bands and their locations observed during a study of 11 Pacific Northwest cyclones.

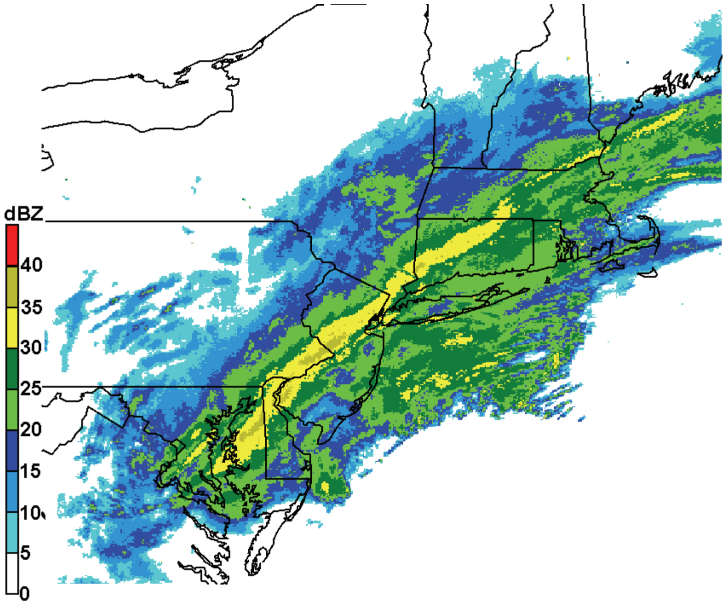

Figure 1.2 WSR-88D radar mosaic (reflectivity shaded according to scale) valid 1200 UTC 12 February 2006, showing an intense single band over the northeast U.S.

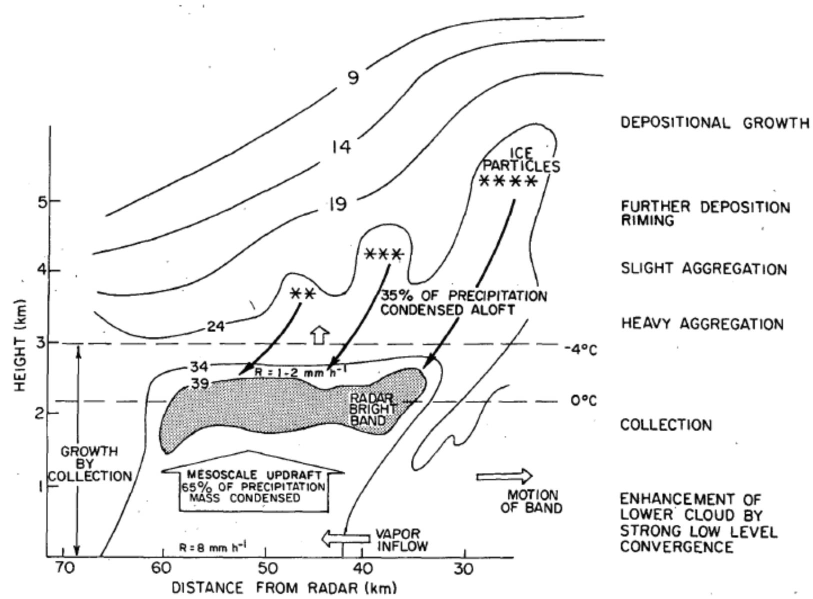

Fig. 1.3. Schematic illustration of the microphysical precipitation processes associated with the warm-frontal rainband studied by Houze et al. (1980). Reflectivity contoured (solid) every 5 dBZ. [Adopted from Houze et al. (1980, Fig. 8).]

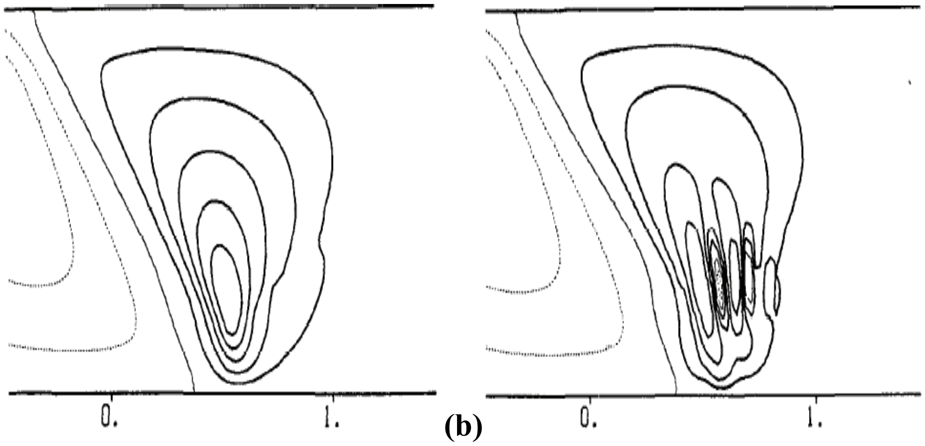

(a) **(b)**

Figure 1.4 (a) Cross section of vertical velocity (positive solid, drawn with power increasing intervals ±2^n x 0.5 cm s^{-1}) from a simulation with geostrophic frontogenesis forcing maximized approximately along the zero contour and small symmetric stability on the lower right side of cross section. (b) As in (a), except with reduced symmetric stability. [From Xu's (1992, Figs. 2a and 6a) cases I and II.]

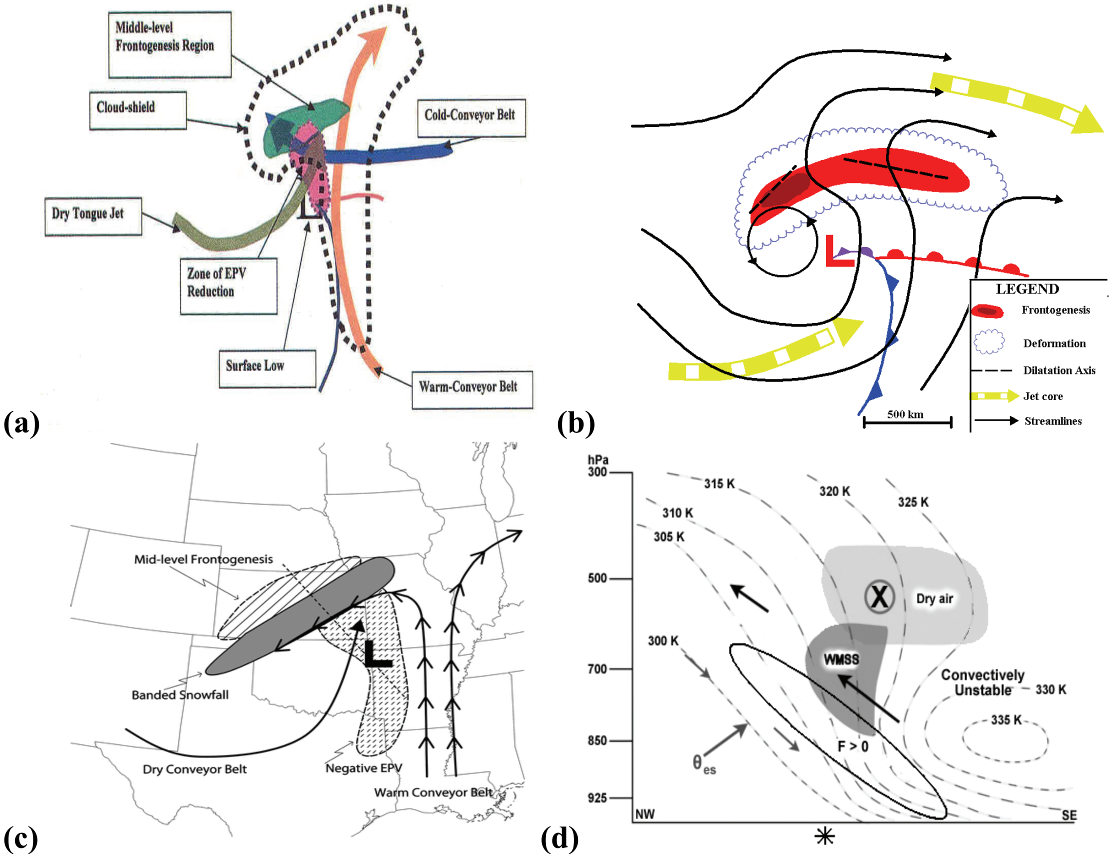

Figure 1.5 Schematics of the synoptic and mesoscale environment conducive to band formation from (a) Nicosia and Grumm (1999, Fig. 17), (b) Novak et al. (2004, Fig. 15a), and (c) Moore et al. (2005, Fig. 15a). (d) Cross section depiction of the mesoscale band environment as shown in Novak et al. (2006, Fig. 2), where 'WMSS' refers to weak moist symmetric stability.

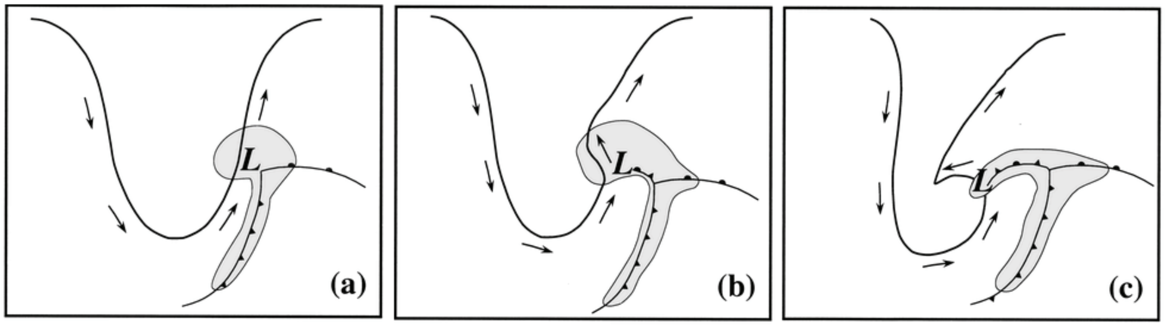

Figure 1.6 Schematic illustrating the synergy between diabatic dilution of PV and negative advection of PV at the tropopause for the (a) open wave stage, (b) occluding stage, and (c) mature occlusion stage. Gray shading represents the dilution of tropopause PV by diabatic heating. Thick solid line represents the PV = 2 PVU (where 1 PVU = 10^{-6} K m^2 kg^{-1} s^{-1}) isertel at the tropopause, and arrows represent the tropopause-level flow. [Adapted from Posselt and Martin (2004, Fig. 14).]

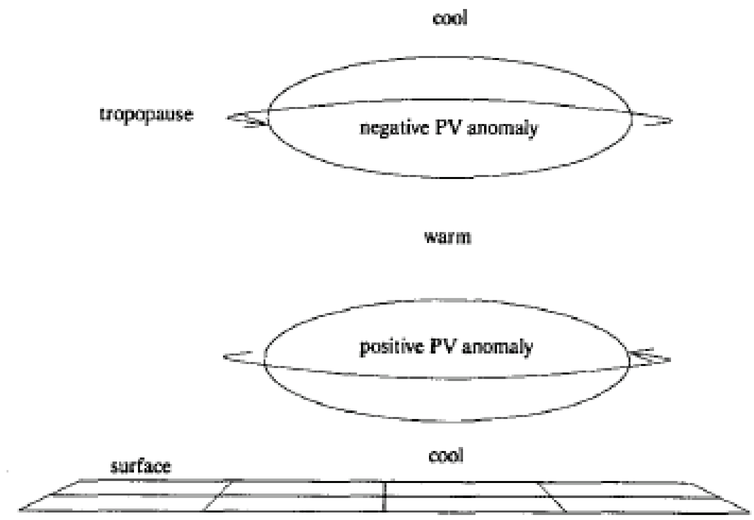

Figure 1.7 Sketch of the structure of potential vorticity anomalies produced by a region of convection and associated changes in temperature and wind structure. [From Raymond and Jiang (1990, Fig. 1)].

Chapter II:

High-Resolution Observations and Model Simulations of the Life Cycle of an Intense Mesoscale Snowband

2.1 Introduction

This chapter presents high-resolution observations and model simulations of the 25 December 2002 snowstorm. Dual-Doppler, wind profiler, commercial aircraft, and integrated precipitable water vapor observations in concert with model simulations down to 1.33-km grid spacing will be used to investigate the structural and dynamical evolution of an intense mesoscale snowband. These datasets will be used to highlight aspects of band structure and dynamics unresolved by previous studies, including the development of a sharp midlevel trough during band formation, an unconventional location of the band relative to the frontogenesis maximum, and the presence of increasing stability during the band formation process. The availability of high-resolution observations and model simulations further allow the diagnosis of model error in this case.

The mesoscale snowband studied in this chapter occurred 25–26 December 2002 over central and eastern New York. Storm total snowfall accumulations exceeded 90 cm in some locations, with much of this snow falling during a 6-h period associated with the formation of an intense mesoscale snowband. Operational forecast aspects of this case are reviewed in Novak et al. (2006) and Stuart and Grumm (2006).

The objectives of this chapter are to (1) describe the observed structural evolution of the band during its life cycle, (2) examine how the frontogenesis, stability, and moisture change during band life cycle in this case, and (3) verify the simulated mesoscale flow and precipitation evolution using comprehensive observational datasets.

Section 2.2 describes the observational datasets and modeling configuration used in the study. Section 2.3 presents a multi-scale overview of the case, and section 2.4 focuses specifically on the band life cycle with particular emphasis placed on the evolution of frontogenesis and stability. Section 2.5 explores changes in moisture availability during the banded event, and a summary and discussion is provided in section 2.6.

2.2 Datasets and methodology

a. Observational datasets

The conventional surface and upper-air observation network was supplemented with Doppler radar, wind profiler, commercial aircraft, and ground-based integrated precipitable water vapor (IPW) observations (Fig. 2.1a) to better depict the structural and dynamical evolution of the 25–26 December 2002 banded event, and verify model forecasts.

Reflectivity and radial velocity data was obtained from Weather Surveillance Radar-1988 Doppler (WSR-88D) radar sites in the northeast United States. These radars (Fig. 2.1a) provided 9 elevation slices with a beam width of 1° and bin length of 1 km (0.25 km for velocity data; Klazura and Imy 1993). The WSR-88D velocity azimuth display wind profile (VWP) product (Klazura and Imy 1993, their Fig. 12) was used to determine wind profiles at the WSR-88D radar sites.

The relative close proximity of the Binghamton, New York (KBGM) and Albany, New York (KENX) radar sites to each other (165 km) allowed for dual-Doppler synthesis, following the methodology of Yuter and Houze (1995). The WSR-88D polar radar data from KBGM and KENX were interpolated to a common Cartesian grid at 2-km horizontal and 1-km vertical resolution. The wind field was computed up to a height of 10 km MSL within dual-Doppler lobes over eastern New York (Fig. 2.1a) using Custom Editing and Display of Reduced Information in the Cartesian Space (CEDRIC; Mohr et al. 1986). A two-step Leise filter (Leise 1982) was applied to eliminate wavelengths less than 8 km. Unfortunately, the relatively coarse vertical resolution of the WSR-88D scans prohibited acquisition of reliable vertical velocity magnitudes.

Additional wind observations were obtained from commercial aircraft (Moninger et al. 2003) and several 915-MHz boundary layer wind profilers (Fig. 2.1a) operating as part of the New England High-Resolution Temperature Program (Stensrud et al. 2006). Ground-based IPW retrievals (Gutman et al. 2004) from four stations near the banded event (Fig. 2.1a) were also available to aid verification of the model moisture fields.

Analyses from the Rapid Update Cycle (RUC; Benjamin et al. 2004) and National Centers for Environmental Prediction (NCEP) Eta Data Assimilation System (EDAS; Rogers et al. 2001) were compared to observations to determine the most representative analyses. This investigation found that the EDAS analyses were superior to the RUC analyses for this particular case, with a better match of the wind profiler, aircraft, and radar-derived winds near the band. This behavior may be expected given the smaller grid spacing of the EDAS (12 km) compared to the RUC (20 km) and the more sophisticated analysis scheme used in the EDAS (3D Var) as compared to the RUC (Optimum Interpolation) at the time of this case (S. Benjamin 2006, personal communication). Therefore, EDAS analyses and Eta 3-h forecasts will be shown in this study, with both referred to as the analysis.

b. Model configurations

Model simulations of the 25–26 December 2002 banded event were run using the fifth-generation Pennsylvania State University–National Center for Atmospheric Research (NCAR) Mesoscale Model (MM5; version 3.4) (Dudhia 1993) and Weather Research and Forecasting (WRF; version 2.0.3) (Michalakes et al. 2001) model. The simulations were run using an outer 36-km domain covering the eastern two-thirds of the U. S. and adjacent coastal waters, and 12-, 4-, and 1.33-km nested (one way) domains centered on the banding location over eastern New York (Fig. 2.1b). Thirty-three sigma levels were used in the vertical, with maximum resolution in the boundary layer. The model top was set at 100-hPa. Model terrain was analyzed for the 36-, /12-, 4-, and 1.33-

km grids from a 5’ and 30” terrain dataset, respectively, using a Cressman analysis scheme, and filtered by a two-pass smoother–desmoother. Terrain from the 4 km model domain is shown in Fig. 2.1b. A 30” land use dataset from NCAR was used to initialize 25 surface categories for all domains. The 4- and 1.33-km nests were run without convective parameterization.

The MM5 and WRF models were initialized with the 0000 UTC 25 December 2002 EDAS analysis, interpolated to the NCEP-221 grid (32-km horizontal resolution, 25-hPa vertical resolution). To explore whether mesoscale models are capable of predicting snowbands, the 0000 UTC 25 December 2002 Eta forecast (as opposed to a series of analyses) was used for boundary conditions. The boundary conditions were obtained by linearly interpolating the Eta forecast at 3 h intervals on the NCEP-104 grid (90-km horizontal resolution, 25-hPa vertical resolution). The U.S. Navy Optimum Thermal Interpolation System (OTIS) sea surface temperature analyses (~30 km horizontal resolution) were used to initialize the model surface temperatures over water.

The sensitivity of band formation and evolution to model physics schemes was investigated by varying the convective, boundary layer, and microphysics schemes in both the MM5 and WRF. The solutions clustered primarily by model type, with the WRF simulations providing a more accurate forecast of the surface cyclone central pressure and precipitation maximum than the MM5 simulations. However, the forecast banded event in the WRF simulations was composed of two short-lived (2-h duration) bands, which were not observed. Also, the bands and associated precipitation maxima in the WRF simulations were displaced ~200 km south of the observed maximum (Novak and Colle 2005). Thus the MM5 simulations were preferred. Differences of band characteristics between MM5 forecasts using different physics schemes were small, with storm total precipitation differences generally ranging less than 5 mm in the banding region; however, it was concluded that the Grell convective parameterization (Grell 1993), NCEP Medium-Range Forecast (MRF) boundary layer scheme (Hong and Pan 1996), and simple ice microphysics (Dudhia 1989; Hong et al. 2004) gave the most realistic simulation of band life cycle. Results from this simulation are discussed in the subsequent sections of this paper.

c. Calculations

The Petterssen (1936) 2D frontogenesis equation,

$$\mathrm{F}_{2\mathrm{D}} = \frac{1}{|\nabla\theta|}\left[-\frac{\partial\theta}{\partial x}\left(\frac{\partial u}{\partial x}\frac{\partial\theta}{\partial x}+\frac{\partial v}{\partial x}\frac{\partial\theta}{\partial y}\right)-\frac{\partial\theta}{\partial y}\left(\frac{\partial u}{\partial y}\frac{\partial\theta}{\partial x}+\frac{\partial v}{\partial y}\frac{\partial\theta}{\partial y}\right)\right], \qquad (2.1)$$

is used to assess frontal forcing for ascent. The magnitude of (2.1) is identical to the magnitude of the across-isentropic component of the Q-vector, Q_n, when the geostrophic wind is substituted (Keyser et al. 1992; Martin 1999). Given the mesoscale nature of the problem in this work, the full wind will be used in calculating frontogenesis.

Moist symmetric stability is assessed through calculation of the saturation equivalent potential vorticity (EPV), defined as:

$$EPV = g\eta \bullet \nabla\theta_{es} \qquad (2.2),$$

where g is gravity, η is the three-dimensional absolute vorticity vector and $\nabla\theta_e$ is the three-dimensional gradient of saturation equivalent potential temperature. Following

Novak et al. (2004), the full wind will be used in calculating EPV since the full wind is likely to be more representative than the geostrophic wind in evaluating moist symmetric stability in the sharply curved flow environments of bands in northeast U.S. cyclones.

2.3 Case Overview

a. Synoptic scale evolution

Cyclone development during the 25–26 December 2002 banded event was similar to a Miller type-B cyclogenesis event (Miller 1946), which is characterized by coastal redevelopment of a surface cyclone as a 500-hPa trough approaches the eastern United States. At 1200 UTC 25 December 2002 (hereafter, times will be abbreviated "time UTC/day"—1200/25 in this circumstance), a deep 500-hPa trough was present over the eastern U.S, with a short-wave evident in the satellite imagery over the southeast United States. (Fig. 2.2a). A 75 m s^{-1} jet at 300 hPa was found at the base of the 500-hPa trough, and a 50 m s^{-1} jet was found in the downstream confluent zone over southeast Canada (Fig. 2.2a). This is a common jet configuration for major northeast U.S. cyclogenesis events (Kocin and Uccellini 2004, 117–120). Surface cyclogenesis was occurring along the Virginia coast (Fig. 2.3a) in the diffluent exit region of the southern jet, southeast of the parent surface cyclone over eastern Ohio. The MM5 12-h forecast largely predicted these features, although the analyzed 500-hPa trough was ~10 m deeper than forecast (cf. Fig. 2.2a and Fig. 2.2b) and coastal surface development was underpredicted by 2 hPa (cf. Figs. 2.3a,b).

By 1800/25, rapid cyclogenesis had occurred along the New Jersey coast under the poleward exit region of the 300-hPa jet streak and just ahead of the 500-hPa short wave trough (Figs. 2.2c and 2.3c). The surface cyclone had developed a warm occlusion frontal structure, and deepened from 995 hPa at 1200/25 (Fig. 2.3a) to 979 hPa at 1800/25 (Fig. 2.3c). Common cyclogenesis features were evident in the observed and simulated cloud patterns at this time, including the emergence of a comma head over New York and Pennsylvania and dry slot near the southern New Jersey coast (Figs. 2.2c,d). Although the MM5 forecast exhibited a nearly identical position of the short-wave trough and attendant 300-hPa jet, the analyzed trough was ~30 m deeper and the jet ~ 5 m s^{-1} slower (cf. Figs. 2.2c,d). These errors translated into a ~7 hPa underprediction of the surface cyclone (cf. Figs. 2.3c,d).

By 0000/26, the surface cyclone had deepened to 973-hPa (Fig. 2.3e), but had become nearly vertically aligned with the 500-hPa cyclone (Fig. 2.2e), limiting further development. A well-defined comma head and dry slot were evident in satellite imagery at this time over New York and Connecticut, respectively (Fig. 2.2e). The MM5 forecast exhibited a similar cloud pattern (Fig. 2.2f); however, the MM5 underforecast the cyclone development, with a 60 m and 9-hPa underprediction of the 500-hPa and surface cyclone, respectively (Figs. 2.2f and 2.3f). Despite this cyclone intensity error, the MM5 predicted a realistic band evolution as described below.

b. Mesoscale evolution

The analyzed mesoscale evolution of the 25–26 December 2002 banded event featured the formation of a 700-hPa low over eastern Pennsylvania by 1800/25 (Fig. 2.4a), and the development of a sharp trough extending northeast from this low center into southern New Hampshire. This trough formed between 1500–1800/25 over New

Jersey and southern New England, and rotated cyclonically to the northwest (not shown). The associated 700-hPa flow configuration at 1800/25 was marked by strong southerly flow approaching 25 m s^{-1} on the southeast side of this trough, with weak and variable flow on the northwest side of this trough (not shown). This flow convergence was occurring in the presence of a 5°C $(100 \text{ km})^{-1}$ temperature gradient, resulting in a band of intense 700-hPa frontogenesis [values approaching 4°C $(100 \text{ km})^{-1}$ $(\text{h})^{-1}$] stretching from northeast Pennsylvania into southern New Hampshire (Fig. 2.4a). Heavy snowfall was occurring near this 700-hPa frontogenesis maximum (Fig 2.4a), while farther to the southeast near the coast the reflectivity was enhanced by a bright band associated with a melting layer. The MM5 forecast the heavy snowfall[1] near the developing 700-hPa low, although the forecast trough axis was ~50–100 km farther south than observed (cf. Figs. 2.4a,b). The corresponding frontogenesis maximum was comparable in magnitude to the analyzed maximum.

By 2100/25, an intense snowband had developed just west of the analyzed 700-hPa trough (Fig. 2.4c), with ~25 m s^{-1} southeast winds to the east of the trough and ~7 m s^{-1} north winds to the west of the trough (Fig. 2.5a). This flow convergence and deformation in the presence of a temperature gradient resulted in 700-hPa frontogenesis values exceeding 7°C $(100 \text{ km})^{-1}$ $(\text{h})^{-1}$ (Fig 2.5a), with the snowband occurring just to the west of the 700-hPa frontogenesis maximum (Fig. 2.4c). The MM5 successfully forecast intense band development, but the band was ~50 km farther southeast than observed (cf. Figs. 2.4c,d). Similar to the analysis, the MM5 forecast trough served as a focus for frontogenesis (cf. Figs. 2.5a,b). However, the axis of maximum frontogenesis was forecast by the MM5 ~50 km farther southeast than analyzed, which is consistent with the position error of the forecast band.

By 0000/26, the analyzed 700-hPa frontogenesis maximum began to weaken as the 700-hPa trough became less defined, and the associated deformation weakened (Fig. 2.4e); however, a band of frontogenesis still extended from eastern New York into Vermont and New Hampshire. The primary snowband remained just west of the analyzed 700-hPa frontogenesis maximum (Fig. 2.4e). Over the next 2.5 h, the frontogenesis continued to weaken and the snowband dissipated, with analyzed and forecast frontogenesis values of 4°C $(100 \text{ km})^{-1}$ $(\text{h})^{-1}$ limited to the New York/Massachusetts border region (Figs. 2.4e,f). However, the MM5 forecast band dissipated at 0000/26, approximately 2.5 h earlier than observed.

c. QPF

The observed 24-h accumulated precipitation (liquid-equivalent) ending 1200/26 exceeded 45 mm in a band stretching from northeast Pennsylvania into eastern New York (Fig. 2.6a). An embedded maximum of 76 mm was located in eastern New York (Fig. 2.6a). The 12-km MM5 forecast accumulated precipitation band (Fig. 2.6b) was ~50 km to the east as compared to the observed location (Fig. 2.6a), which is consistent with the displaced forcing (e.g., Fig. 2.5). A second maximum of precipitation forecast in northern

---

[1] Simulated reflectivities were calculated using empirical relations based on the model cloud and precipitation mixing ratios as in Koch et al. (2005). Due to the uncertainties in obtaining the simulated reflectivity, only qualitative comparisons are made between observed and model reflectivity structures.

Connecticut was not observed (cf. Figs. 2.6a,b). The12-km MM5 forecast precipitation maximum within the band was 46 mm, which is ~40% less than observed. The corresponding 4-km and 1.33-km MM5 precipitation fields exhibited a 53 mm (~30% underprediction) and 59 mm (~22% underprediction) maximum within the band (Figs. 2.6c and d, respectively), with greater spatial variance in precipitation likely from the improved representation of orographic effects (i.e., Fig. 2.1b). Thus, higher horizontal model resolution does result in improved QPF in this case, but it is not the sole answer.

Comparisons of band width using simulated reflectivity fields averaged over the band life cycle showed a 15% reduction in band width when reducing grid spacing from 12 km to 4 km, but no further decrease when using 1.33-km grid spacing (not shown), suggesting the band was explicitly resolved at 4-km grid spacing. Therefore, the 4-km MM5 fields are used in the subsequent investigation of band life cycle.

2.4 Band life cycle

The band life cycle is subjectively divided into three stages – band formation, band maturity, and band dissipation. Timing differences of band dissipation between the model forecast and observations required comparing the 2300/25 model fields with the 0000/26 observed fields. Also, position differences in the maximum band intensity between the model forecast and observations necessitated different model and observed cross section locations.

a. Band Formation

WSR-88D radar observations from the dual-Doppler synthesis at 1800/25 show a large region of enhanced precipitation in central New York (Fig 2.7a). Animations over the subsequent 90 min showed enhanced reflectivity features moving towards the northwest and merging along a northeast-southwest axis, forming the primary band by 1929/25 (Fig. 2.8a). Examples of these enhanced reflectivity features are evident near the New Jersey/Pennsylvania border region (Fig. 2.7a), and in northeast Pennsylvania (Fig. 2.8a), just southeast of the primary band. These band mergers and subsequent band formation occurred in a region of intense midlevel convergent flow associated with the midlevel trough (Fig. 2.4a). These convergent winds are evident in the dual-Doppler derived winds at 3 km MSL, where 25 m s^{-1} southeast winds slow to less than 5 m s^{-1} over a horizontal distance of 100 km (Fig. 2.7a), resulting in convergence of ~2 x 10^{-4} s^{-1}. This convergence is also evident in the wind profiler and aircraft observations across the region (Fig. 2.7a). By 1930/25 (Fig. 2.8a), the winds on the west side of the band turned to light northerly as the associated midlevel trough strengthened, which effectively increased the deformation and maximum convergence to ~2.4 x 10^{-4} s^{-1}.

The 4-km MM5 forecast evolution of band formation is similar to the observations. At 1800/25, an east-northeast–west-southwest oriented band was located in a region of speed convergence at 3 km MSL over eastern New York, while a second band was located farther southeast over western Connecticut (Fig. 2.7b). The first band weakened nearly in place over the next ~45 min, while the second band moved northwest into eastern New York, and became stretched along a northeast–southwest axis, forming the primary band by 1930/25 (Fig. 2.8b). The presence of light winds on the west side of the band at 1930/25 is similar to the dual-Doppler observations (cf. Figs. 2.8a,b).

At 1800/25, maximum frontogenesis values between 7 and 12°C (100 km)$^{-1}$ (h)$^{-1}$ were located over southeast New York, associated with speed convergence in the presence of a 2.3°C (100 km)$^{-1}$ temperature gradient (Fig. 2.7c). Ninety minutes later (Fig. 2.8c), the temperature gradient increased to ~2.7 °C (100 km)$^{-1}$, and the convergence and deformation increased (related to the development of light winds on the west side of the trough). The combined effect was an increase in frontogenesis to values over 12°C (100 km)$^{-1}$ (h)$^{-1}$ (Fig. 2.8c).

At 1800/25, a cross section of analyzed frontogenesis, ascent, and observed reflectivity through the band formation region (Fig. 2.9a) shows that the frontogenesis maximum sloped from the surface (near the position of the warm occlusion) to 5 km MSL. This frontogenesis resulted in a relatively broad region of ascent, maximized at over 40 cm s^{-1} at a height of 5 km MSL (Fig. 2.9a). The resultant heavy snowfall occurred in a ~150 km wide region, with the height of the observed 30 dBZ contour extending to nearly 5 km MSL (Fig. 2.9a). A region of negative EPV existed above the frontogenesis maximum in the 400–500-hPa layer (Fig. 2.9b), with θ_{es} field indicating that much of this negative EPV region was associated with conditional instability (CI). A small portion of the CI region near 400 hPa at x = 300 km also exhibited negative absolute vorticity (calculated using the full wind), indicative of inertial instability (II). However, given the small area of II and faster growth rates of CI (Bennetts and Hoskins 1979; Bennetts and Sharp 1982), CI was likely the dominant instability. Although the CI lies above the maximum frontogenesis, the vertical motion forced by frontogenesis extends well above the location of maximum frontogenesis (e.g., Sawyer 1956; Eliassen 1962; Thorpe and Emanuel 1985; Hakim and Keyser 2001). Thus, the observed heavy snowfall at 1800/25 was likely a result of the release of CI by frontogenetical forcing.

The corresponding 1800/25 4-km MM5 cross section (Figs. 2.9c,d) is similar to the analyzed 1800/25 cross section, with a sloping region of frontogenesis, associated ascent, and precipitation plume evident; however, the model cross section exhibits two distinct reflectivity bands near the surface at x = 120 km and x = 270 km (Fig. 2.9c). These reflectivity bands are associated with two separate ascent maxima, the strongest of which nears 80 cm s^{-1} (Fig. 2.9c). The ascent maxima and associated bands are forced by two sloping frontogenesis maxima (Fig. 2.9c). These frontogenesis maxima correspond to two enhanced thermal gradients over southeast New York at 3 km MSL (Fig. 2.7c). The corresponding MM5 cross section of the stability fields (Fig. 2.9d) indicates three regions of negative EPV in the 500–400-hPa layer. The first region (x = 270 km) is marked by both CI and II, whereas the second (x = 180 km) and third (x = 100 km) regions are marked by II. A large area of conditional neutrality exists between the first and second negative EPV minima in the region of strongest ascent. During the 1600–1800/25 period, elevated CI was diagnosed in this region (not shown). Thus, as shown in the Eta analysis, the modeled heavy snowfall at 1800/25 was likely a result of the release of CI and II by frontogenetical forcing.

By 1930/25 (Fig. 2.10a), the observed reflectivities evolved into a narrow and intense (> 30 dBZ) band. The corresponding MM5 forecast shows that the double frontogenesis/ascent pattern and associated bands at 1800/25 had evolved into a single intense band, associated with a single frontogenesis/ascent maximum (Fig. 2.10b). The 4-km MM5 conditional stability at 1930/25 had generally increased during the past 90 min (cf. Figs. 2.9d and 2.10c); however, an ~30-km wide region of negative EPV existed between 500 and 400 hPa on the equatorward edge of the ascent maximum. This negative EPV region coincides with a region of II.

b. Band maturity

The mature stage of the band life cycle occurred at 2100/25, when both the observed and modeled bands were near their peak intensity. At this time, the 3-km MSL dual-Doppler winds exhibited a sharp cyclonic wind shift near the observed band, with strong southeast winds (17 m s^{-1}) on the east side of the band, and the emergence of 10 m s^{-1} north winds on the west side of the band (Fig. 2.11a). The position of this cyclonic wind shift, as well as the band, had moved eastward ~40 km during the past 90 min (cf. Figs. 2.8a and 2.11a).

The corresponding 4-km MM5 forecast also shows the establishment of a robust cyclonic wind shift near the simulated band (Fig. 2.11b). The magnitude of the temperature gradient had nearly tripled during the past 1.5 h, reaching a magnitude of ~8.3°C (100 km)$^{-1}$ within the region of maximum speed convergence just east of the trough axis (Fig. 2.11c). As will be shown in the next chapter, the temperature gradient was largely created by horizontal latent heating gradients; however, the development of a local temperature minimum along a southwest–northeast axis nearly coincident with the band (Fig. 2.11c) also contributed to the temperature gradient. Parcel trajectories and point temperature tendency calculations suggest that this local cooling was the result of the vertical advection of cooler air below the frontal inversion (in the 2–3 km MSL layer) by the band updraft (not shown). The coincidence of this large temperature gradient with the zone of strong speed convergence resulted in frontogenesis values exceeding 19°C (100 km)$^{-1}$ (h)$^{-1}$ (Fig. 2.11c).

A cross section of analyzed frontogenesis and ascent at 2100/25 (Fig. 2.12a) shows an intense frontogenesis maximum centered at 2.5 km MSL, with ascent nearing 30 cm s^{-1} above this level (Fig. 2.12a). The corresponding 4-km MM5 cross section at 2100/25 (Fig. 2.12c) is similar to the analysis cross section, with an intense frontogenesis maximum near 700 hPa and a narrow sloping updraft approaching 70 cm s^{-1} (Fig. 2.12c). Recall from section 1.1b that theory would predict the ascent maximum 50–200 km to the warm side of the frontogenesis maximum. In the present case, both the observed and forecast ascent maximum is found nearly coincident with the frontogenesis maximum (Figs. 2.12b,d). This finding will be further discussed in section 2.6.

The 2100/25 cross section (Fig. 2.12a) also shows that the observed reflectivity core sloped downward to the west, such that the band core was ~10 km farther west at the surface than at 3 km MSL (Fig. 2.12a). Similar to these radar observations, the MM5 forecast band also exhibited a tilt, such that the band core was ~25 km farther west at the surface than at 3 km MSL (Fig. 2.12c). Explicit calculation of hydrometeor trajectories from the model forecast during the 1900–2100/25 period show that this displacement was due to horizontal advection of snow (Fig. 2.12c), with the band updraft slowing the hydrometeors' fall and prolonging the time the hydrometeors were subject to horizontal advection in the 600–500-hPa layer. Given the observed easterly component of the 3 km MSL winds in the band region (e.g., Fig. 2.11a), hydrometeor advection is the most probable explanation for the observed band tilt. Model hydrometeor (snow) mixing ratios increased towards the surface, ranging from 0.3 g kg^{-1} at 450 hPa to a near surface maximum of ~1.8 g kg^{-1} (not shown), qualitatively similar to the vertical structure of the observed radar reflectivity pattern (Fig. 2.12a), and the schematic shown in Fig. 1.3.

The analyzed stability at 2100/25 indicates a large region of negative EPV on the warm side of the frontogenesis maximum in the 500–350-hPa layer (Fig. 2.12b). The elevated CI in the far southeast location (x = 300 km) transitions to a region of combined CSI and II in the central portion of the cross section (x = 200 km), and weak moist symmetric stability in the northwest part of the cross section (x = 100 km). This distribution of stability is consistent with idealized schematics of stability regimes within a banded frontal zone (e.g., Schultz and Schumacher 1999; Moore et al. 2005). In contrast to the presence of CI and CSI at 2100/25 in the analysis, the MM5 forecast stability fields indicated conditional *stability* above the frontogenesis maximum at this time (cf. Figs. 2.12b,d). Although the juxtaposition of dry air over the saturated lower levels supported CI in the 600–700-hPa layer southeast of the banded region (Fig. 2.12d), the weak ascent (and even weak descent) in this region precluded the instability from being released in the MM5 forecast. Despite the conditional stability in the banded region at this time, a relatively small area of negative EPV was found on the equatorward periphery of the sloping ascent maximum associated with II (Fig. 2.12d).

The presence of II in banded frontal zones has been shown in previous idealized and observational studies (e.g., Holt and Thorpe 1991; Persson and Warner 1995; Thorpe and Clough 1991; Jurewicz and Evans 2004; Schultz and Knox 2007). Holt and Thorpe (1991) proposed that upright convection can create II within frontal regions via the vertical advection of low momentum air. The ensuing slantwise flow response was termed ‘delta-M adjustment’ (see also Morcrette and Browning 2006). In the present case, CI (representing the potential for upright convection) was present during band formation (e.g., Figs. 2.9b,c); however, during band maturity CI is absent in the MM5 forecast while II is present (Fig. 2.12d). Examination of the model fields show that the forecast II at 450 hPa was within a 30–40 km wide geopotential height ridge (~3 m amplitude), which was directly above a maximum in the 700–500-hPa layer-averaged condensational heating (associated with the snowband) (Fig. 2.13). The positive height perturbations and associated anticyclonic flow are consistent with a diabatically generated ridge associated with diabatic heating by the band itself. Similar correspondence between condensational heating, height perturbations, and II were found at the time of band formation and dissipation (not shown). Given the presence of the II in the absence of upright convection, it seems likely that the diagnosed presence of II in the model forecast during band life cycle in this case is a diabatic signature of the band itself.

c. Band dissipation

At 0000/26, the weakening snowband was found near the New York/Massachusetts border, with the cyclone’s dry slot evident in eastern Connecticut and Massachusetts (Fig. 2.14a, see also Fig. 2.2e). Although the cyclonic wind shift had moved to the east of the dual-Doppler coverage area, wind observations from the Schenectady, New York (SCH) and Orange, Massachusetts (ORE) profilers (Fig. 2.1a) showed that the 3-km MSL wind shift was aligned from southern New Hampshire through western Massachusetts (Fig. 2.14a). Southeast winds on the east side of this trough (15 m s^{-1} at ORE) were considerably weaker than during band formation or maturity (cf. Figs. 2.11a and 2.14a), resulting in reduced convergence, deformation, and associated frontogenesis relative to earlier times.

The MM5 forecast valid at 2300/25 shows that the cyclonic wind shift had moved east ~50 km during the past 2 h (cf. Figs. 2.11b and 2.14b). Southeast winds on the east side of this trough were ~5 m s^{-1} less than observed (cf. Figs. 2.14a,b), and ~5 m s^{-1} less than during band maturity (cf. Figs. 2.11b and 2.14b). Localized maxima of convergence and deformation were found in western Massachusetts and southern New York, resulting in two frontogenesis maxima (Fig. 2.14c); however, the frontogenesis maxima were considerably weaker than at the time of band maturity (cf. Figs. 2.11c and 2.14c)

Cross sections through the observed and forecast band show that the frontogenesis and ascent had weakened from the time of band maturity (cf. Figs. 2.15a and 2.12a, and Figs. 2.15c and 2.12c). The analyzed stability had increased from the time of band maturity, with only a small region of CI found above the band in the 600–500-hPa layer (cf. Figs. 2.12b and 2.15b). CI was absent in the model stability fields in the banded region (Fig. 2.15d); however, once again a small area of negative EPV was found on the equatorward periphery of the sloping ascent maximum (Fig. 2.15d), associated with II.

d. Model time series

A time series of frontogenesis, ascent, and conditional stability during the life cycle of the simulated band was constructed to better understand its evolution. Cross sections from the 4-km MM5 forecast along section A-B (see Fig. 2.7b) were examined to determine the magnitude of the midlevel frontogenesis maximum at the base of the band updraft, the difference of θ_{es} between 600 and 400 hPa on the equatorward flank of the band updraft (a measure of the conditional stability), and the magnitude of the ascent maximum. These parameters were recorded every 15 min during the 1800/25 to 0000/26 time period.

During the time of band formation, the frontogenetical forcing was increasing, while the 600–400-hPa layer conditional stability was also increasing (Fig. 2.16). In fact, the smallest θ_{es} difference between 600 and 400 hPa was during the first hour of the time series, when there were shallow, embedded layers of CI (e.g., Fig. 2.9d). Ascent exceeding 1 m s^{-1} was present from 1830 to 1915/25. This ascent dramatically weakened to 68 cm s^{-1} over the next 45 min as the band formed. Thus, the evolution of ascent, frontogenesis, and conditional stability is consistent with the release of elevated CI in the presence of increasing frontogenetical forcing. The band formed as this instability was released in the sharp convergence zone associated with the developing midlevel trough.

Despite the increasing conditional stability during the time of band maturity, the ascent remained nearly constant near 60 cm s^{-1}. The effect of increasing conditional stability was mitigated by increasing frontogenetical forcing, which reached a peak of 35°C $(100\ \text{km})^{-1}\ (\text{h})^{-1}$ at 2100/25. After 2100/25, the combined effect of weakening frontogenetical forcing and large conditional stability resulted in band dissipation, with ascent weakening to less than 40 cm s^{-1} by 0000/26. Thus, changes in both the forcing and stability contributed to band dissipation.

2.5 Moisture availability

In addition to frontogenetical forcing and weak moist symmetric stability, there must be sufficient moisture for band formation to occur. The 12-km MM5 forecast fields were used to determine what role changes in moisture availability in the banded region played in band evolution. However, first the MM5 forecast moisture evolution is validated.

Comparison of observed and forecast IPW values during the 1500/25 to 0300/26 period show that the MM5 underpredicted IPW on the order of 0.5–1.0 g kg^{-1} (~5%) at all stations except Westford, Massachusetts (Fig. 2.17). The 0000/26 Albany, New York (ALB) sounding, which was launched in the immediate vicinity of the band, also exhibited a 0.8 g kg^{-1} (~6%) underprediction of IPW (Fig. 2.17). This small moisture error in the model forecast was likely a contributing factor to the underprediction in precipitation (i.e., Fig. 2.6). Although there was slightly less moisture modeled in the banded region than observed, the temporal evolution of the moisture fields was well forecast.

To investigate changes in moisture availability, the 12-km MM5 forecast was used to calculate trajectories of parcels which were located in the core of the modeled band updraft at the time of band formation (1930/25), band maturity (2100/25), and the start of band dissipation (2200/25). The core of the band updraft was located at 500 hPa at 1930 UTC and lowered to 600 hPa at 2100/25 and 2200/25. A total set of 21 trajectories were calculated in 7 clusters separated ~50 km apart along the band axis, with each cluster composed of 3 points aligned across the band axis (separated 12-km apart). Three representative trajectories were chosen at each time to represent parcels on the western side of the band updraft (parcel W), on the eastern side of the band updraft (parcel E), and in the center of the band updraft (parcel C). The location, pressure, temperature, and mixing ratios of all trajectory parcels were recorded every 15 min from the model forecast during the 15-h period from 1200/25 to 0300/26. Mixing ratios are noted at the initial time, the final time, and at the time when the parcels reach 600 hPa in the band updraft. Since the saturation mixing ratio is temperature and pressure dependent, a common pressure level (600 hPa) was chosen to allow comparisons of moisture within the band updraft during band life cycle.

This analysis shows that parcels within the band updraft at 1930/25 originated in the marine boundary layer over the Atlantic Ocean at 1200/25 (Fig. 2.18a), with initial mixing ratios ranging from 6.7 to 7.7 g kg^{-1} (Fig. 2.18b). These parcels moved west-northwest and turned cyclonically as they first rose near the surface occluded front, and then rose within the band updraft (Figs. 2.18a,b). Although a large portion of the original moisture content had precipitated out by the time the parcels arrived at 600 hPa, the parcels retained mixing ratio values between 2.4 and 2.9 g kg^{-1}. The easternmost parcel continued moving to the north-northwest, while parcels farther west turned cyclonically, dramatically illustrating the deformation of the flow. The cyclonically turning trajectories may be considered representative of the trowal airstream, or alternatively the cyclonically turning portion of the warm conveyor belt.

Parcel trajectories at the start of band dissipation (2200/25) show that the band updraft was composed of two separate airstreams – one originating at low-levels over the Atlantic Ocean represented by parcel E, and a second originating well to the south of the banding region, represented by parcels C and W (Figs. 2.18c,d). As at the time of band formation, parcel E exhibited ascent near the occluded front and within the band updraft; however, the parcel failed to reach 500 hPa in the band updraft (Fig. 2.18d), indicative of the weaker ascent. Parcels C and W ascended near the surface cyclone, and then experienced more modest ascent in the band updraft after 2100/25, also failing to reach 500 hPa (Figs. 2.18c,d). Parcel E turned anticyclonically to the north-northeast, while parcels C and W turned cyclonically, illustrating deformation of the flow even at the time of band dissipation. Parcel mixing ratios at 600 hPa within the band updraft at 2200/25 ranged from 2.0 to 2.4 g kg^{-1} (Fig. 2.18d), which was ~0.4 g kg^{-1} (0.2 g kg^{-1}) less than at the time of band formation (maturity).

The precipitation rate within the modeled band decreased ~30% between 2100/25 and 2200/25 (not shown). To determine what extent changes in moisture and ascent can explain this decrease, parameters from the full set of 21 trajectories were averaged over a 2 h window centered on 2100/25 and 2200/25. A 0.14 g kg^{-1} decrease in water vapor at 600 hPa was recorded between the time of band maturity and band dissipation (Table 1), similar to previously noted changes in parcel C (Fig. 2.18). Trajectories within the modeled dry slot (e.g., Figs. 2.2d,f) remained ~50 km to the east of the band updraft, or arrived after band dissipation (not shown). Thus, the dry airstream was not responsible for the decrease in water vapor. Rather, this decrease was due to changes in the thermal profile, as the mean 2100/25 trajectory set conserved a θ_e of 307.2 K during moist ascent during band dissipation, as compared to 308.3 K during band maturity (Table 1). Using the mean band maturity θ_e profile, and assuming that all moisture condensed and precipitated, the mean ascent profile during band maturity supported a precipitation rate of 9.8 mm h^{-1}. Using the same ascent profile, but with the cooler θ_e during band dissipation supported a precipitation rate of 9.2 mm h^{-1}, which is 6% less than at the time of band maturity.

The mean ascent averaged amongst the 21 trajectories decreased markedly between 2100/25 and 2200/25 (Table 1). Using the band maturity moisture profile, assuming all moisture was condensed and precipitated, and substituting the band dissipation ascent profile resulted in a calculated precipitation rate of 7.5 mm h^{-1}, which is 23.5% less than at the time of band maturity. Thus, changes in ascent (indicative of changes in frontogenesis and stability) dominated changes in moisture in explaining band dissipation in this case.

2.6 Summary and discussion

Dual-Doppler, wind profiler, and aircraft observations in concert with MM5 simulations down to 1.33-km grid spacing were used to investigate the life cycle of an intense mesoscale snowband occurring 25–26 December 2002. Results from this study show that both the observed and modeled band evolution were related to changes in forcing, stability, and moisture, validating the importance of these parameters in governing band life cycle.

The observations and MM5 forecast show band formation was coincident with the sharpening of a midlevel trough and associated increase in deformation, convergence, and frontogenesis. Although a midlevel trough is evident in previously documented cases (Sanders 1986, his Fig. 6; Nicosia and Grumm 1999, their Figs. 4, 9, and 14; Martin 1998a, his Fig. 3), the dual-Doppler observations in the present case help illustrate the pronounced sharpness of the trough and associated wind shift at the time of band formation. Band dissipation occurred as the midlevel trough became less defined and the frontogenetical flow weakened. The weakening frontogenetical forcing in the presence of conditional stability led to a weakening frontal circulation. Chapter 3 will investigate the processes responsible for the formation and evolution of the midlevel trough and associated frontogenesis maximum in this case, since it is a critical feature of the band life cycle.

The current case exhibited CI at least 1.5 h before band formation (e.g., Fig. 2.9b). Band formation occurred as this CI was released by increasing frontogenetical forcing, and the conditional stability increased. This result may seem in contrast to the case studies of Nicosia and Grumm (1999), in which band formation occurred as the EPV decreased sharply. However, an important difference between the present work and Nicosia and Grumm (1999) is that Nicosia and Grumm (1999) calculated EPV using the geostrophic wind, which would be more susceptible to the absolute vorticity becoming negative (II). Even in the present case where the full wind is used in calculating EPV, small regions of negative EPV were diagnosed throughout the band life cycle as a symptom of the diabatically-generated flow from the band itself. However, just considering the θ_{es} fields in Figs 5, 10, and 15 of Nicosia and Grumm (1999), the smallest conditional stability was observed before band formation, and the conditional stability increased during the band life cycles in each case, as observed and simulated in the present case. A similar stability evolution has been noted by Greenstein (2006, 88–89) and Evans and Jurewicz (2009). Additional cases are necessary to determine whether single-band formation may be associated with the transition from a state of elevated CI, to weak conditional and/or moist symmetric stability, which will be explored in chapter 4.

Cross sections through the observed and simulated band revealed that the band core sloped downward to the west at times, which was shown to be a signature of hydrometeor advection. Cross sections also revealed that the ascent maximum was found nearly coincident with the frontogenesis maximum, counter to previous theoretical work which predicts the ascent maximum 50–200 km on the warm side of the frontal forcing. However, Hakim and Keyser (2001) showed that the value of this displacement is proportional to the static stability and baroclinicity, and inversely proportional to the inertial stability. In the present case, although II was diagnosed in the 400–500-hPa layer, large inertial stability associated with the sharp cyclonic wind shift was diagnosed at the level of maximum frontogenetical forcing (3 km MSL). In this environment the ascent maximum is expected to be closer to the frontogenetical forcing. A component of the displacement discrepancy in this case may also arise from theoretical studies using frontogenetical forcing maximized near the surface (Thorpe and Emanuel 1985; Xu 1992), without a slope (Emanuel 1985), or at a point (Hakim and Keyser 2001), whereas this case exhibits a deep sloping layer of frontogenesis.

Trajectories from the model simulation show that the primary source of moisture during band formation was from the Atlantic Ocean boundary layer. As the band evolved, this moisture-laden airstream was relegated to just the eastern portion of the band, while the remaining length of the band was fed by slightly colder (drier) air originating in the midlevels to south of the banding region. This change in moisture was calculated to result in a 6% reduction in precipitation rate. A larger reduction in precipitation rate (23%) was calculated due to changing ascent. Thus the effect of changing ascent (indicative of changes in frontogenesis and stability) dominated over changing moisture in explaining band dissipation.

Maximum precipitation was underforecast within the banded region by ~30% at 4 km grid spacing, and the axis of heaviest precipitation was displaced ~50 km to the southeast of the observed location. Comparisons between high-resolution observations and the model forecasts show that the band position error was tied to an error in the location of the midlevel trough and subsequent location of mesoscale forcing. The early weakening of this trough and associated frontogenesis in the presence of stronger conditional stability than analyzed led to premature band dissipation in the MM5 forecast. The greater stability and shorter band duration in the MM5 forecast likely accounted for a majority of the precipitation underprediction, although a small underprediction of integrated precipitable water vapor in the banded region also likely contributed. Higher horizontal model resolution was shown to contribute toward improved QPF; however, it appears more dramatic improvement may be gained by better simulating the frontogenesis, stability, and moisture evolution in this case.

This study illustrates that mesoscale models are capable of generating realistic snowbands; however, the intrinsic uncertainties associated with forecasting the evolution of forcing, stability, and moisture suggest improved forecasts of mesoscale bands and the resulting QPF will likely require ensemble approaches. This future work will be discussed in chapter 5.

Tables

Table 2.1 Comparison of mean trajectory parameters for the time of band maturity (2100 UTC) and the start of band dissipation (2200 UTC).

	Ascent (hPa h^{-1})	600 hPa Mixing Ratio (g kg^{-1})	Equivalent Potential Temperature (K)
2100 UTC	73.5	2.25	308.3
2200 UTC	62.5	2.11	307.2

Figures

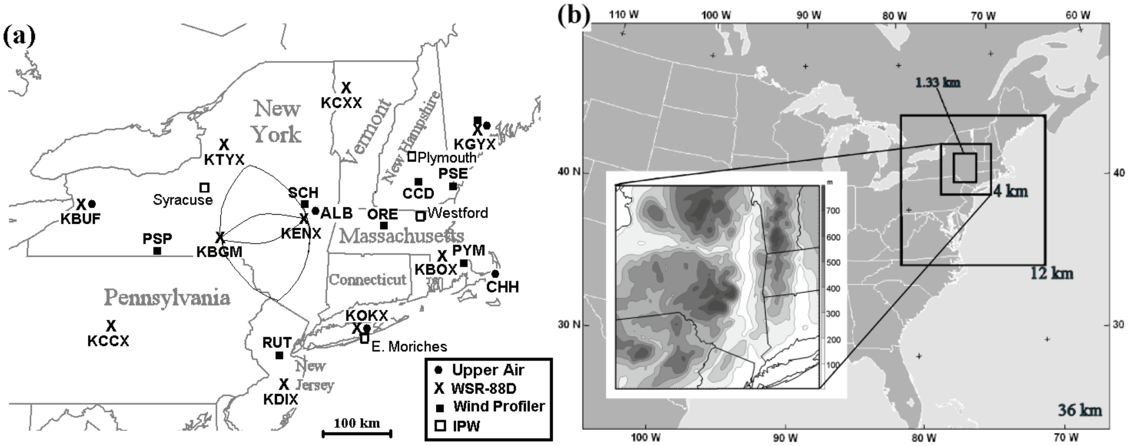

Figure 2.1 (a) Station identifiers and locations of upper-air sounding (dot), WSR-88D ("x"), wind profiler (filled square), and integrated precipitable water vapor (open square) observation sites used in the study. Dual-Doppler coverage area outlined. (b) 36-km model simulation domain, with inner boxes outlining locations of the 12-, 4-, and 1.33-km nested domains, respectively. Insert shows the terrain (m) of the 4-km domain.

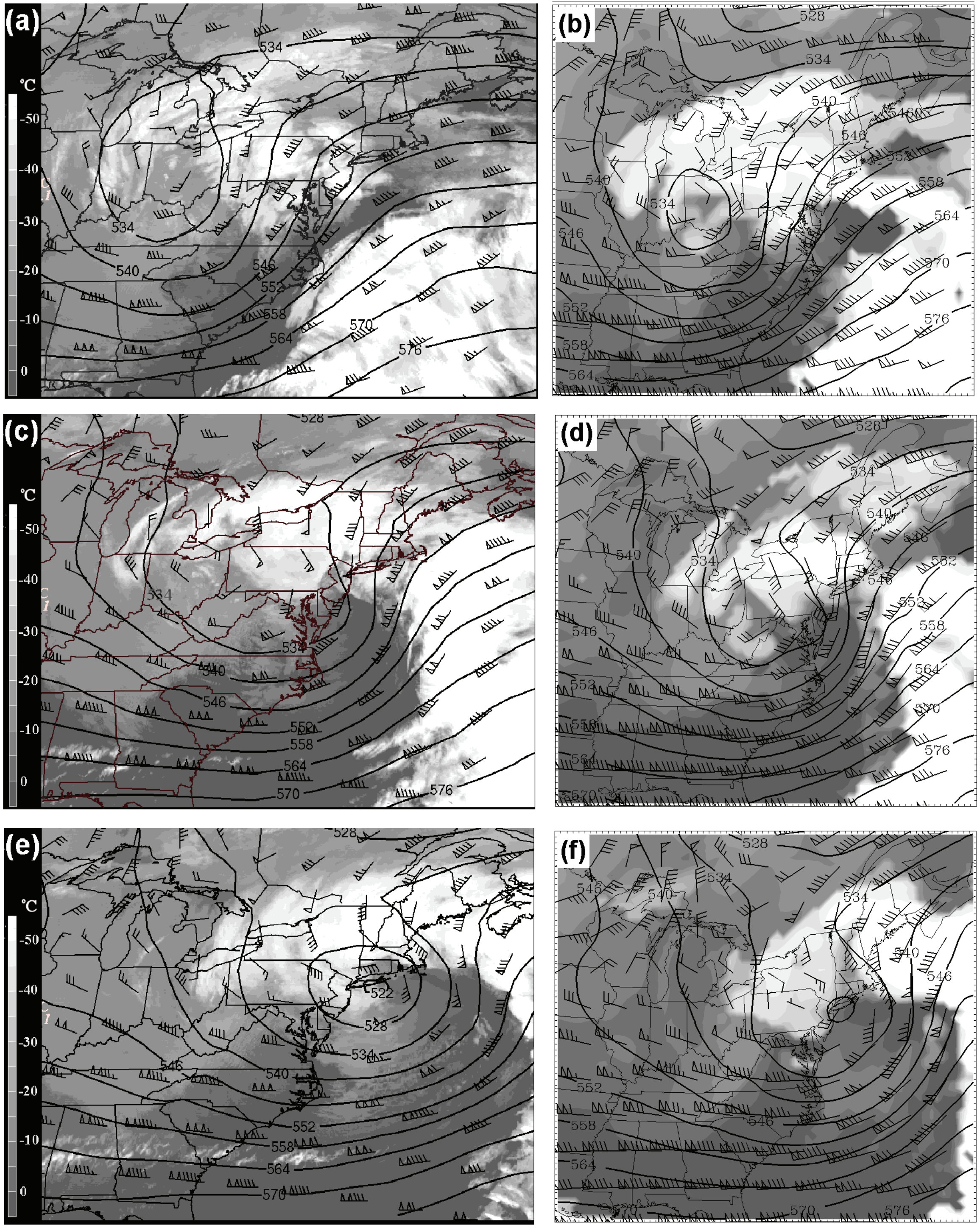

Figure 2.2 Eta analysis of 500-hPa geopotential height (solid, contoured every 60 m), 300-hPa wind (full barb = 5 m s^{-1}, pennant = 25 m s^{-1}), and the infrared brightness temperature (°C, shaded) for (a) 1200 UTC, (c) 1800 UTC 25 Dec 2002, and (e) 0000 UTC 26 Dec 2002. (b) As in (a), except 12-h MM5 forecast cloud top temperature (shaded) valid at 1200 UTC 25 Dec 2002. (d) As in (b), except 18-h MM5 forecast valid at 1800 UTC 25 Dec 2002. (f) As in (b), except 24-h MM5 forecast valid at 0000 UTC 26 Dec 2002.

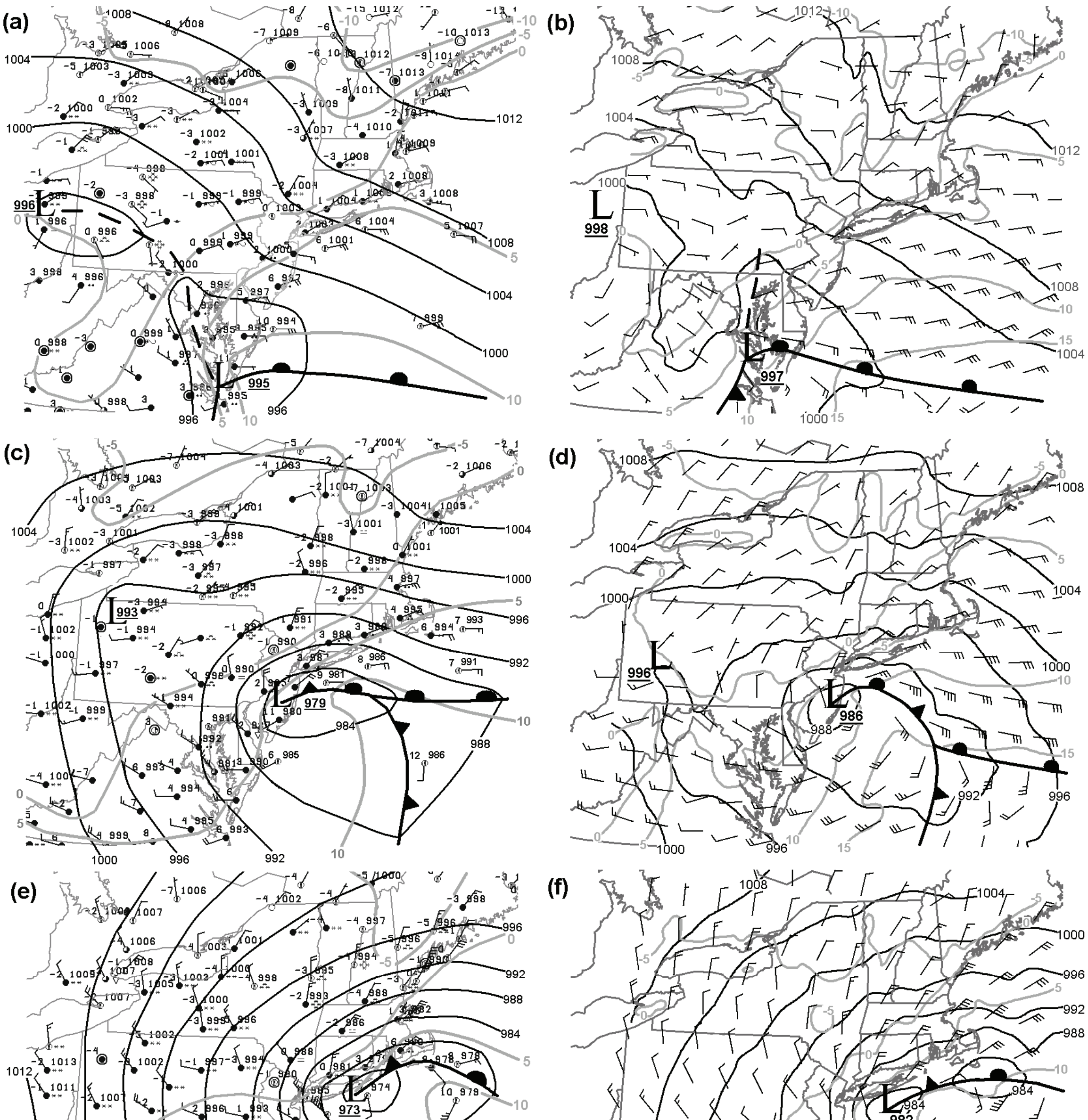

Figure 2.3 Manual surface analysis with conventional surface station symbols, isobars (solid, contoured every 4 hPa), isotherms (gray, contoured every 5°C), and surface fronts valid at (a) 1200 UTC, (c) 1800 UTC 25 Dec 2002, and (e) 0000 UTC 26 Dec 2002. (b) As in (a), except MM5 12-h forecast valid at 1200 UTC 25 Dec 2002. (d) As in (a), except 18-h MM5 forecast valid at 1800 UTC 25 Dec 2002. (f) As in (a), except 24-h MM5 forecast valid at 0000 UTC 26 Dec 2002.

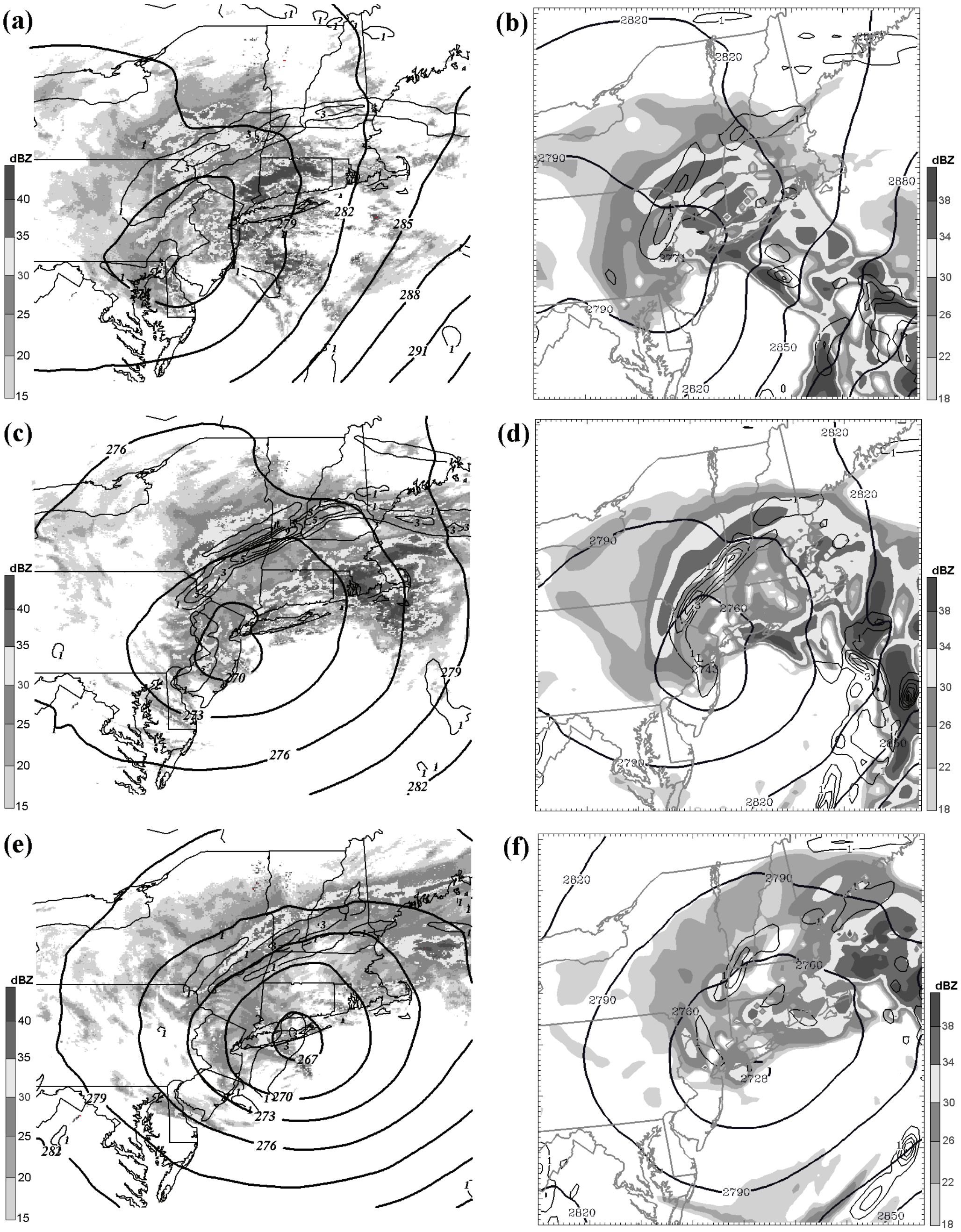

Figure 2.4 WSR-88D radar mosaic (reflectivity shaded according to scale starting at 15 dBZ), with the Eta analysis 700-hPa geopotential height (thick solid, contoured every 30 m), and 700-hPa Petterssen frontogenesis [thin solid, positive values contoured every 2°C (100 km)$^{-1}$ (h)$^{-1}$ starting at 1°C (100 km)$^{-1}$ (h)$^{-1}$] overlaid, valid at (a) 1800 UTC, (c) 2100 UTC 25 Dec 2002, and (e) 0000 UTC 26 Dec 2002. (b) 12-km MM5 18-h forecast surface simulated reflectivity (shaded according to scale starting at 18 dBZ), 700-hPa geopotential height (thick gray, contoured every 30 m), and 700-hPa Petterssen frontogenesis [thin solid, positive values contoured every 2ºC (100 km)$^{-1}$ (h)$^{-1}$ starting at 1ºC (100 km)$^{-1}$ (h)$^{-1}$] valid at 1800 UTC 25 Dec 2002. (d) As in (b), except 12-km MM5 21-h forecast, valid at 2100 UTC 25 Dec 2002. (f) As in (b), except 12-km MM5 24-h forecast, valid at 0000 UTC 26 Dec 2002.

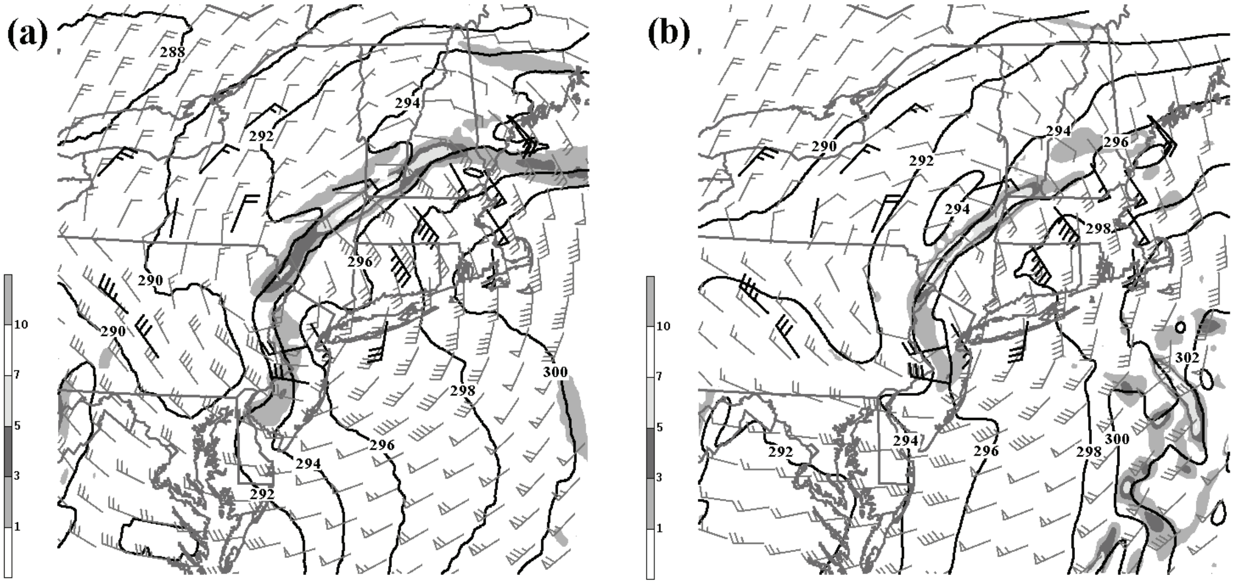

Figure 2.5 (a) 2100 UTC 25 Dec 2002 Eta analysis of 700-hPa Petterssen frontogenesis [shaded according to scale starting at 1°C (100 km)$^{-1}$ h^{-1}], 700-hPa potential temperature (solid, contoured every 2 K), and winds (gray barbs; full barb = 5 m s^{-1}, pennant = 25 m s^{-1}). In situ and remote sensing wind observations displayed as black barbs. (b) As in (a), except 12-km MM5 21-h forecast valid at 2100 UTC 25 Dec 2002.

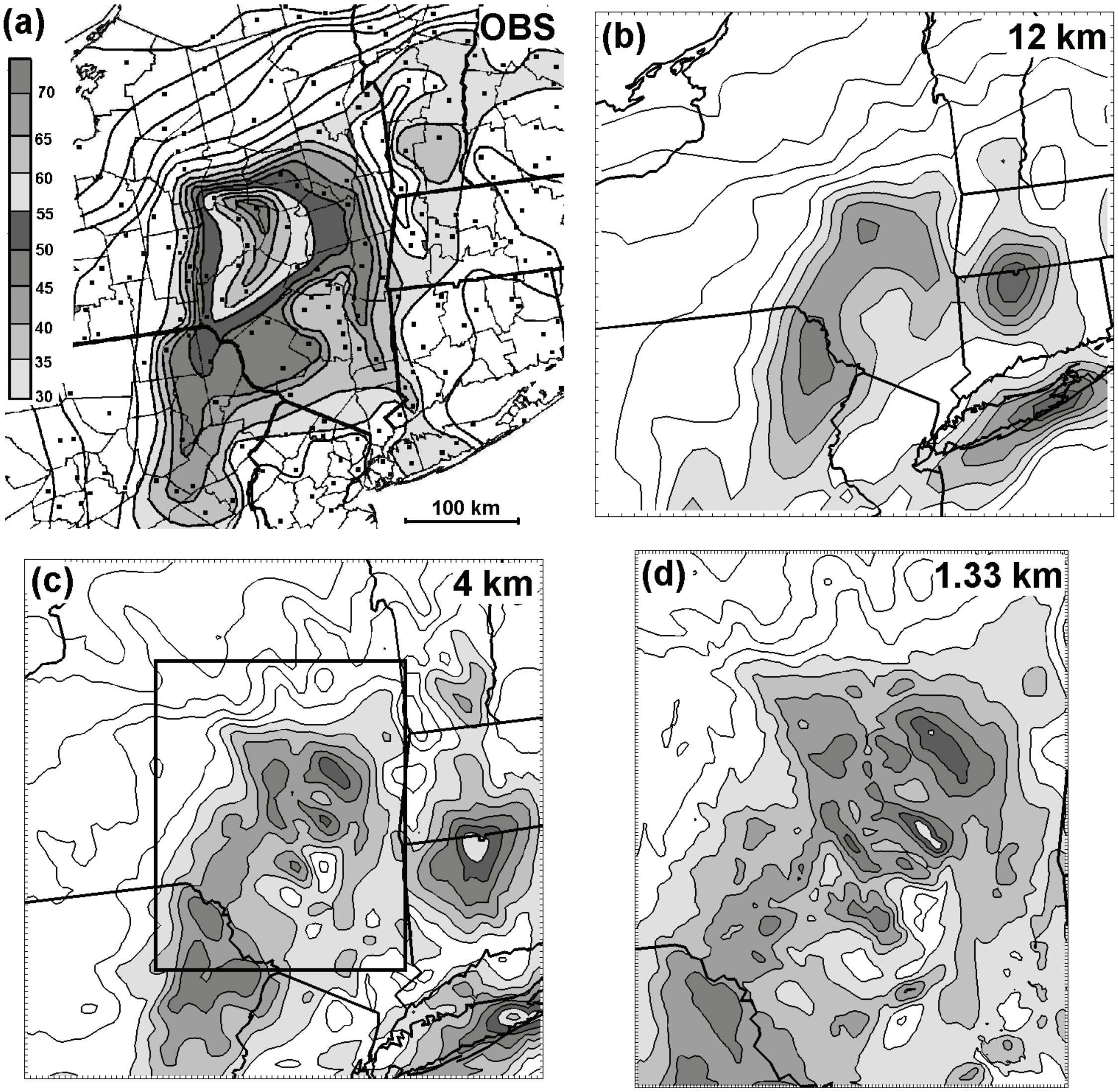

Figure 2.6 (a) Observed liquid equivalent precipitation during the 24-h period ending 1200 UTC 26 Dec 2002 (contoured every 5 mm, shaded according to scale starting at 30 mm). Station observation locations used in the analysis are marked by black dots. Corresponding 12–36 h forecast accumulated precipitation shown for the (b) 12-km, (c) 4-km, and (d) 1.33-km MM5. Domain of (d) outlined by box in (c).

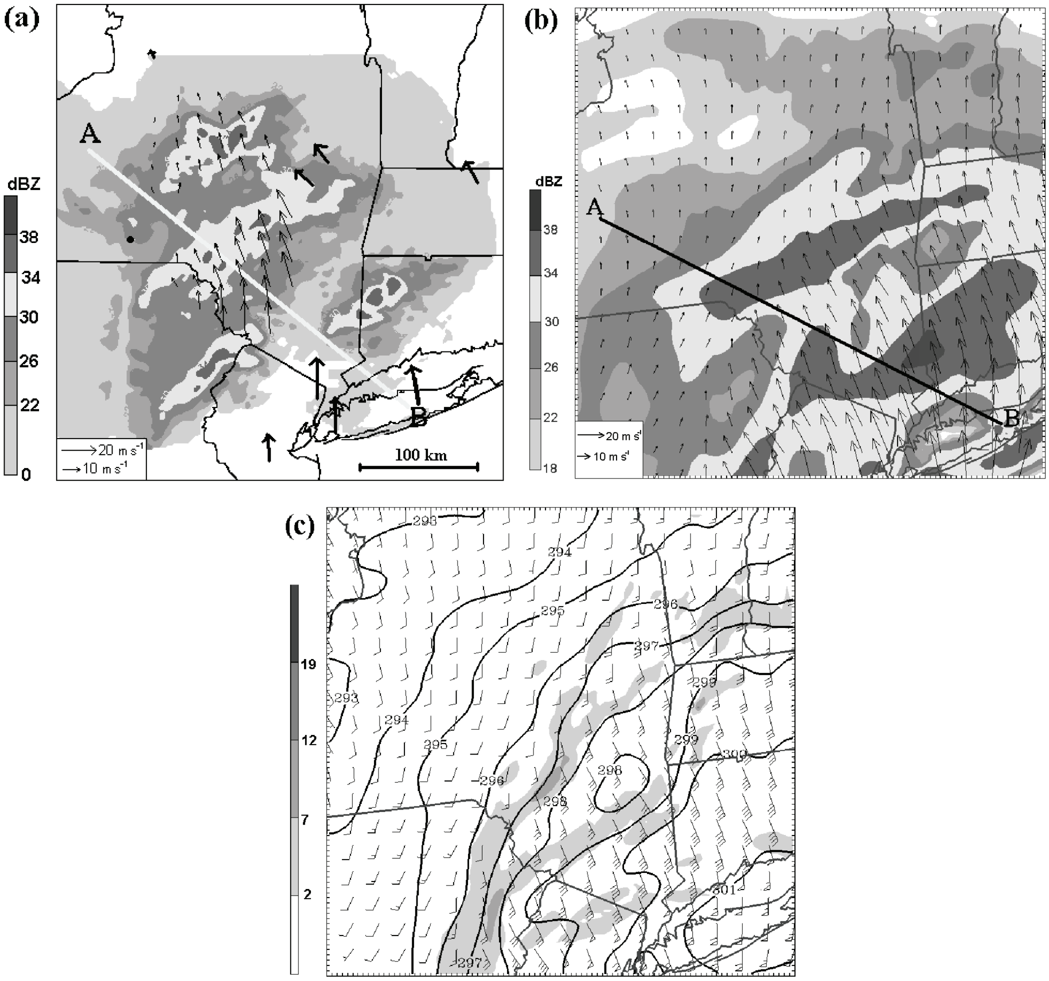

Figure 2.7 (a) Dual-Doppler radar reflectivity (1-km MSL altitude; shaded according to scale) and 3-km MSL winds (arrows) valid at 1802 UTC 25 Dec 2002. In situ and remote sensing wind observations displayed as thick black arrows. (b) 4-km MM5 18-h forecast simulated reflectivity (1-km MSL altitude; shaded according to scale) and 3-km MSL wind (arrows). (c) 4-km MM5 18-h forecast Petterssen frontogenesis [shaded according to scale starting at 2ºC (100 km)$^{-1}$ (h)$^{-1}$], potential temperature (solid, contoured every 1 K), and wind (full barb = 5 m s^{-1}, pennant = 25 m s^{-1}) at 3-km MSL.

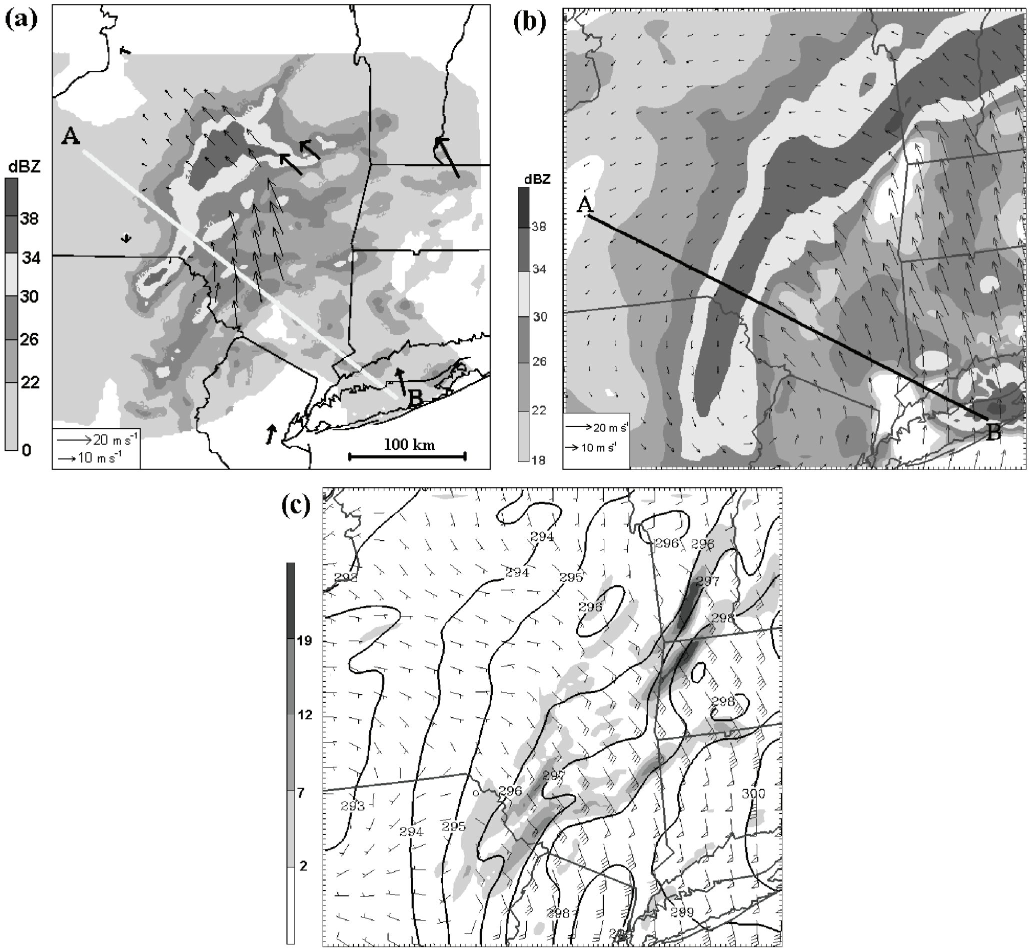

Figure 2.8 (a) As in Fig. 2.7a, except valid at 1929 UTC 25 Dec 2002. (b,c) As in Figs. 2.7b,c, except 19.5-h forecast valid at 1930 UTC 25 Dec 2002.

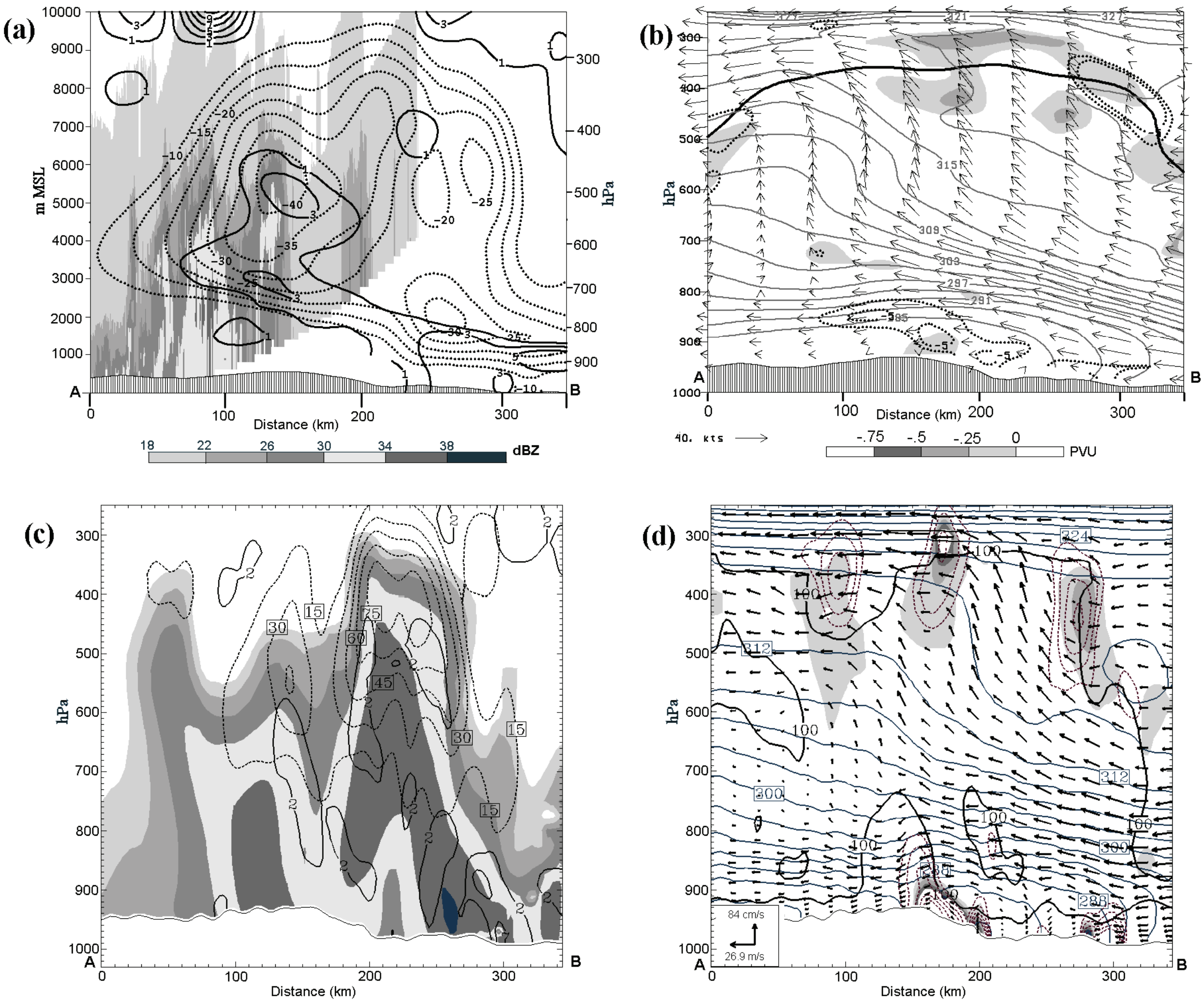

Figure 2.9 (a) KBGM WSR-88D radar reflectivity cross section (orientation shown in Fig. 2.7a) valid at 1802 UTC 25 Dec 2002 with the 1800 UTC Eta analysis Petterssen frontogenesis [solid, positive values contoured every 2ºC (100 km)$^{-1}$ (h)$^{-1}$, starting at 1ºC (100 km)$^{-1}$ (h)$^{-1}$], and ascent (dotted, contoured every 5 cm s^{-1} starting at 10 cm s^{-1}). (b) Cross section as in (a), with saturation equivalent potential vorticity (shaded where negative according to scale), saturation equivalent potential temperature (gray solid, contoured every 3 K), velocity in the plane of the cross section (arrows), absolute vorticity (dotted, contoured where negative every 5 x 10^{-5} s^{-1}), and the 100% contour of relative humidity w.r.t. ice (thick solid). (c) 4-km MM5 18-h forecast cross section (orientation shown in Fig. 2.7b) showing simulated reflectivity [shaded according to scale, as in (a)], Petterssen frontogenesis [black solid, positive values contoured every 4ºC (100 km)$^{-1}$ (h)$^{-1}$ starting at 2ºC (100 km)$^{-1}$ (h)$^{-1}$], and ascent (dotted, contoured every 15 cm s^{-1} starting at 15 cm s^{-1}). (d) As in (b), except for the 4-km MM5 18-h forecast.

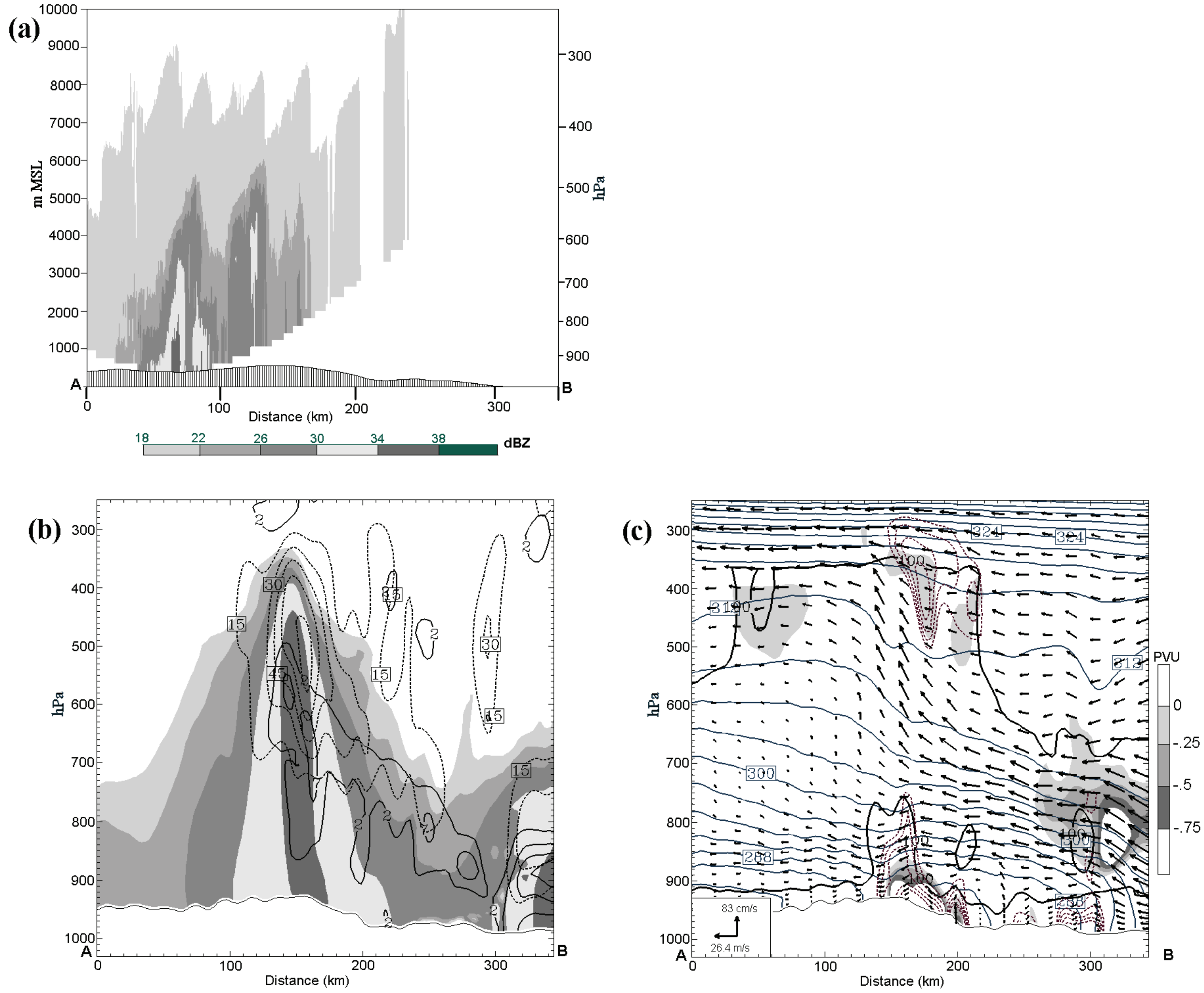

Figure 2.10 (a) KBGM WSR-88D radar reflectivity cross section valid at 1929 UTC 25 Dec 2002. Cross-section orientation shown in Fig. 2.8a. (b,c) As in Figs. 2.9c,d, except for the 4-km MM5 19.5-h forecast valid at 1930 UTC 25 Dec 2002.

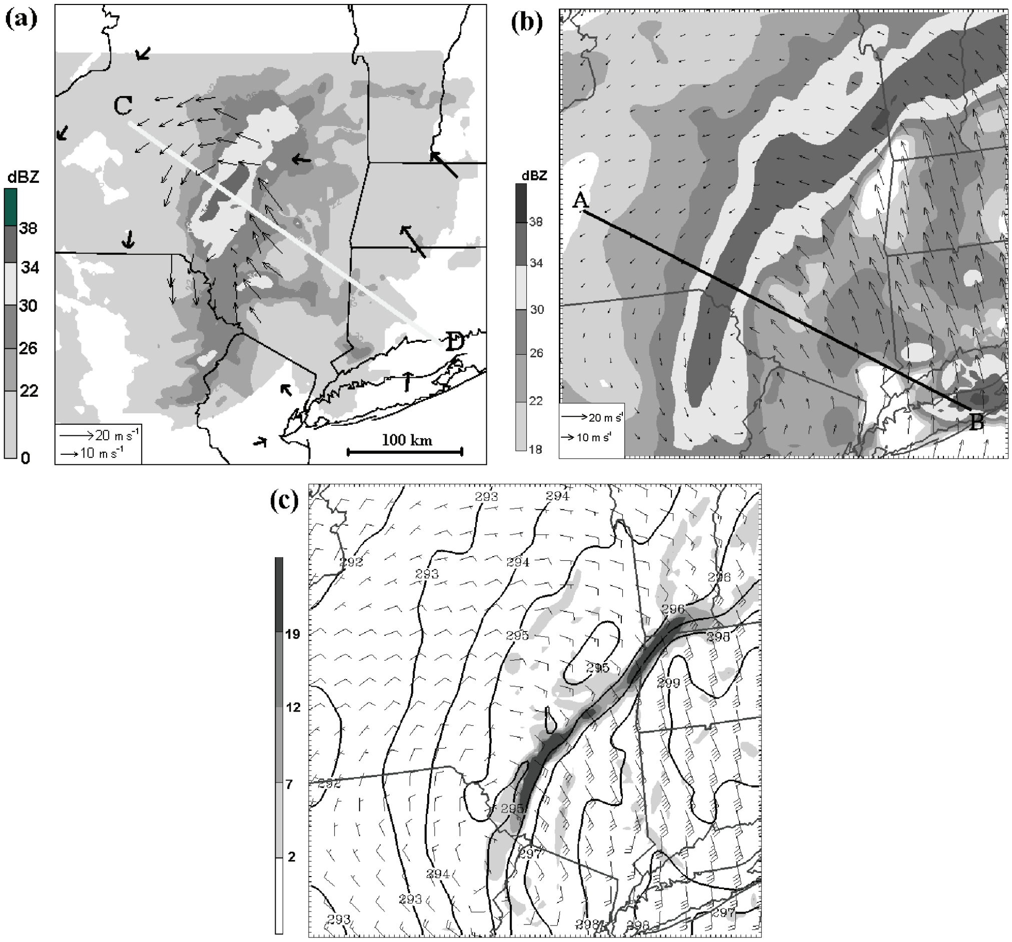

Figure 2.11 (a) As in Fig. 2.7a, except valid at 2101 UTC 25 Dec 2002. (b,c) As in Figs. 2.7b,c, except 4-km MM5 21-h forecast valid at 2100 UTC 25 Dec 2002.

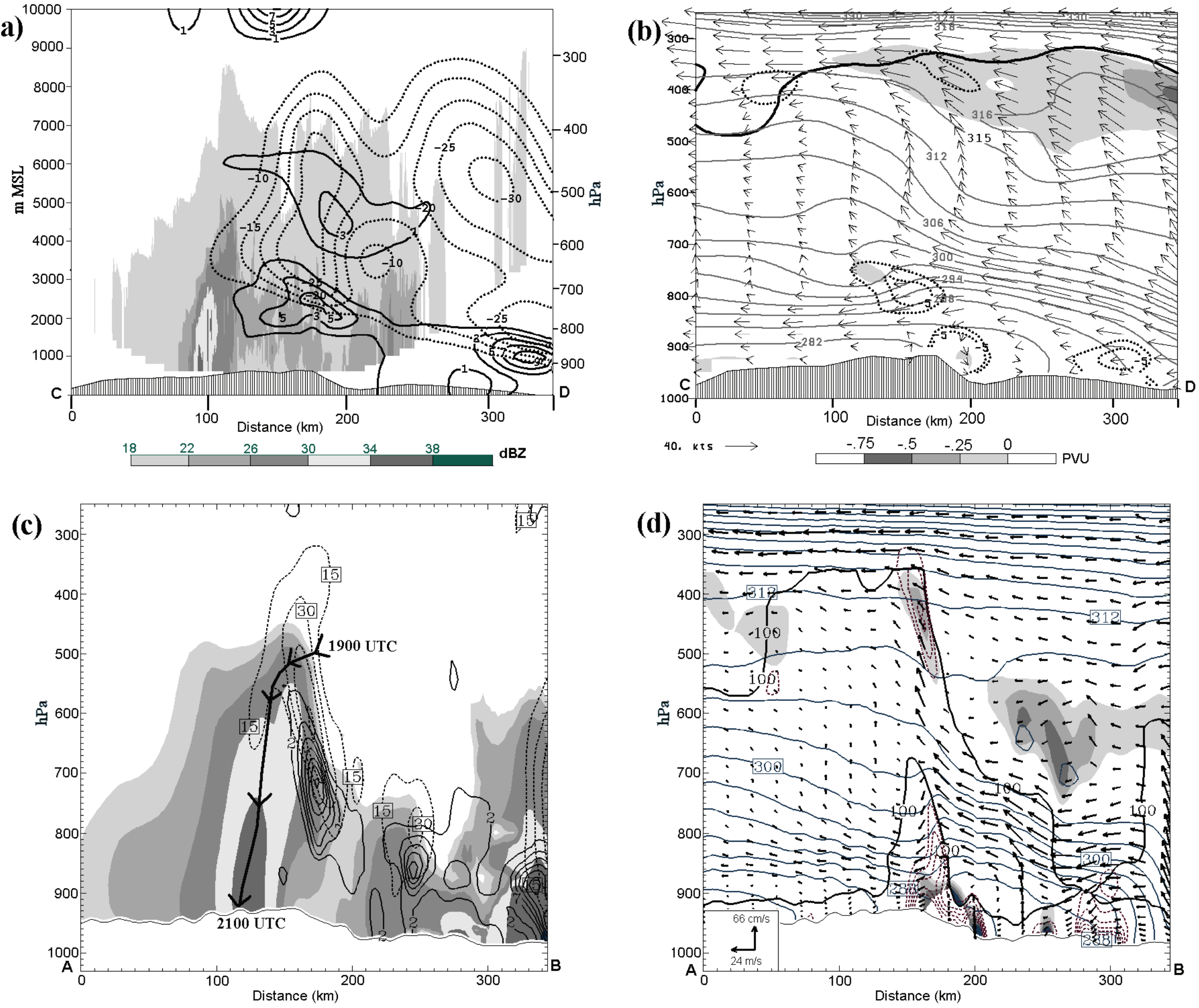

Figure 2.12 (a) KENX WSR-88D radar reflectivity cross section (orientation shown in Fig. 2.11a) valid at 2101 UTC 25 Dec 2002 with the 2100 UTC Eta analysis Petterssen frontogenesis [solid, positive values contoured every 2ºC (100 km)$^{-1}$ (h)$^{-1}$, starting at 1ºC (100 km)$^{-1}$ (h)$^{-1}$], and ascent (dotted, contoured every 5 cm s^{-1} starting at 10 cm s^{-1}). (b) Cross section as in (a), with saturation equivalent potential vorticity (shaded where negative according to scale), saturation equivalent potential temperature (gray solid, contoured every 3 K, except the 316 K potential temperature contour added for clarity), velocity in the plane of the cross section (arrows), absolute vorticity (dotted, contoured where negative every 5 x 10^{-5} s^{-1}), and the 100% contour of relative humidity w.r.t. ice (thick solid). (c) 4-km MM5 21-h forecast cross section (orientation shown in Fig. 2.11b) showing simulated reflectivity [shaded according to scale, as in (a)], Petterssen frontogenesis [black solid, positive values contoured every 4ºC (100 km)$^{-1}$ (h)$^{-1}$, starting at 2.0ºC (100 km)$^{-1}$ (h)$^{-1}$], ascent (dotted, contoured every 15 cm s^{-1} starting at 15 cm s^{-1}), and the 1900–2100 UTC 25 Dec 2002 hydrometer trajectory in the plane of the cross section (bold, arrows drawn every 0.5 h). (d) As in (b), except for the 4-km MM5 18-h forecast along section A-B (orientation shown in Fig. 2.11b).

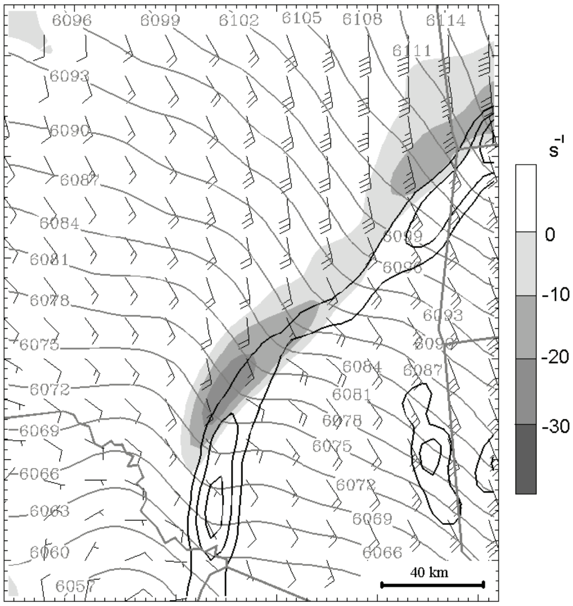

Figure 2.13 4-km MM5 21-h forecast 450-hPa absolute vorticity (shaded where negative according to scale every 10 x 10^{-5} s^{-1}), geopotential height (gray solid, contoured every 3 m), winds (full barb = 5 m s^{-1}), and 700–500-hPa layer-averaged condensational heating rate (thin solid, contoured every 1°C h^{-1}, starting at 0°C h^{-1}).

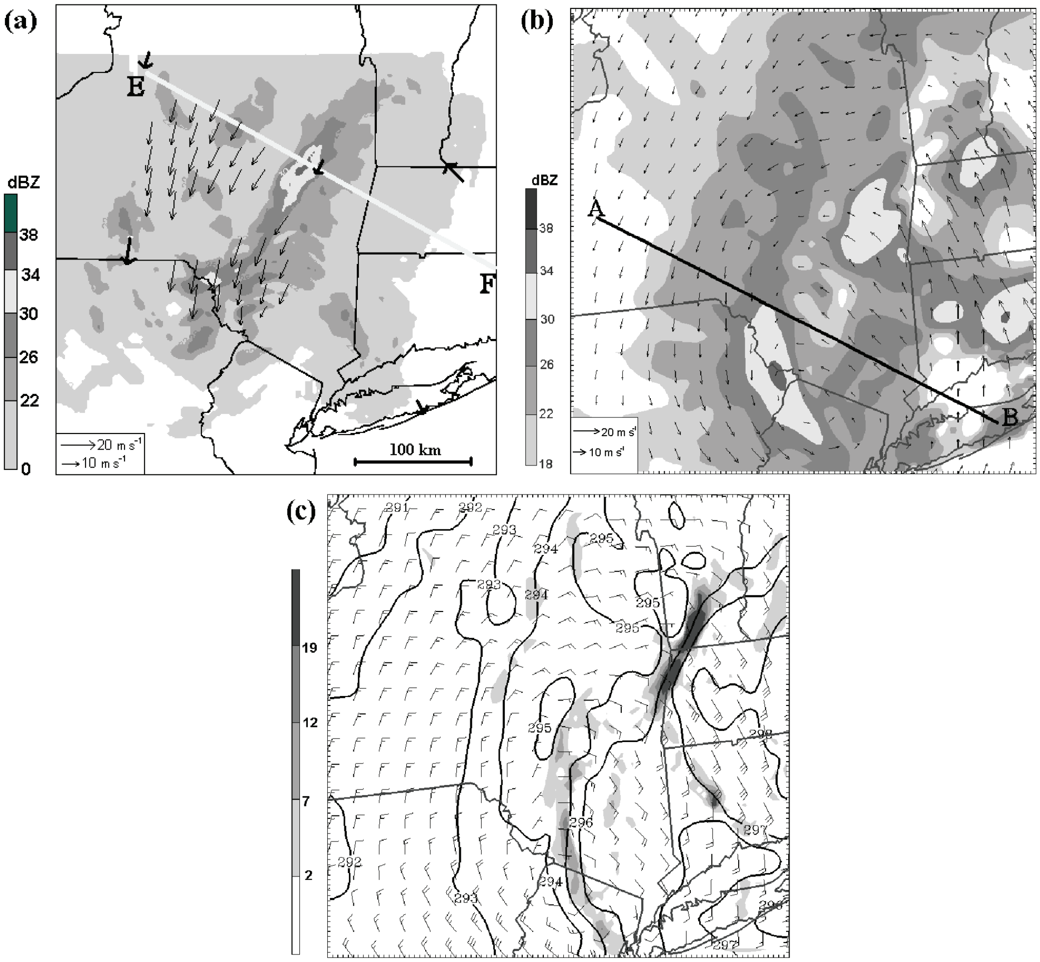

Figure 2.14 (a) As in Fig. 2.7a, except valid at 2359 UTC 25 Dec 2002. (b,c) As in Figs. 2.7b,c, except 4-km MM5 23-h forecast valid at 2300 UTC 25 Dec 2002.

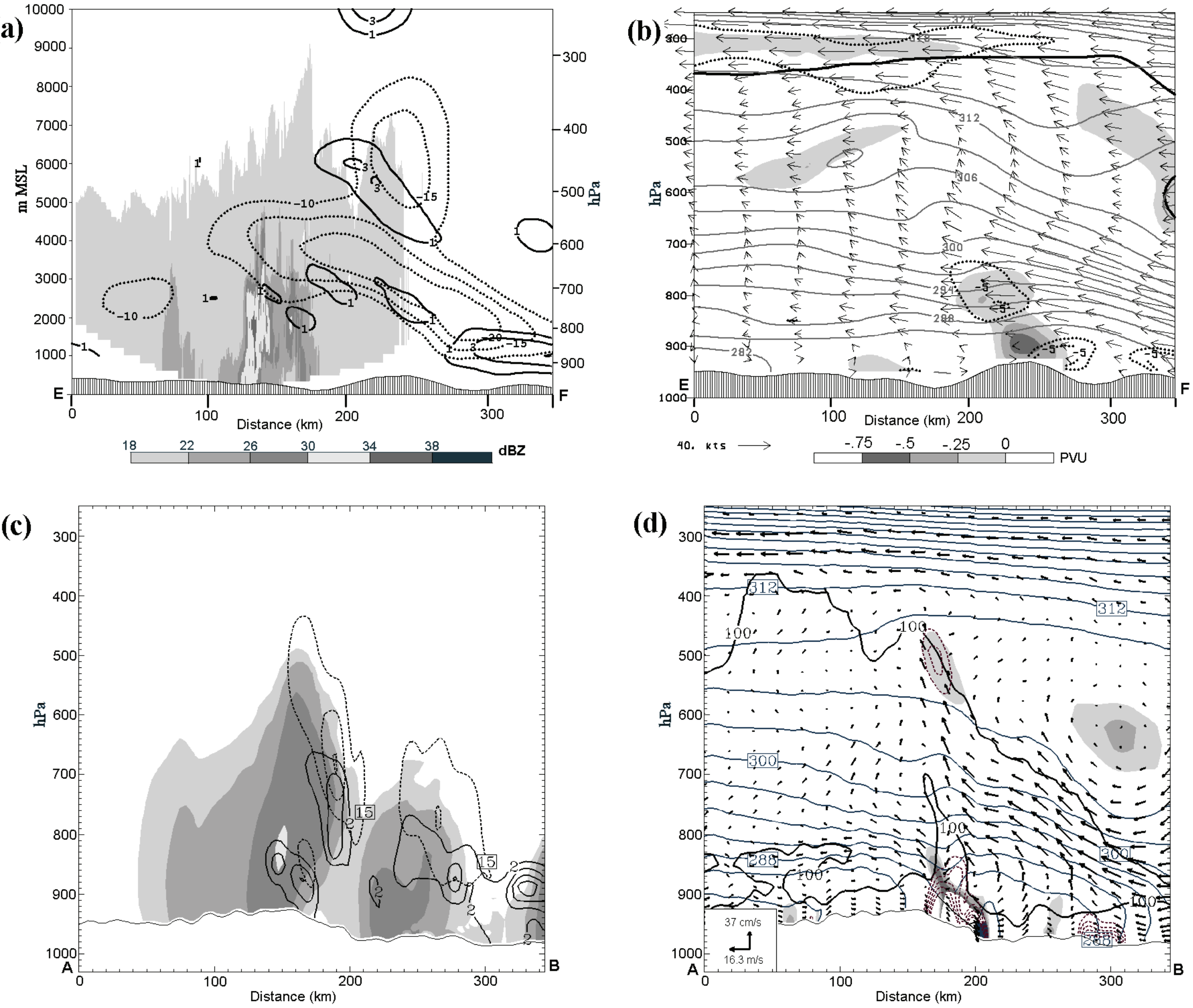

Figure 2.15 (a,b) As in Figs. 2.12a,b, except KENX WSR-88D radar reflectivity cross section (orientation shown in Fig. 14a) valid at 2359 UTC 25 Dec 2002, and Eta analysis fields valid at 0000 UTC 26 Dec 2002. (c,d) As in Figs. 2.12c,d, except 4-km MM5 23-h forecast valid at 2300 UTC 26 Dec 2002.

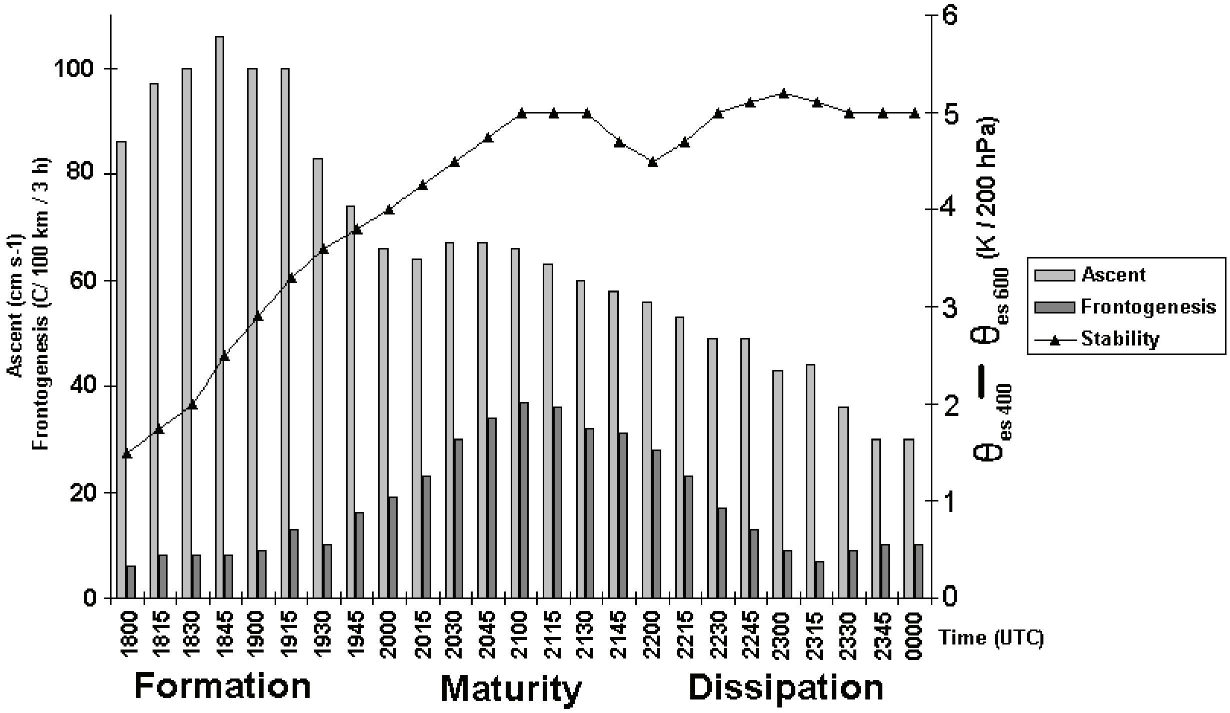

Figure 2.16 Time series of midlevel ascent maximum, Petterssen frontogenesis maximum, and conditional stability in the immediate vicinity of the simulated band. See text for details.

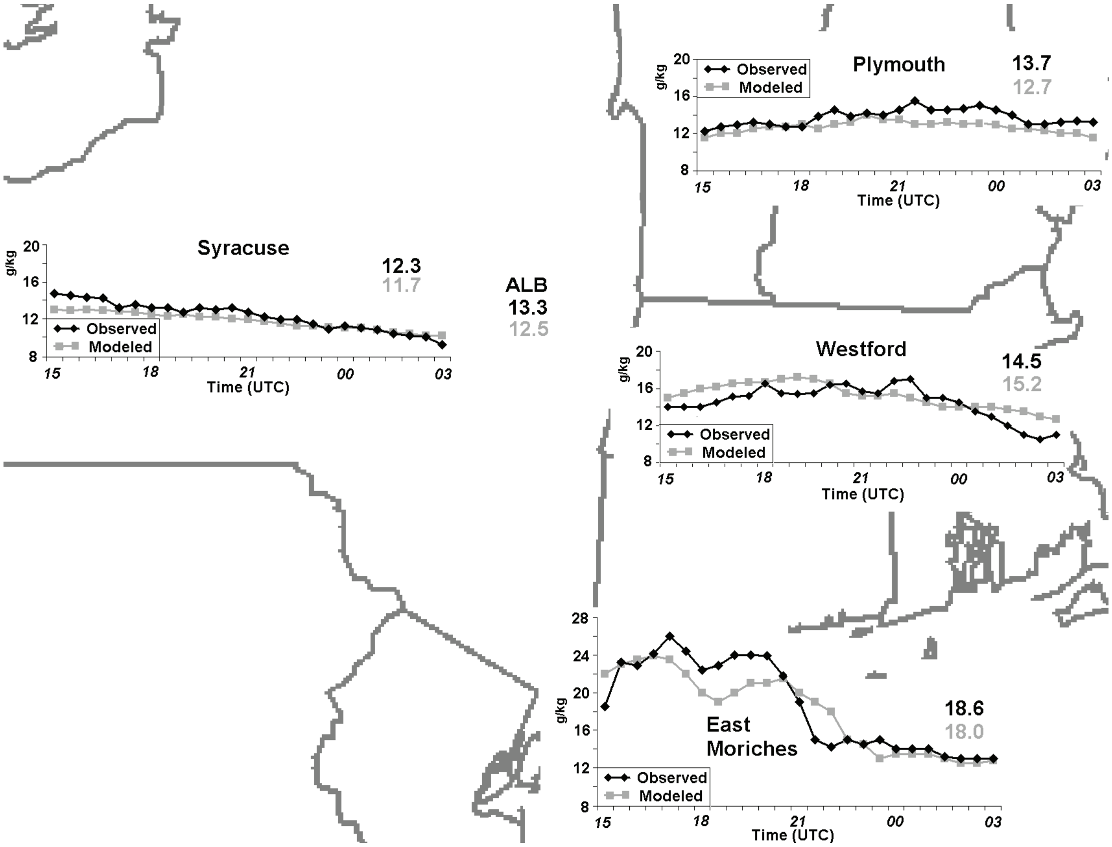

Figure 2.17 Time series comparison of 12-km MM5 forecast versus observed integrated precipitable water vapor (g kg^{-1}) from 1500 UTC 25 Dec to 0300 UTC 26 Dec 2002 for Syracuse, New York, Plymouth, New Hampshire, Westford, Massachusetts, and East Moriches, New York. Mean observed (black) and forecast (gray) values during the time series are shown in upper-right corner of each graph. 0000 UTC 26 Dec 2002 values from the Albany, New York (ALB) operational radiosonde release are also shown.

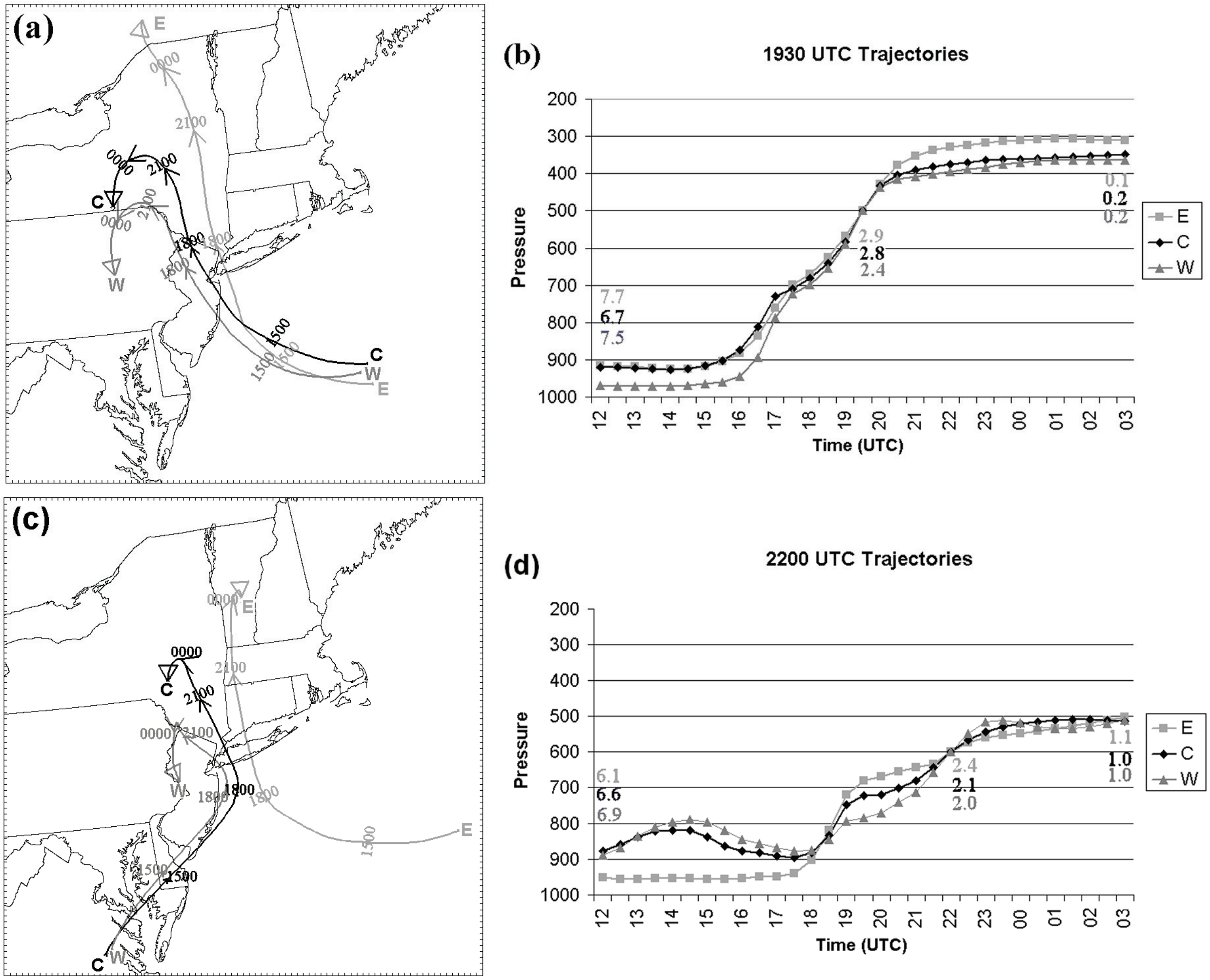

Figure 2.18 (a) 12-km MM5 forecast parcel trajectories passing through the band updraft at 1930 UTC. Time (UTC) labeled on each trajectory path. (b) Time series of parcel trajectory pressure plotted every 0.5 h. Parcel mixing ratios (g kg^{-1}) labeled at the initial time, the final time, and at the time when the parcels reach 600 hPa in the band updraft. (c,d) As in (a,b), except for parcel trajectories passing through the band updraft at 2200 UTC 25 Dec 2002.

Chapter III:

The Role of Moist Processes in Mesoscale Band Formation and Evolution

3.1 Introduction

The case study presented in chapter 2 of the 25 Dec 2002 snowstorm over the northeast U.S. showed that prior to band formation, conditional stability was small while the forcing for ascent increased along a mesoscale trough extending poleward of the 700-hPa low. During band formation the frontal environment was marked by a region of elevated conditional and inertial instability and increasing frontogenesis. Increasing conditional stability and diminishing frontogenesis characterized band dissipation. Documentation of such a band life-cycle is important, however, this chapter focuses on why the frontogenesis and stability evolved in this manner.

As reviewed in section 1.1b, moist processes are critical to cyclone development (e.g., Reed and Kuo 1988; Davis 1992; Stoelinga 1996), and such processes may also be critical to precipitation band evolution. This chapter builds on the description of the evolution of an intense banded event presented in chapter 2 to answer the following specific questions:

- What role do moist processes play in the genesis and evolution of the midlevel frontogenesis maximum in the comma head of banded cyclones?
- What influence does latent heating release (LHR) associated with the band have on band evolution?
- What processes are responsible for reducing conditional stability prior to band formation?

The same triply-nested modeling system (36, 12 and 4 km grid spacing) used in chapter 2 will be used in this chapter to conduct piecewise PV inversions, modeling experiments, and a θ tendency budget for the 25 Dec 2002 snowstorm to answer the above questions. The methods used to investigate the 25 Dec 2002 snowstorm are also applied to two additional cases to further generalize the results. Section 3.2 describes the methods used in the study. Sections 3.3 and 3.4 present analysis of the frontogenesis forcing and stability evolution of the 25 Dec 2002 snowstorm, respectively. Section 3.5 presents results from two other major banded snowstorms. A discussion and conclusions are provided in section 3.6.

3.2 Datasets and methodology

The realistic simulation of the 25 Dec 2002 snowstorm presented in chapter 2 is used as the "control run" in this study. The simulation was accomplished using the fifth-generation Pennsylvania State University–National Center for Atmospheric Research (NCAR) Mesoscale Model (MM5) (Dudhia 1993) in a nested configuration at 36, 12, and 4 km grid spacing. The run was initialized at 0000 UTC 25 Dec 2002 (hereafter, times will be abbreviated "time UTC/day" – 0000/25 in this circumstance), which is approximately 19.5 h prior to band formation.

The processes responsible for the midlevel trough evolution and associated frontogenesis evolution are investigated using the piecewise PV inversion technique of Davis and Emanuel (1991), and other modeling experiments. The stability evolution is investigated via application of a θ tendency budget and model trajectory analysis in section 3.4. These techniques are also applied to two additional cases to explore the generality of the results.

a. Piecewise potential vorticity inversion

This study applies piecewise PV inversion at 12-km grid spacing in the framework of nonlinear balanced dynamics (Charney 1955). Chapter 2 showed that the first order attributes of a mesoscale band can be realistically simulated at 12 km horizontal grid spacing. Tests using a 36 km PV inversion showed qualitatively similar results to the 12-km inversion (height minima, and wind and frontogenesis maxima in the same locations), except that the 12 km inversion exhibited more realistic shapes and amplitudes of features. To facilitate numerical convergence for the 12 km inversion, the 12 km height field was smoothed using a 25 point smoother and the 12 km domain used in chapter 2 was expanded (Fig. 3.1). Sensitivity tests confirm that expanding the domain size had little impact on the band evolution and cyclone depth (within 1 hPa of the chapter 2 run).

As applied in McTaggart-Cowan et al. (2006, 1738–1742), PV and θ perturbations are taken relative to a basic zonal baroclinic state consistent with Eady model constraints (Eady 1949), with a constant buoyancy (N^2= 0.015 s^{-2}, where *N* is the Brunt-Vaisala frequency), vertical shear (2.5 m s^{-1} km^{-1}), and meridional temperature gradient [0.6 K (100 km)$^{-1}$]. The PV perturbations (q') and θ perturbations (θ') are defined by subtracting the basic state PV and θ fields from the modeled PV and θ fields, respectively. The q' field was separated into four parts: upper-level (q_u'), which includes all q' above and including 500 hPa; lower boundary (q_l'), which includes the θ' at 950 hPa; moist interior (q_m'), which includes all q' between 950 and 550 hPa where the RH was ≥ 70%, and dry interior (q_d'), which includes the remaining q' in the 950–550 hPa layer. The q_m' generally represents PV associated with diabatic process occurring in the 950–550 hPa layer.

To further identify the kinematic contribution of each PV piece to the forcing for ascent, piecewise frontogenesis (Morgan 1999; Korner and Martin 2000) was employed. In this method, the Petterssen (1936) 2D frontogenesis equation (see eqn. 2.1) is calculated from the induced flow from a particular PV piece and the control run potential temperature gradient. Thus, the kinematic contribution to frontal forcing for ascent can be attributed to specific parts of the PV field. Particular focus is placed on the 700-hPa level, since this was the level of maximum frontogenesis in the 25 Dec 2002 snowstorm (chapter 2), and it is commonly near the level of maximum frontogenesis in northeast U.S. band events (Novak et al. 2006).

b. Dry run experiments

To isolate the effect of moist processes on band evolution, a simulation identical to the control run was integrated in a fake-dry configuration. The "fake dry" run option of the MM5 system sets the temperature tendency from the microphysics and convective schemes to zero while retaining all other effects of moisture (Grell et al. 1995; NCAR 2005). This run is termed the "dry run." Comparison of the dry and control runs shows the cumulative effect of LHR, and identifies the kinematic and potential temperature contributions of LHR to the midlevel frontogenesis. A second run ("delayed-dry run") was restarted with the 18 h forecast from the control run (1.5 h prior to band formation) and was integrated in a fake-dry configuration. Thus, the difference between the control and delayed-dry runs represents the cumulative effect of LHR between 1800/25 and the specified time after 1800/25.

3.3 Frontogenetical forcing evolution

Chapter 2 provided a detailed description of the evolution of the 25 Dec 2002 snowstorm. This section focuses on the frontogenetical forcing evolution of the snowstorm. Cyclone development in the 25 Dec 2002 snowstorm was similar to a Miller type-B cyclogenesis event (Miller 1946), characterized by coastal redevelopment of a surface cyclone as a 500-hPa trough approaches the eastern U.S. A 700-hPa trough developed to the north of the midlevel low, and served as a focus for frontogenesis and subsequent snowband formation.

Figure 3.2 shows the observed and simulated radar reflectivity as derived in chapter 2, 700-hPa height, and 2D frontogenesis evolution during the 0900–1800/25 time period. The end of this period precedes band formation by 1.5 h. At 0900/25 (Fig 3.2a), the 700-hPa low was over Ohio, supporting southwest geostrophic flow over the mid-Atlantic and Northeast U.S. A region of heavy precipitation was observed in southern Virginia, which moved into northern Virginia and expanded in size by 1200/25 (Fig. 3.2b). A small area of 700-hPa frontogenesis was found in southern Pennsylvania at this time. During the 1200–1800/25 period (not shown), the area of heavy precipitation continued to expand and move northward, and was associated with an increase in midlevel frontogenesis over eastern Pennsylvania. By 1800/25, a 700-hPa low had formed over eastern Pennsylvania (Fig. 3.2c). A sharp trough (trough A) extended from the 700-hPa low center to southern New Hampshire, and served as a focus for frontogenesis and heavy snowfall (Fig. 3.2c). This trough developed and began to move north during the 1500–1800/25 period (not shown). Two other 700-hPa height troughs were evident at 1800/25, one extending southeast from the low center (trough B) and another extending northwest (trough C). Trough C weakened with time as the coastal low developed, and will not be further discussed. The MM5 simulation at 12-km grid spacing exhibited a similar reflectivity, height, and frontogenesis evolution to the observed evolution (Figs. 3.2d–f).

Band formation occurred near trough A at ~1930/25. Figure 3.3 shows the mature and weakening stages of the band. At 2100/25 (Fig. 3.3a) the intense snowband was evident near the frontogenesis maximum along trough A. The 700-hPa frontogenesis maximum was nearly double of that just 3 h earlier in both the analysis (cf. Figs. 3.2c and 3.3a) and model forecasts (cf. Figs. 3.2f and 3.3c), associated with a robust cyclonic wind shift along trough A near the band.

By 0000/26, the analyzed and modeled 700-hPa frontogenesis maximum began to weaken as the 700-hPa trough became less defined (Figs. 3.3b,d). A comparison of the 700-hPa height falls during band formation and dissipation shows that there were large hourly height falls along trough A at 1800/25 (Fig. 3.4a), while height falls had shifted off the New England coast by 0000/25 (Fig. 3.4b). Deformation decreased along trough A during this period as the flow became more symmetric. For example, average deformation values of 20 x 10^{-5} s^{-1} were calculated within a 1.5° x 2° latitude–longitude box along trough A at 1800/25, but were only 12 x10^{-5} s^{-1} along the remnant trough A in western New England at 0000/26 (box locations shown in Fig. 3.4).

Overall, the simulated reflectivity, height, and frontogenesis evolution at 12-km grid spacing was close to the observed evolution throughout the event (Figs. 3.2 and 3.3; see also Fig. 2.4). Thus, the genesis and evolution of the midlevel frontogenesis maximum was examined via piecewise PV inversion and model experiments, as described in section 3.2. Results of the full inversion at 1800/25 for the 700-hPa height, wind, and associated frontogenesis are shown in Fig. 3.5. Since the inversion relies on nonlinear balance and is a smoothing process, an exact correspondence between the simulated and inverted fields is not expected. The full inversion surface cyclone was slightly deeper than the modeled cyclone (~5 hPa), but exhibited a track and evolution that was otherwise nearly identical (not shown). Overall, the inverted 700-hPa low center is ~45 m deeper than the control run; however, both troughs A and B are evident in the inverted height fields, as well as the frontogenesis maximum just north of trough A (Fig. 3.5). The successful replication of the frontogenesis maximum associated with trough A facilitates piecewise PV analysis of its formation and evolution.

The percentage that each PV piece contributed to the maximum 700-hPa negative height perturbation (i.e., low) during the 1500/25–0000/26 time period was analyzed (not shown). The q_u’ explained a majority (50–80%) of the height perturbation, while the q_m’ term explained more than 25%. The q_d’ and q_l’ terms explained less than 10%. Given the dominance of the q_u’ and q_m’ in explaining the 700-hPa low, further analysis of the contribution of these PV anomalies’ to the forcing evolution is presented at a representative lower (700 hPa) and upper (400 hPa) level.

a. *Band formation*

At 0900/25, 10.5 h prior to band formation, the 400-hPa q_u’ field exhibited a maximum over western North Carolina (Fig. 3.6a). Strong positive PV advection was located to the east of this maximum (Fig. 3.6a), forcing height falls, ascent (e.g., Bluestein 1993; Nielsen-Gammon and Lefevre 1996; Hakim et al. 1996), and associated precipitation over south-central Virginia (Figs. 3.2a,d). The developing precipitation was associated with latent heating[2] in the 400–800-hPa layer (Fig. 3.7a). Meanwhile, the 700-hPa q_m’ field exhibited an elongated maximum in northwestern Ohio associated with the primary cyclone (Fig. 3.6b), and a small arc in eastern Ohio associated with the parent cyclone’s occlusion.

---

[2] Calculated in Fig. 3.7 as heating due to condensation and deposition in regions of explicitly resolved saturated ascent via $\frac{\partial\theta}{\partial t} = \left(\frac{R_m\theta}{g \cdot p}\right) \cdot \omega(\Gamma_m - \Gamma_d)$, where Rm is the gas constant for water vapor, g is gravity, p is the pressure, ω is vertical velocity in pressure coordinates, Γ_m the moist adiabatic lapse rate and Γ_d the dry adiabatic lapse rate.

Three hours later at 1200/25, a small upper PV filament (U1) developed in the 400-hPa q_u' field over eastern Virginia (Fig. 3.6c). U1 appears to have formed as a consequence of the diabatic redistribution of PV. For example, at 700 hPa, the q_m' field exhibited a newly-formed local diabatic PV maximum (L1) in the vicinity of U1 (Fig. 3.6d). L1 was associated with the developing precipitation shield (Fig. 3.2e) in the region of enhanced positive upper PV advection and ascent associated with U1 (Figs. 3.6c and 7b). L1 exhibited perturbation PV values exceeding 2 PVU, and large latent heating in its vicinity (Fig. 3.7b). The associated LHR reduced PV downshear of L1 (x=300–400 km) in the 300–400-hPa layer, effectively increasing the slope of the tropopause and associated PV advection (Fig. 3.7b). The inverted 700-hPa height, wind, and frontogenesis fields associated with the q_u' and q_m' indicate 700-hPa frontogenesis was induced by the q_m' over northern Virginia and central Pennsylvania (Figs. 3.8a,b).

During the next 6 h (1200–1800/25), U1 amplified and moved north in tandem with L1 as trough A formed. By 1800/25, just 1.5 h prior to band formation, a PV hook had developed, with a "notch" of low 400-hPa q' values over southern Pennsylvania (Fig. 3.6e). This upper PV notch indicates the development of a trowal (e.g., Martin 1998a). At this time U1 represented the sharp poleward edge of the PV hook, which was elongated towards the northeast. Positive PV advection was located on the poleward edge of U1 (Fig. 3.6e), along a similar axis as the newly formed trough A (e.g., Fig. 3.2f). L1 moved north into northern New Jersey and became deformed along a northeast–southwest oriented axis by 1800/25 (Fig. 3.6f), corresponding to trough A. At 1800/25, L1 continued to be associated with latent heating and was positioned beneath the region of enhanced PV advection associated with U1 (Fig. 3.7c). The PV inversion showed that negative 700-hPa height anomalies associated with the q_u' field had increased along an axis nearly collocated with trough A (Fig. 3.8c). The wind field associated with the q_u' supported a band of frontogenetical forcing along trough A; however, a majority of the 700-hPa frontogenesis along troughs A and B was associated with the q_m' (Figs. 3.8c,d).

The role of LHR in the formation of the midlevel frontogenesis maximum is highlighted by a comparison of the control and dry runs at 1800/25 (Figs. 3.9a,b). Troughs A and B were considerably less sharp in the dry run (Figs. 3.9a,b). Consequently, frontogenetical forcing along trough A was nearly 4 times weaker in the dry run than the control run at this time, and band formation failed to occur. Comparison of the upper PV distribution shows that the control run PV hook has a sharper poleward edge and is more elongated toward the northeast (Figs. 3.9c,d), which is evidence of diabatic PV redistribution in the control run. However, the upper PV anomaly in the dry-run does exhibit a broad elongation toward the southern New England coast (Fig. 3.9d), contributing to a weak trough A and associated weak frontogenesis (Fig. 3.9b). The dry run does not exhibit L1 (Fig. 3.9f), further confirming the diabatic nature of L1.

In summary, strong forcing for ascent ahead of the upper PV anomaly created a small area of precipitation over southern Virginia. LHR associated with this precipitation created an elongation in the upper PV distribution (U1) and a small midlevel diabatic PV anomaly (L1). Once U1 and L1 formed, they simultaneously modified the upper and interior PV distributions, leading to mutual amplification and upscale growth. The anomalies exhibited a northeast-southwest orientation which supported larger height falls along this axis and the formation of trough A. Trough A subsequently served as a focus for frontogenesis and band formation.

b. *Band maturity*

At 2100/25, an intense band was present in eastern New York (Figs. 3.3a,c). Positive PV advection (favoring ascent and height falls) occurred on the poleward edge of the PV hook (U1) over eastern New York at 400 hPa (Fig. 3.10a). Inversion of the q_u' showed negative 700-hPa height anomalies in eastern New York elongated along a northeast–southwest orientation (Fig. 3.10c). Note that this orientation is similar to the orientation of trough A (Figs. 3.10c and 3.3c). The induced frontogenesis exceeded 2°C $(100\ \mathrm{km})^{-1}$ $(3\ \mathrm{h})^{-1}$ in eastern New York (Fig. 3.10c), which was ~40% of the frontogenesis induced by the total balanced flow.

The q_m' at 700 hPa shows that L1 oriented along a northeast–southwest axis in eastern New York (Fig. 3.10b) parallel to trough A and the precipitation band (Fig. 3.3c). L1 remained beneath the region of upper PV advection associated with U1 (Fig. 3.7d). Frontogenesis induced by q_m' increased to values exceeding 3°C $(100\ \mathrm{km})^{-1}$ $(3\ \mathrm{h})^{-1}$ along trough A in southeast New York (Fig. 3.10d), which is ~60% of the frontogenesis induced by the total balanced flow. To isolate the impact the PV anomaly generated by the precipitation band (L1) had on trough A and the associated frontogenesis, the q_m' in the 800–500-hPa layer in a 3.5° x 4.5° latitude–longitude box centered on the band was inverted (box shown in Fig. 3.10b). The resultant inverted 700-hPa height and wind field show negative height perturbations exceeding 10 m along the band, with an induced cyclonic circulation (Fig. 3.11). The induced frontogenesis accounts for ~60% of the total q_m' induced frontogenesis in southeast New York and ~35% of the frontogenesis induced by the total balanced flow. These results demonstrate that diabatic heating from the band itself contributed to amplification of the frontogenetical forcing during band maturity.

Figure 3.12 shows a comparison of the control and delayed-dry run at 2100/25. This time is 3 h after latent heating was turned off in the delayed-dry run, and 1.5 h after band formation occurred in the control run. A much weaker band occurred in the delayed-dry run than in the control run, illustrating the critical role LHR plays in band formation and maintenance, even given an initially favorable flow field just 1.5 h prior to band formation. In particular, the heights in eastern New York in the delayed-dry run at 2100/25 are ~15 m higher than the control run, consistent with the PV inversion results (i.e., Fig. 3.11). As a result, the midlevel trough is less defined, and the frontogenesis maximum is ~3 times weaker in the delayed-dry run compared to the control run. Explicit differences in the wind and temperature (control minus delayed dry) show strong flow convergence in eastern New York, and a local temperature difference exceeding 4°C over southern New England (Fig. 3.12c).

Normalized frontogenesis (Schultz 2004):

$$F_{norm} = \frac{F}{|\nabla\theta|} \tag{3.1}$$

was calculated to separate the roles of the potential temperature gradient and kinematic flow in frontogenesis. Calculation of normalized frontogenesis reveals that the change in kinematic flow between the control and dry runs accounts for ~60% of the change in the frontogenesis maximum between these runs, while the change in temperature gradient accounted for the remaining ~40% of the change in the frontogenesis maximum. Thus, LHR during the 1800–2100/25 period both altered the flow (creating large deformation and convergence) and enhanced the temperature gradient, resulting in intense frontogenesis in the band region. These results further highlight the critical role of moist processes in the formation and maintenance of the band.

c. Band dissipation

Given that LHR associated with the precipitation band enhanced the frontogentical forcing, what led to band dissipation? As noted in section 3.3, the largest height falls shifted east of trough A during band dissipation (Fig. 3.4), creating a more symmetric midlevel height field and reducing the deformation, convergence, and associated frontogenesis. To explore what caused the eastward displacement of the 700-hPa height falls, the piecewise PV inversion results during the 2100/25−0000/26 period were analyzed.

At 2100/25 the q_u’ field exhibited a small bulge (U2) along the perturbation PV tail off the Atlantic coast (Fig. 3.10a). The q_m’ field showed a small anomaly (L2) near U2 (Fig. 3.10b), suggesting PV was redistributed by LHR. A temperature difference maximum between the control and delayed-dry run off the Virginia coast is found near L2 (Fig. 3.12c), providing further evidence of LHR. Frontogenesis induced by L2 is also evident in this region (Fig. 3.10d).

Three hours later at 0000/26, U2 had developed into a well-defined filament off the southern New England coast, with an attendant low PV notch (Fig. 3.13a). Positive PV advection was found on the poleward edge of U2 (Fig. 3.13a), supporting large height falls in this region. The q_u’ field was responsible for 700-hPa frontogenesis along the remnant trough A in western New England and near U2 off the coast (Fig. 3.13c). At lower levels, L2 had grown in amplitude and size over the last 3 h (cf. Figs. 3.10b and 3.13b). Accordingly, the inverted 0000/26 q_m’ field exhibited strong frontogenesis near L2 southeast of the New England coast (Fig. 3.13d). However, frontogenesis associated with the q_m’ field in western New England was nearly absent (Fig. 3.13d).

To quantify the effect of L2 on the frontogenesis in western New England at 0000/26, the q_m’ in a 3.5° x 4.5° latitude–longitude box surrounding L2 was inverted at 2200/25 and 0000/26 when the frontogenesis was weakening (see Fig. 2.16). The 0000/26 inversion box is shown in Fig. 3.13b, and was adjusted 1.5° south for the 2200/25 inversion to account for the location of L2. The inversions show that L2 was responsible for inducing a *frontolytic* flow in western New England that grew in amplitude through time (Figs. 3.14a,c). Separate inversions of q_u’ in the same respective boxes showed negligible frontolysis (Figs. 3.14b,c). Other inversions of q_m’ in the Gulf of Maine and q_d’ in the dry slot (not shown) also resulted in negligible frontolysis. Thus, band dissipation was primarily caused by the formation and upscale growth of L2 east of the band. This anomaly created larger height falls off the southeast New England coast than along the former trough A. The result was a more symmetric height and wind field over western New England and associated weaker frontogenetical forcing.

3.4 Stability evolution

As shown in section 2.4, the 25 Dec 2002 snowstorm exhibited a deep layer of conditional neutrality, with an embedded layer of conditional instability near 500 hPa in the immediate band environment prior to band formation. For example, at 1800/25 (~90 min prior to band formation), a region of heavy precipitation and midlevel convergent flow occurred over eastern New York and Pennsylvania (Fig. 3.15a). A cross section through the heavy precipitation region (Fig. 3.15b) shows a region of near-neutral conditional stability in the 600–350-hPa layer. A spatial view of the 470–600-hPa θ_{es} difference at1800/25 shows a region of negative values [indicative of conditional instability (CI)] over southeast New York (Fig. 3.15c). This region of CI was associated with the developing dry slot (not shown). However, an isolated region of negative values was also evident near the New York–Pennsylvania–New Jersey border, near where the precipitation band would form 90 min later. The conditional stability was restored during band formation and remained stable throughout the subsequent band duration (e.g., Fig. 2.16).

To explore the stability evolution, a θ tendency budget was calculated. A θ budget was calculated as opposed to a saturated equivalent potential temperature (θ_{es}) budget to more easily separate the impact of diabatic heating from temperature advections. The Pearson correlation coefficient (Wilks 1995, 45–50) between θ and θ_{es} was 0.99, further justifying use of the θ tendency as a proxy for the θ_{es} tendency in this case. The θ tendency equation (Carlson 1991, eq. 1.13c),

$$\frac{\partial \theta}{\partial t} - \underset{\text{A}}{-\left(u\frac{\partial \theta}{\partial x} + v\frac{\partial \theta}{\partial y}\right)} - \underset{\text{B}}{\omega\frac{\partial \theta}{\partial p}} + \underset{\text{C}}{\frac{Q}{c_p}\left(\frac{\theta}{T}\right)} \quad , \tag{3.2}$$

was evaluated using 5 min output from the model on the 4-km domain with explicit convection, where *u* and *v* are components of the vector wind, *p* the pressure, ω the vertical velocity and *Q* the diabatic heating rate. Term A represents horizontal advection, term B represents vertical advection, and term C represents diabatic heating. Term C is composed of heating/cooling from diabatic processes included in the microphysics, radiation, and boundary layer schemes. An additional diffusional correction term is applied in the MM5, and is considered part of term C for simplicity. On average >90% of the total magnitude of term C was from latent heating due to cloud processes (derived from the microphysics scheme), and therefore all other heating processes were combined into an "other" category. Thus, the terms assessed in the θ budget were the local θ tendency, horizontal θ advection (term A), vertical θ advection (term B), latent heating due to cloud processes, and heating due to other processes. Differences between terms at two levels provided a stability tendency budget, which could be assessed through time.

The budget was analyzed for a 4x4 grid-point box (256 km^2) within the negative EPV region just southeast of the band formation location in the 470−600-hPa layer, where CI was present (e.g., Fig. 3.15a). Sensitivity tests confirm that shifting the analysis box location two grid points to the northeast or southwest (remaining along the axis of negative EPV) does not change the results. A time series of the 470–600-hPa θ difference, and difference tendency between 1200/25 and 2000/25 is shown in Fig. 3.16. Three distinct stability tendency regimes are evident. Destabilization occurred between 1200−1400/25 as the 470–600-hPa θ difference decreased from 7 K to 4 K. CI developed in the 500−575-hPa layer during this period (not shown). Between 1400/25 and 1900/25 the weak stability was maintained, with the 470–600-hPa θ difference remaining around 5.5 K. The stability sharply increased during the 1900–2000/25 period, as band formation occurred.

Analysis of the individual terms in the 470–600-hPa layer during the 1200–1400/25 period of destabilization (Table 3.1) shows that differential horizontal advection contributed to destabilization, while differential vertical advection partially offset the destabilization. Analysis of the individual levels revealed that stronger warm air advection occurred at 600 hPa than at 470 hPa (not shown), while there was stronger ascent and associated vertical advection of lower θ at 470 hPa than at 600 hPa. During the period of small stability maintenance (1400–1900/25), terms fluctuated in sign, with differential vertical advection typically opposing differential latent heating (Table 3.1). During the period of rapid stabilization (1900–2000/25), differential temperature advection (small warm air advection above, cold air advection below) was the primary term contributing to stabilization (Table 3.1), partially offset by differential latent heating and vertical advection. Although on average differential vertical advection was a slight destabilizing term during this period, it was a strong stabilizing term during 1930–2000 UTC, coinciding with the period of band formation. This result is consistent with the release of CI as diagnosed in chapter 2.

To view processes reducing the conditional stability in a Lagrangian framework, 6-h backward trajectories at the top and bottom of the conditionally unstable layer at the analysis location were also calculated. The trajectories were obtained using a 5-min time step interpolated from 15-minute output on the 12-km domain. Trajectories illustrate that the upper and lower parcels arriving at the analysis location during the 1200–1400/25 period originated southwest of the analysis location (Figs. 3.17a,b). Cross sections exhibited a shallow layer of conditional instability between 500 and 600 hPa and a deeper layer of potential instability between 700 and 500 hPa in the vicinity of where the parcels originated (not shown). Trajectories ending at 1400/25 show that the upper parcel became saturated as the layer experienced sustained ascent (Fig. 3.17b). The upper parcel θ was conserved during its advance (not shown), suggesting dry adiabatic ascent, while the θ of the lower saturated parcel increased 2.6 K (not shown) in association with LHR. Thus, the advection and lifting of a potentially unstable layer account for conditional stability reduction during the 1200–1400/25 period.

Differential moisture advection within the cyclone's dry slot has been cited as an important destabilization process associated with band events. Parcels entering the stability analysis box during the 1500–1800/25 period arrived generally from the south, and had remained saturated along their entire 6 h trajectories (Fig. 3.17c). At 2000/25 (after band formation), the upper parcel originated within the developing dry slot ~ 6 h prior (Figs. 3.17d and 3.8c), while the lower parcel remained nearly saturated during its entire advance to the analysis box (Fig. 3.17d). Thus, parcels which had advanced through the dry slot arrived in the banding region *after* the band had formed, and therefore the dry slot did not play a role in the initial stability reduction.

Trajectory analysis of parcels arriving at the stability analysis box at 2000/25 shows that the dry slot did contribute to the stability evolution after band formation. For example, 6 h prior to the parcels' arrival at the stability analysis box location (1400/25), the θ difference between the upper and lower parcel was 11.5 K (suggesting strong stability). This difference decreased to 5.6 K four hours later (1800/25) as lifting of the potentially unstable layer occurred in the dry slot. If this layer was simply advected to the analysis location, it would have maintained low stability at the analysis location. However, both parcels became saturated as they ascended in the local band environment (Fig. 3.17d), and the upper parcel experienced slightly greater ascent (~150 m more), leading to a slight increase in the θ difference to 6.5K. The parcels arrived at the analysis location with this θ difference, which was more stable than parcels arriving just 1 h earlier (5.5 K) (Fig. 3.16). Thus, ascent within the dry slot did destabilize the air that arrived in the banding region at 2000/25; however, the stabilizing effects of differential diabatic heating and differential vertical ascent in the immediate band environment offset the destabilization in this case. Presumably, the stability would have been even larger during band maturity in the absence of a dry slot in this case.

3.5 Other cases

To explore the representativeness of the above results, the methods employed in investigation of the 25 Dec 2002 snowstorm were applied to the 12 February (Feb) 2006 and 14 Feb 2007 snowstorms. An intense snowband associated with the 12 Feb 2006 snowstorm brought a record breaking 68.3 cm of snow to New York City. The 14 Feb 2007 snowstorm deposited nearly 1 m of snowfall in a narrow band in upstate New York.

As in the 25 Dec 2002 snowstorm, the analyzed mesoscale evolution of the 12 Feb 2006 and 14 Feb 2007 cases featured the formation of a midlevel (~700 hPa) low. This low is evident in the wind field over northern Delaware in the 12 Feb 2006 case (Fig. 3.18a), and northeast Pennsylvania in the 14 Feb 2007 case (Fig. 3.18b). A sharp cyclonic wind shift extends northeast from this midlevel low center in each storm (Figs. 3.18a,b), associated with a midlevel height trough (not shown). Convergence and deformation were found in the vicinity of this wind shift as strong southeast flow slowed, and backed across the trough (Figs. 3.18a,b).

Corresponding 4-km MM5 simulations [model configurations are presented in Novak et al. (2007)] show the simulated precipitation bands were within 50 km of the observed location in each case at the time of band maturity (Fig. 3.18); however, the 12 Feb 2006 simulation was time shifted 3 h earlier to obtain the best match. Similar to the observations, a sharp wind shift was evident in the model wind forecasts (Figs. 3.18c,d), associated with intense frontogenesis. These model simulations are used for further investigation.

a. Forcing evolution

The 400-hPa q'_u field 3 h prior to band formation in the 12 Feb 2006 case (1200/12) featured a synoptic-scale elongation along the eastern U.S. coast (Fig. 3.19a). PV values within the upper anomaly were ~ 2 PVU stronger than in the 25 Dec 2002 case (cf. Figs. 3.6c and 3.19a). Positive PV advection was occurring on the poleward flank of this anomaly, supporting height falls and ascent along the coast. Inversion confirms that the upper PV elongation contributes to 700-hPa trough development and frontogenesis along the coast (Fig. 3.20a). The q'_m field (Fig. 3.19b) shows a PV band along this trough, representing the effects of LHR associated with heavy precipitation developing within the region of strong upper PV advection near the coast. Inversion showed that the induced flow from the q'_m was strongly frontogenetic along the coast (Fig. 3.20c). In fact, similar to the 25 Dec 2002 case, the induced flow from the q'_m explained more than half (65%) of the total balanced frontogenesis maximum at the time of band maturity at 1800/12 (not shown). Unlike the 25 Dec 2002 case, the q'_m anomaly formed and amplified in place.

The 400-hPa q'_u field 3 h prior to band formation in the 14 Feb 2007 case (1500/14) was quite different from either the 25 Dec or 12 Feb cases, with a weak 400-hPa PV anomaly (<2.0 PVU) over Ohio and a weak trough (associated with PV <1.0 PVU) located along the coast (Fig. 3.19c). Weak PV advection was occurring on the eastern edge of these anomalies. Inversion confirmed that the q'_u field was associated with little frontogenesis (Fig. 3.20b), and accounted for less than ~10% of the total balanced 700-hPa frontogenesis maximum. In contrast, the q'_m field at the same time exhibited two strong elongated anomalies, one associated with the inland system, and another along the coast (Fig. 3.19d). The coastal anomaly had originated along the southeast U.S. coast around 0000/14. A confluent zone was formed in eastern New York between the two q'_m anomalies (see Fig. 3.19d), as the coastal anomaly induced southeast winds, while the inland anomaly induced south-southwest winds. Inversion confirmed that the flow induced by the q'_m resulted in a band a frontogenesis in central Pennsylvania (Fig. 3.20d), accounting for ~85% of the frontogenesis maximum at the time of band formation.

Similar to the 25 Dec 2002 case, both the 12 Feb 2006 and 14 Feb 2007 cases exhibited band dissipation as heights fell more rapidly to the east of the midlevel trough than along the trough. In the 12 Feb 2006 case at 2100/12 (Fig. 3.20a), positive 400-hPa PV advection was evident along the poleward edge of the upper PV elongation, which would tend to maintain the trough. Indeed, inversion of the q'_u shows induced frontogenesis in eastern New England, near the band location at this time (Fig. 3.22a). However, at lower levels a separate diabatic PV anomaly just off the New England coast developed over the past 2 h (Fig. 3.21b). This anomaly was associated with heavy precipitation and formed at the tip of the upper PV elongation (Figs. 3.21a,b). The inverted q'_m height field is elongated towards this feature, and frontogenesis induced by q'_m is limited to the Maine coast, in the vicinity of this feature (Fig. 3.22c). Separate inversion of this diabatic PV anomaly (located within box 1 in Fig. 3.21b) confirms that it was responsible for frontolysis in the band region (i.e., eastern New England; Fig. 3.23). Another PV anomaly exceeding 1 PVU was found at 700 hPa beneath the upper PV elongation in the cyclone's dry slot (Fig. 3.21b). Piecewise inversion of this dry slot anomaly (located within box 2 in Fig. 3.21b) confirmed that the diabatic PV anomaly in eastern New England was dominant in creating frontolysis (Fig. 3.23). Frontolysis values induced by the diabatic PV anomaly at 2100/12 were ~25% of the total balanced frontogenesis. Thus, as with the 25 Dec 2002 case, a diabatic PV anomaly helped shift height falls east of the primary band, and weakened frontogenesis in the band region.

During the 14 Feb 2007 case the coastal diabatic PV anomaly amplified and became dominant over northern New England. As the coastal anomaly amplified, the upper PV anomaly formerly over Ohio moved to the southern New England coast by 0600/15 (Fig. 3.21c). The PV advection associated with this feature over the Gulf of Maine at this time (Fig. 3.21c) contributed to 700-hPa height falls east of the primary trough in central New England, but negligible frontogenesis (Fig. 3.22b). The 700-hPa q_m' field at 0600/15 exhibited a prominent north−south maximum associated with the primary trough (Fig. 3.21d), and inversion confirmed that the q_m' field was responsible for a band of frontogenesis collocated with the band (Fig. 3.22d). However, a new PV anomaly was evident along the Maine coast (located within box 1 in Fig. 3.21d). This anomaly formed near a band of heavy precipitation along the cyclone's surface occlusion (not shown). Piecewise inversion of the q_m' within box 1 in Fig. 3.21 indicated frontolysis in the band region (Fig. 3.24a), with values ~30% of the total balanced frontogenesis. Inversion of the PV in the dry slot (i.e., q_d' within box 2 in Fig. 3.21d) indicated small height falls and little impact on the frontogenesis in the band region (Fig.

3.24b). Thus, the diabatic PV anomaly along the Maine coast helped shift height falls east of the primary band and weakened frontogenesis in the band region.

b. Stability evolution

As in the 25 Dec 2002 case, the stability evolution of the 12 Feb 2006 and 14 Feb 2007 cases were evaluated on the 4-km domain at a representative location (see Figs. 3.18c,d) within the layer of persistent small conditional stability. Based on cross sections, this layer was between 520–630 hPa and 410–550 hPa in the 12 Feb 2006 and 14 Feb 2007 cases, respectively. The stability tendency for each case is shown in Fig. 3.25. As in the 25 Dec 2002 case, the lowest conditional stability in each case occurred prior to band formation, while the stability was partially restored near the time of band formation. During the destabilizing period in all three cases, differential horizontal θ advection was the dominant destabilizing term (Tables 3.1–3.3). During the stability maintenance period just prior to band formation, differential horizontal θ advection was generally small, and the effect of differential vertical θ advection was offset by differential latent heating. During the stabilization period (generally during or after band formation), differential horizontal θ advection was dominant in the 25 Dec 2002 cases (Table 3.1), whereas differential vertical θ advection was dominant in the 14 Feb 2007 and 12 Feb 2006 cases cases (Tables 3.2 and 3.3, respectively). These results highlight the 3D nature of the stability evolution as well as the role latent heating can play in the stability evolution.

Trajectory analysis of the 12 Feb 2006 case (not shown) revealed that parcels arriving during the primary destabilization period (0000–0600/12) originated southwest of the analysis box and were saturated during their advance. After 0600/12, parcels which had experienced stability reduction within the dry slot arrived at the analysis location and contributed to the weak conditional stability during the stability maintenance period (Fig. 3.25). In the 14 Feb 2007 case, parcels remained saturated upon their advance to the analysis box at all times. Thus, the dry slot was not related to the initial stability reduction in all three examined cases. Rather, differential horizontal temperature advection in moist southwest flow ahead of the upper trough was the dominant process reducing the midlevel conditional stability.

3.6 Discussion and conclusions

The processes regulating the frontogenesis and stability evolution in the 25 Dec 2002 northeast U. S. snowstorm and two other cases were investigated using piecewise PV inversions, modeling experiments, and θ tendency budgets.

Band formation in all three cases was coincident with the sharpening of a midlevel trough to the north of a parent low, and an associated increase in frontogenesis in an environment of small conditional stability. Piecewise PV analysis showed that there are a variety of PV evolutions that contribute to band formation and evolution. For example, during the 25 Dec 2002 case, the diabatic redistribution of PV simultaneously created upper (U1) and lower (L1) PV anomalies. PV advection associated with these anomalies supported the formation of trough A and associated frontogenesis at 700 hPa. This process began ~8 h prior to band formation and ~500 km south of the band formation location. The dry run showed that LHR was critical for amplifying the trough through the simultaneous modification of the upper and lower PV distribution (Fig. 3.9). In the 12 Feb 2006 case, trough formation occurred in situ as the upper PV anomaly forced ascent along the coast and the associated diabatic PV anomaly amplified while remaining nearly stationary. In the 14 Feb 2007 case, the midlevel frontogenesis developed in the confluent flow between separate inland and coastal diabatic PV anomalies, with the coastal anomaly evolving nearly independent of the upper PV anomaly during the initial stage of the cyclone's life cycle. Common to all three cases are diabatic PV anomalies whose induced flow accounts for a majority of the midlevel frontogenesis, highlighting the importance of LHR in band evolution.

Band dissipation in all three cases occurred as new diabatic PV anomalies (associated with LHR) formed east of the primary band, creating a more symmetric midlevel flow that weakened the midlevel frontogenesis associated with the band. For example, piecewise PV analysis of the 25 Dec 2002 case showed that the formation of a new diabatic PV anomaly (i.e., L2) served to shift the height falls east of trough A, and contributed to frontolysis in the band region (Fig. 3.14). In the 12 Feb 2006 and 14 Feb 2007 cases, new diabatic PV anomalies were also responsible for the eastward shift in height falls and frontolysis. Thus band duration in each case was partially determined by when these new diabatic PV anomalies formed and how they evolved, illustrating a specific example of how moist processes can influence the lifetime of a band.

Conditional stability reduction occurred several hours prior to band formation in each case (e.g., Figs. 3.16 and 3.21). After the initial stability reduction, the stratification remained small until the release of CI during the band formation process. This stability evolution has also recently been shown by Evans and Jurewicz (2009) in a climatological study of heavy snowfall events in central New York, and suggests that the development of CI prior to band formation and subsequent release of CI during the band formation process may be relatively common. The spectrum of instabilities and their evolution will be explored further in the next chapter.

Diagnosis of the processes responsible for destabilization in each case revealed that differential horizontal θ advection in moist southwest flow ahead of the upper trough was dominant over differential vertical θ advection or latent heating in all three cases. Trajectories showed that the advection and lifting of a potentially unstable layer (not associated with the dry slot) accounted for the initial conditional stability reduction in the 25 Dec 2002 case, while differential horizontal θ advection (in a saturated environment) accounted for the initial stability reduction in the 12 Feb 2006 and 14 Feb 2007 cases. The dry slot *was not* responsible for the initial stability reduction in all three examined cases, counter to past understanding based on coarser temporal and spatial resolution data (e.g., Nicosia and Grumm 1999; Moore et al. 2005; see also Fig. 1.5).

Piecewise PV inversion and the delayed dry experiment in the 25 Dec 2002 case showed that LHR was critical to the formation and maintenance of the band. Band formation failed to occur in the absence of LHR in the dry simulation, and was substantially weaker even given a favorable upper PV distribution and lower PV anomaly present just 90 min prior in the delayed dry simulation. These results illustrate the role the band itself plays in its own evolution, via the positive feedback between LHR and frontogenesis (Emanuel 1985, Thorpe and Emanuel 1985; Davies 1999), and frontogenesis and stability (Nicosia and Grumm 1999). In particular, the presence of a band (and associated LHR) locally decreases heights leading to convergence, and locally increases the temperature gradient (e.g., Figs. 3.11 and 3.12). The induced convergent flow in the presence of the temperature gradient contributes to frontogenesis.

Furthermore, differential latent heating associated with the precipitation band can contribute to reduced stability above the level of maximum heating (Tables 3.1–3.3). However, the resulting strong ascent generally leads to a differential vertical advection pattern that stabilizes the environment, serving as a local "brake" on the feedback.

Although the band itself locally modifies the environment via diabatic feedbacks, the band was susceptible to changes in the meso-α scale flow associated with the formation and subsequent influence of new diabatic PV anomalies. Given that both band formation and dissipation in each case were largely driven by the upscale growth of diabatic PV anomalies, the observed details of which are uncertain (e.g., Zhang et al. 2003; Zhang et al. 2007), the predictability of banding events may be greatly limited. Indeed, Evans and Jurewicz (2009) have shown that the correlation between forecasts of band ingredients (frontogenesis, small EPV, and saturation) and observed event total snowfall decrease substantially beyond 12 h in an operational model. They attribute this result to timing and location errors. On the other hand, successful detailed operational short-range predictions of intense bands have been made (e.g., Novak et al. 2006). In the present study the dry run still exhibited frontogenesis (although limited) in the banding region, suggesting a degree of determinism in the potential for band formation, at least for forecast projections < 24 h. Thus, it is possible that band occurrence is more predictable than band timing and location. Future investigation of the predictability of band events, including aspects of their occurrence, location, and timing, is discussed in chapter 5.

Tables

Table 3.1 25 Dec 2002 potential temperature budget terms (x10^{-4} K s^{-1}) averaged over the specified time period, including differential horizontal advection (hor adv), vertical advection (vert adv), latent heating (latent), other (see text), and their sum. Positive (negative) values represent a stabilizing (destabilizing) tendency in the layer.

	Hor Adv	**Vert Adv**	**Latent**	**Other**	**SUM**
12–14 UTC	-3.1	1.7	0.3	-1.5	-2.6
14–19 UTC	-0.6	3.1	-1.2	-0.7	0.6
19–20 UTC	2.5	-0.9	-0.6	0.3	1.3

Table 3.2 12 Feb 2006 potential temperature budget terms (x10^{-4} K s^{-1}) averaged over the specified time period, including differential horizontal advection (hor adv), vertical advection (vert adv), latent heating (latent), other (see text), and their sum. Positive (negative) values represent a stabilizing (destabilizing) tendency in the layer.

	Hor Adv	**Vert Adv**	**Latent**	**Other**	**SUM**
0–7 UTC	-7.5	4.6	1.1	0.1	-1.7
7–14 UTC	-0.9	0.1	0.9	-0.1	0
14–18 UTC	-1.8	9.9	-4.6	-0.8	2.7

Table 3.3 14 Feb 2007 potential temperature budget terms (x10^{-4} K s^{-1}) averaged over the specified time period, including differential horizontal advection (hor adv), vertical advection (vert adv), latent heating (latent), other (see text), and their sum. Positive (negative) values represent a stabilizing (destabilizing) tendency in the layer.

	Hor Adv	**Vert Adv**	**Latent**	**Other**	**SUM**
10–12 UTC	-1.8	0.7	-0.7	~0	-1.8
12–18 UTC	-0.5	4.8	-4.7	0.8	0.4
18–20 UTC	3.1	9.8	-5.4	-1.2	6.3

Figures

Figure 3.1 12-km MM5 piecewise PV inversion domain with geographic locations labeled as New England (NE), New York (NY), Pennsylvania (PA), New Jersey (NJ), Virginia (VA), North Carolina (NC), and Ohio (OH).

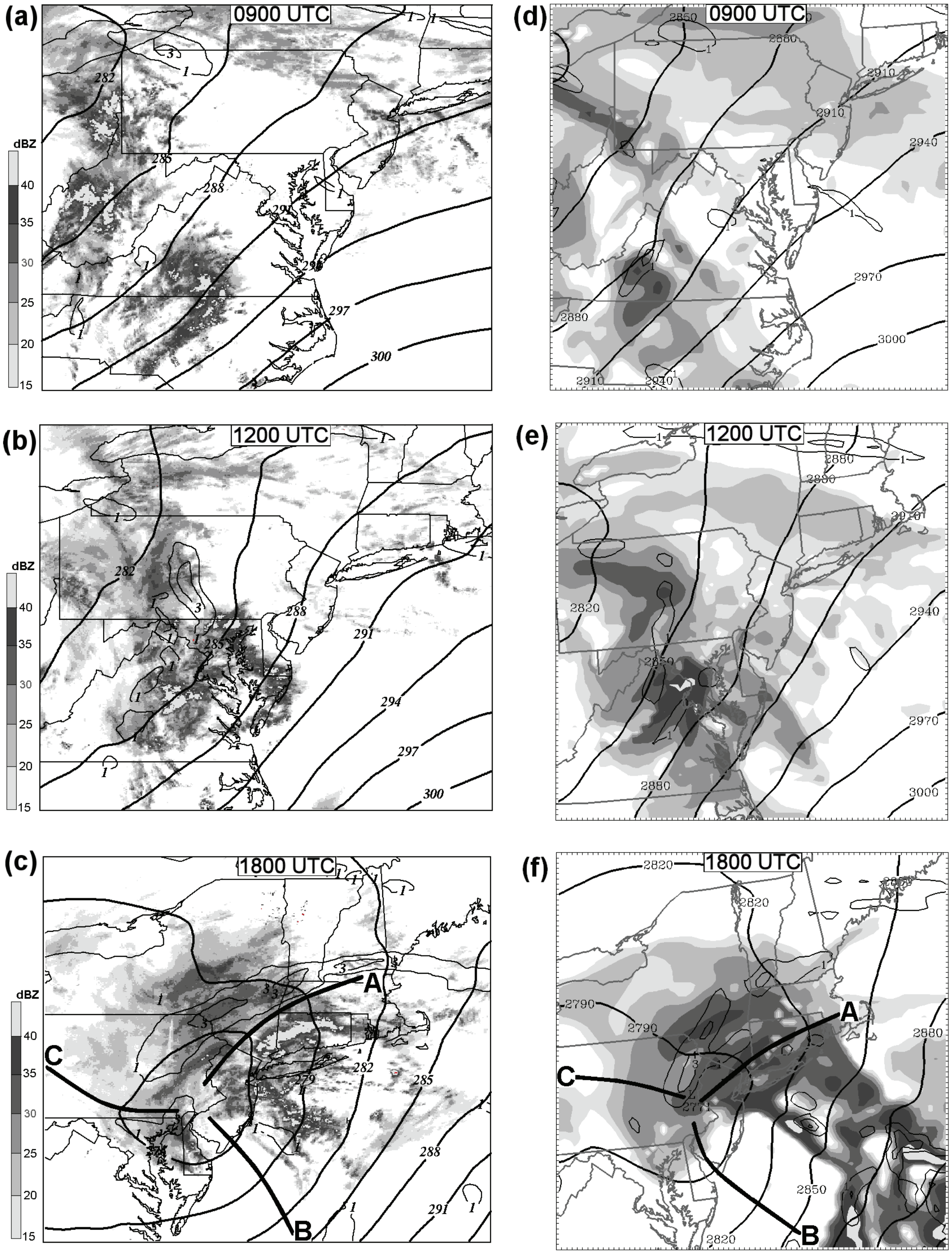

Figure 3.2 WSR-88D radar mosaic (reflectivity shaded according to scale starting at 15 dBZ), with the 12-km Eta analysis 700-hPa geopotential height (thick solid, contoured every 30 m), and 700-hPa Petterssen frontogenesis [thin solid, positive values contoured every 2°C $(100\ \mathrm{km})^{-1}$ $(\mathrm{h})^{-1}$ starting at 1°C $(100\ \mathrm{km})^{-1}$ $(\mathrm{h})^{-1}$] overlaid, valid at (a) 0900 UTC, (b) 1200 UTC, and (c) 1800 UTC 25 Dec 2002. (d) 12-km MM5 9-h forecast surface simulated reflectivity, 700-hPa geopotential height (thick solid, contoured every 30 m), and 700-hPa Petterssen frontogenesis [thin solid, positive values contoured every 2ºC $(100\ \mathrm{km})^{-1}$ $(\mathrm{h})^{-1}$ starting at 1ºC $(100\ \mathrm{km})^{-1}$ $(\mathrm{h})^{-1}$] valid at 0900 UTC, (e) 1200 UTC, and (f) 1800 UTC 25 Dec 2002.

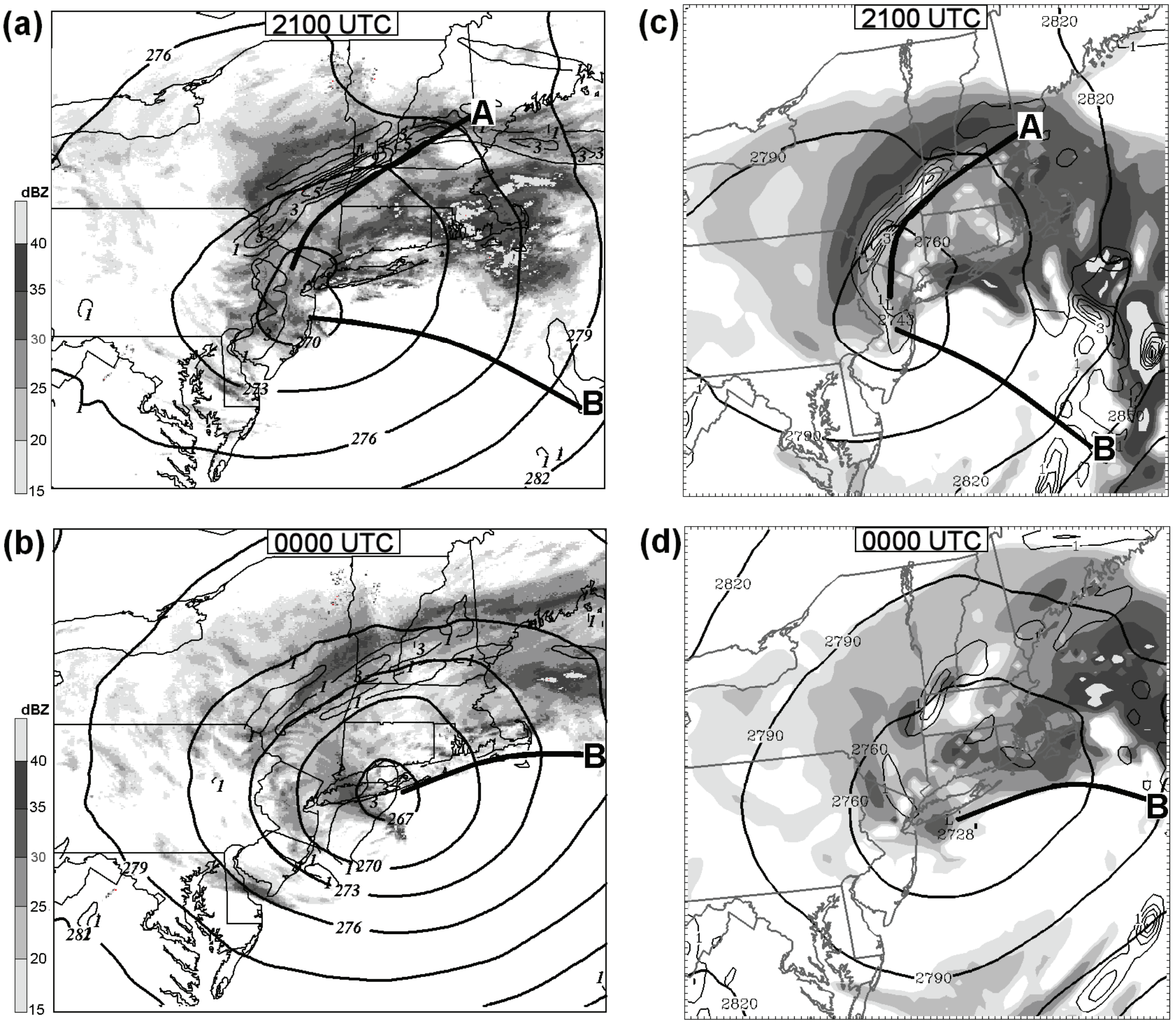

Figure 3.3 As in Fig. 3.2, except WSR-88D radar mosaic valid at (a) 2100 UTC 25 Dec 2002 and (b) 0000 UTC 26 Dec 2002, and MM5 forecast valid at (c) 2100 UTC 25 Dec 2002, and (d) 0000 UTC 26 Dec 2002.

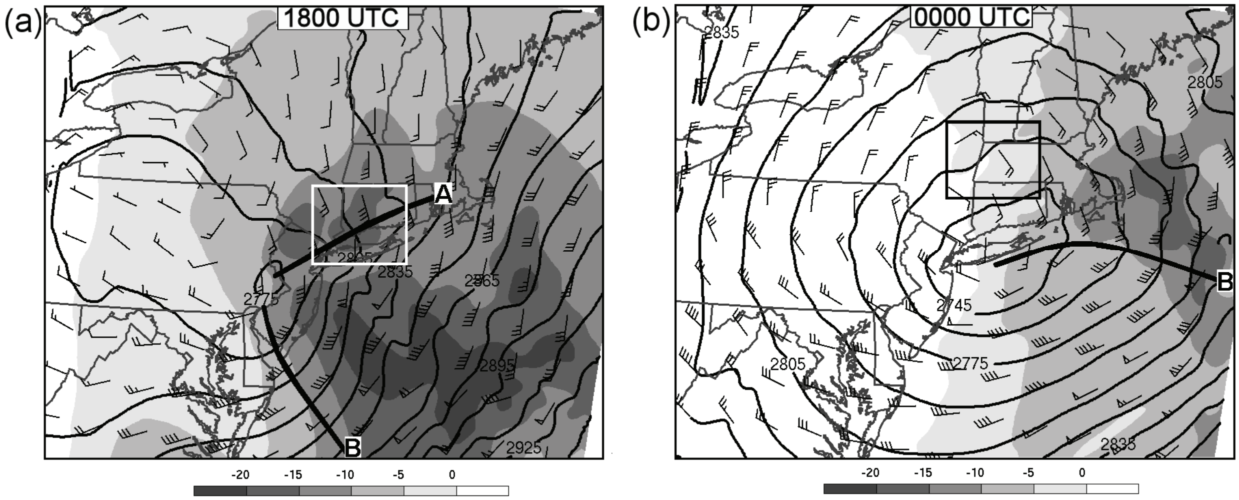

Figure 3.4 MM5 forecast 700-hPa geopotential height (thick solid, contoured every 15 m), wind (1 full barb = 10 kt), and height falls [shading according to scale (m h^{-1})] valid at (a) 1800 UTC and (b) 0000 UTC. Deformation values cited in the text were calculated within box shown on each panel.

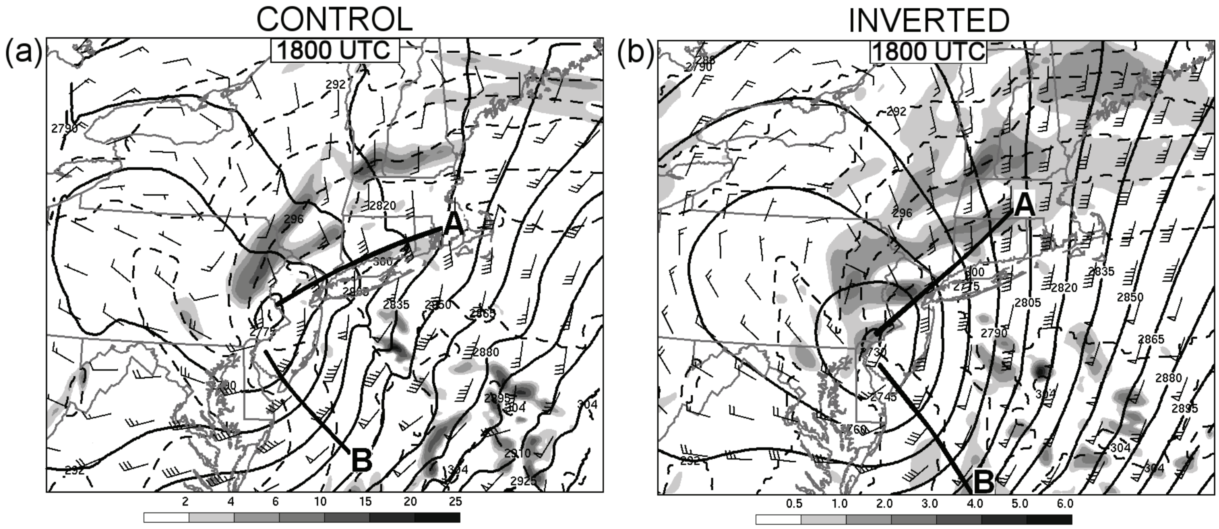

Figure 3.5 Comparison of the (a) control and (b) inverted 700-hPa geopotential height (contoured every 15 m), wind (1 full barb = 10 kt), and resulting frontogenesis [shaded according to scale, in units of °C (100 km)$^{-1}$ (3 h)$^{-1}$], valid 1800 UTC 25 Dec 2002. The control run 700-hPa potential temperature (dashed) is contoured every 2 K in (a) and (b).

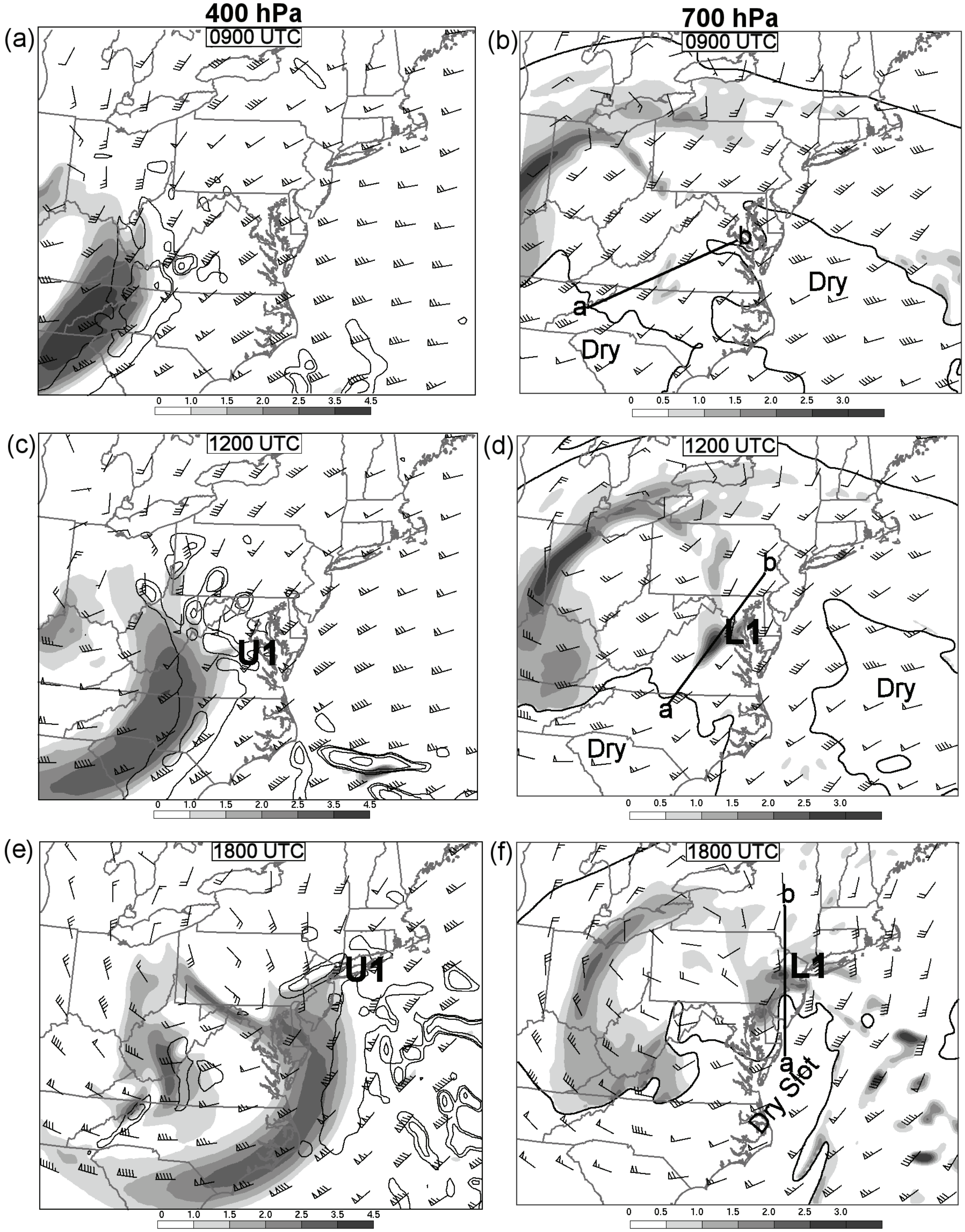

Figure 3.6 (a) 0900 UTC 25 Dec 2002 400-hPa PV perturbation (shaded according to scale every 0.5 PVU where 1 PVU = 10^{-6} K m^2 kg^{-1} s^{-1}), winds (1 barb = 10 kt), and PV advection (thin, contoured where positive every 0.5 x 10^{-5} PVU s^{-1} starting at 0.5 x 10^{-5} PVU s^{-1}). (b) As in (a), except at 700 hPa and with the 70% isohume overlaid (thick solid). (c,d) As in (a,b), except at 1200 UTC 25 Dec 2002. (e,f) As in (a,b), except at 1800 UTC 25 Dec 2002.

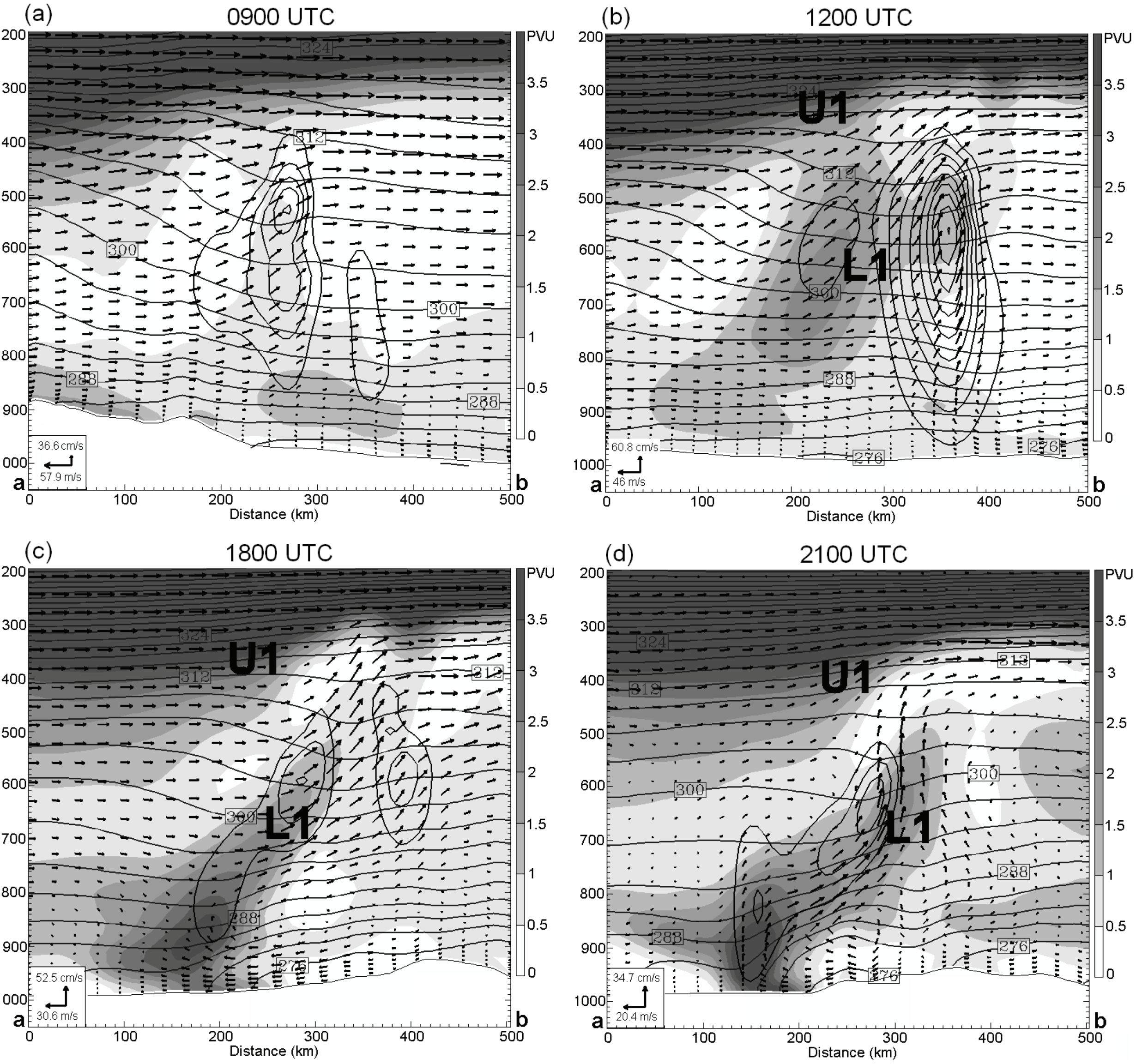

Figure 3.7 (a) 12-km MM5 9-h forecast cross section (orientation shown in Fig. 3.6b) of PV (shaded according to scale, starting at 0.5 PVU), potential temperature (gray solid, contoured every 3 K), instantaneous latent heating rate (black solid, contoured every 1°C h^{-1}, starting at 0°C h^{-1}), and velocity in the plane of the cross section (arrows). (b) As in (a), except for the 12 h forecast (orientation shown in Fig. 3.6d). (c) As in (a), except for the 18 h forecast (orientation shown in Fig. 3.6f). (d) As in (a), except for the 21 h forecast (orientation shown in Fig. 3.10a).

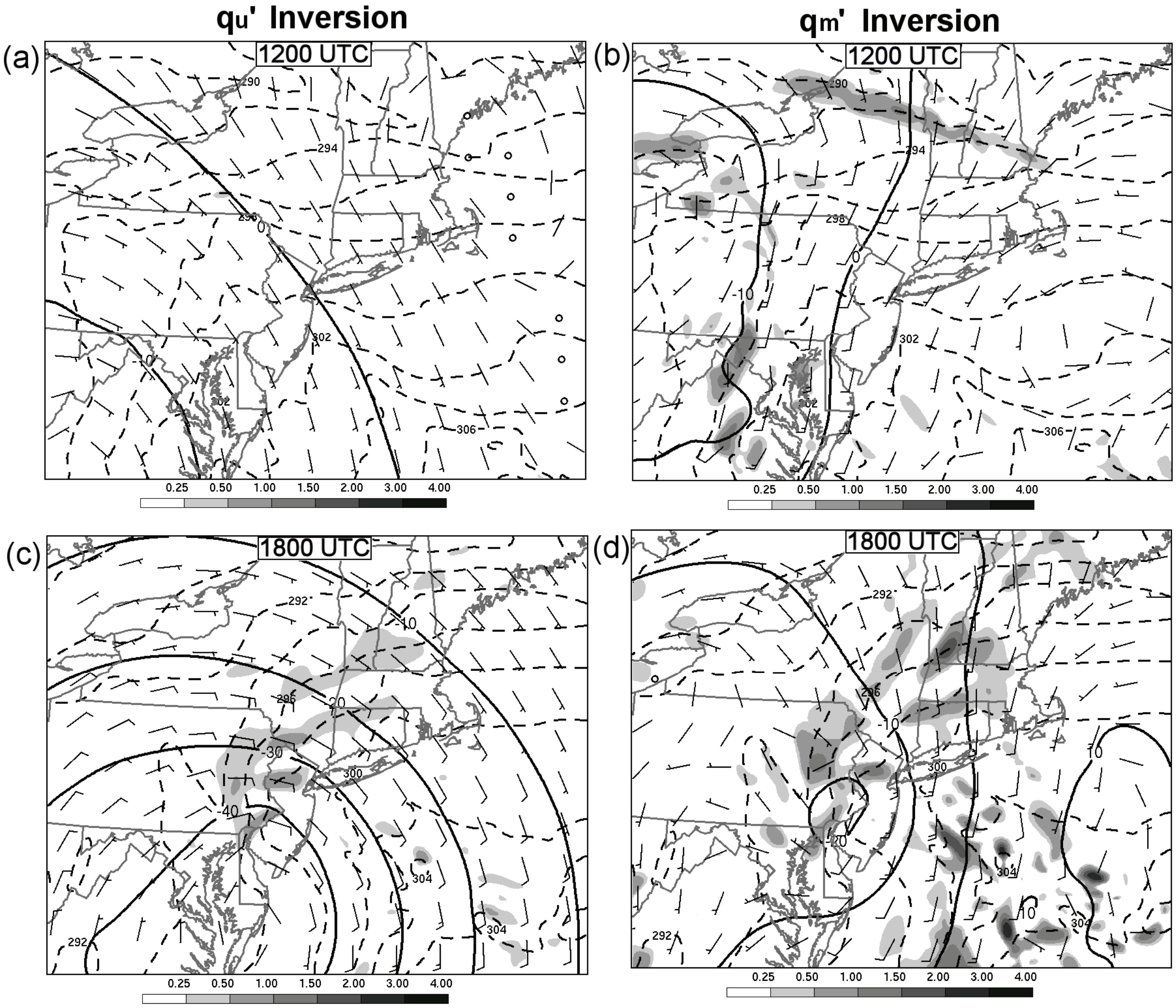

Figure 3.8 (a) The 700-hPa balanced geopotential height (contoured every 10 m) and wind (1 full barb = 10 kt) inverted from q_u', and resulting frontogenesis [shaded according to scale starting at 0.25°C (100 km)$^{-1}$ (3 h)$^{-1}$]. The control run 700-hPa potential temperature (dashed) is contoured every 2 K. (b) As in (a), except inverted from q_m'. (c) As in (a), except valid at 1800 UTC 25 Dec 2002. (d) As in (b), except valid at 1800 UTC 25 Dec 2002.

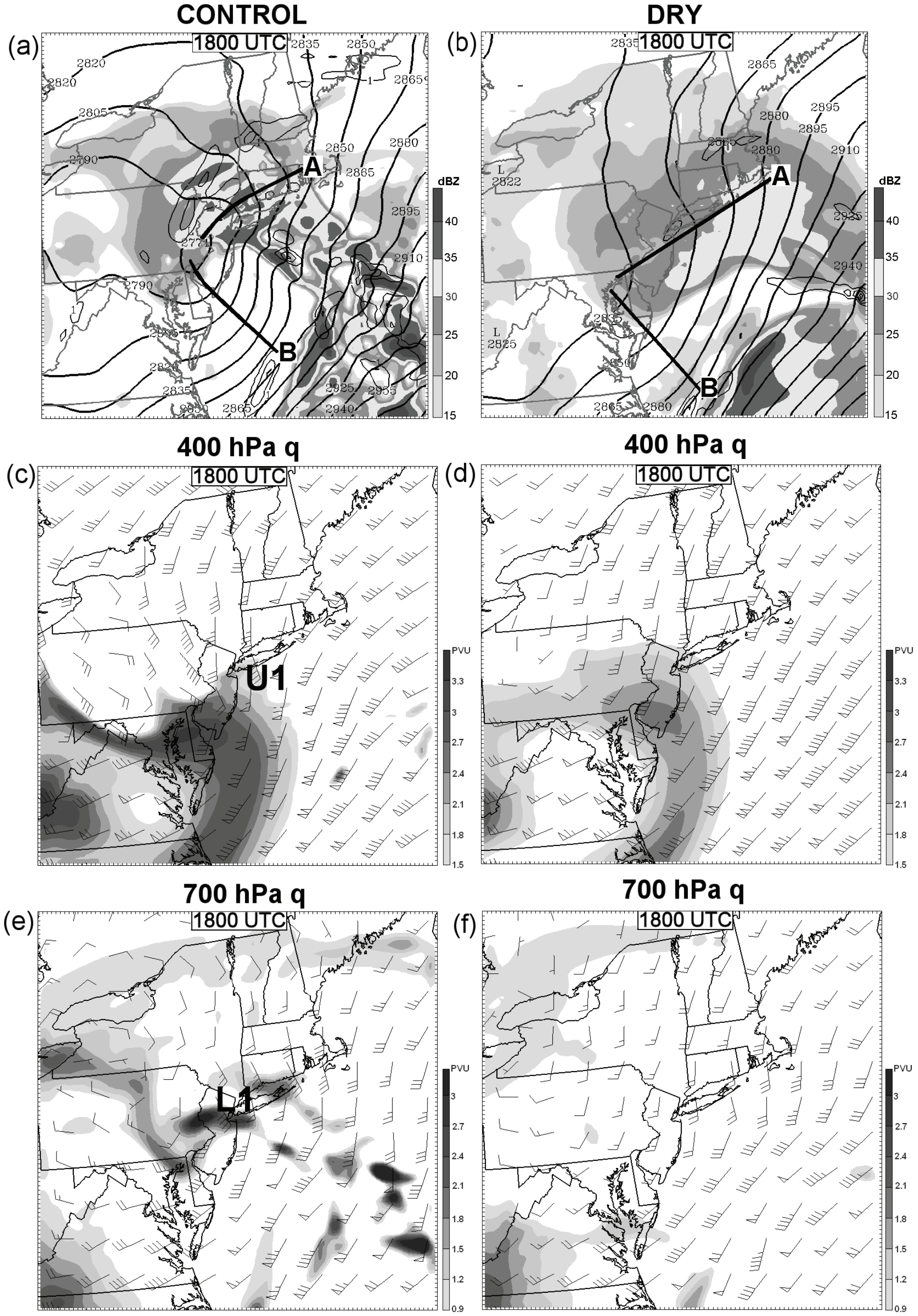

Figure 3.9 Comparison of the control (left column) and dry runs (right column) valid at 1800 UTC 25 Dec 2002. (a,b) geopotential height (solid, contoured every 15 m), frontogenesis [contoured where positive every 2°C (100 km)$^{-1}$ h^{-1},starting at 1°C (100 km)$^{-1}$ h^{-1}], and simulated reflectivity (shaded according to scale). (c,d) 400-hPa PV (PVU; shaded according to scale) and winds (1 barb = 10 kt). (e,f) As in (c,d), except for 700 hPa.

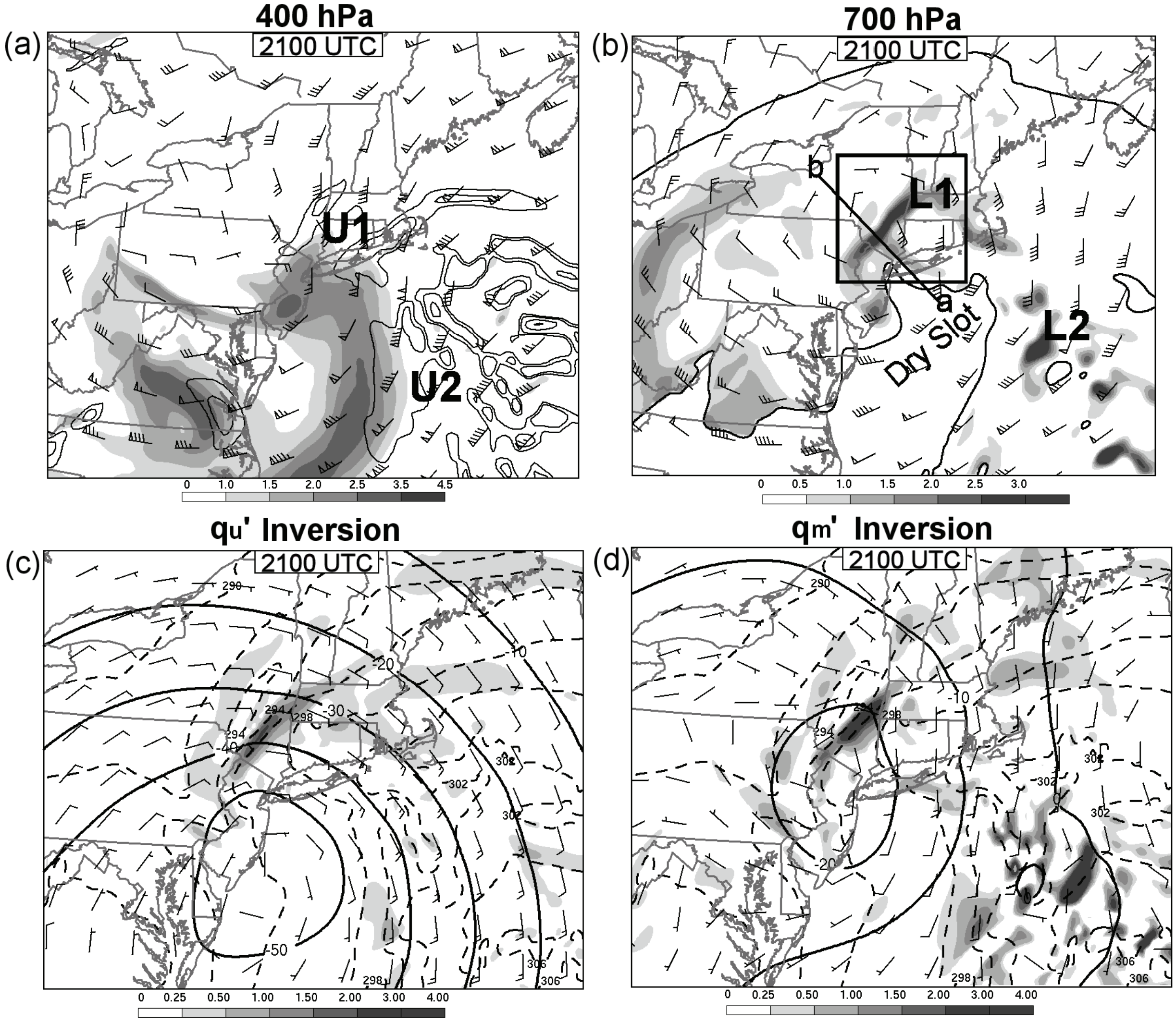

Figure 3.10 (a,b) As in Fig. 3.6, except valid at 2100 UTC 25 Dec 2002. The region used for the inversion shown in Fig. 3.11 is outlined in (b). (c,d) As in Fig. 3.8, except valid 2100 UTC 25 Dec 2002.

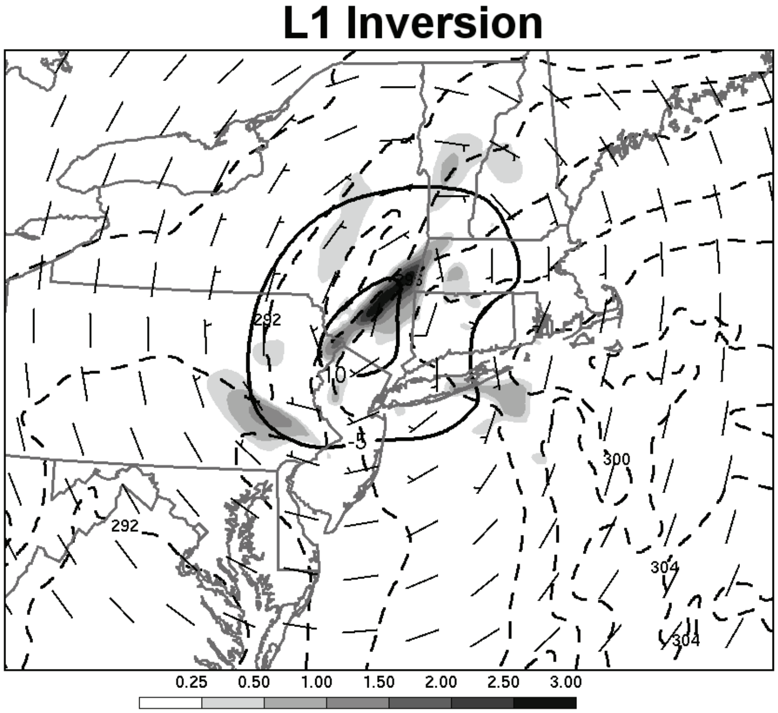

Figure 3.11 The 700-hPa balanced geopotential height (contoured every 5 m), and wind (1 full barb = 10 kt) inverted from q_m' within the box in Fig. 3.10b at 2100 UTC 25 Dec 2002. The control run 700-hPa temperature (dashed) is contoured every 2 K. The resulting frontogenesis is shaded according to scale, starting at 0.25°C $(100\ \mathrm{km})^{-1}$ $(3\ \mathrm{h})^{-1}$.

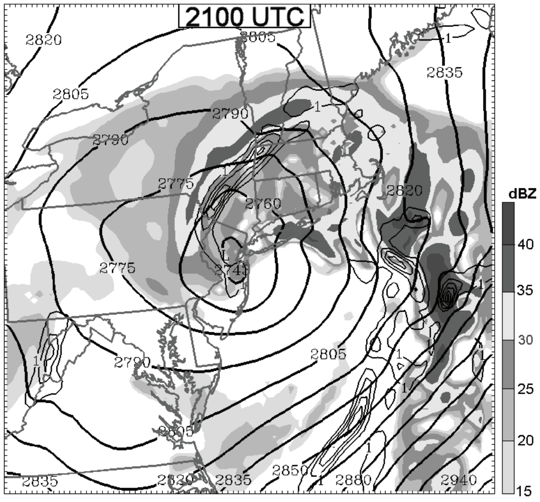
(a) CONTROL

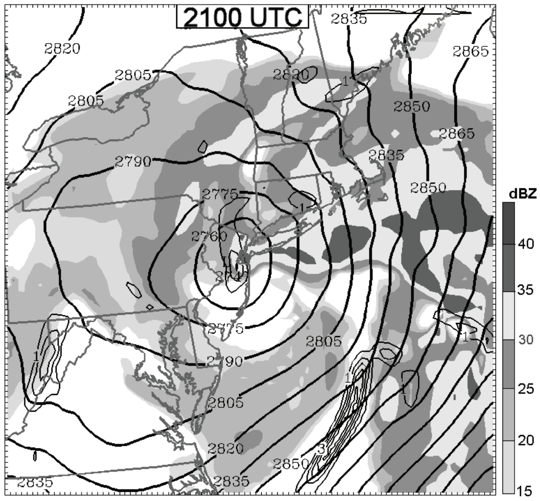
(b) DELAYED DRY

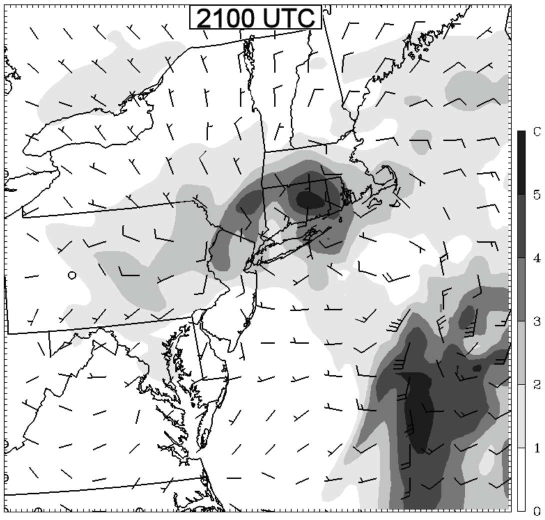
(c) DIFFERENCE

Figure 3.12 Comparison of the (a) control and (b) delayed-dry run geopotential height (solid, contoured every 15 m), frontogenesis [contoured where positive every 2°C $(100\ \mathrm{km})^{-1}\ (3\ \mathrm{h})^{-1}$, starting at 1° C $(100\ \mathrm{km})^{-1}\ \mathrm{h}^{-1}$] and simulated reflectivity (shaded according to scale), valid at 2100 UTC 25 Dec 2002. (c) Temperature (shaded) and wind (barbs) difference (control minus delayed-dry run), valid 2100 UTC 25 Dec 2002.

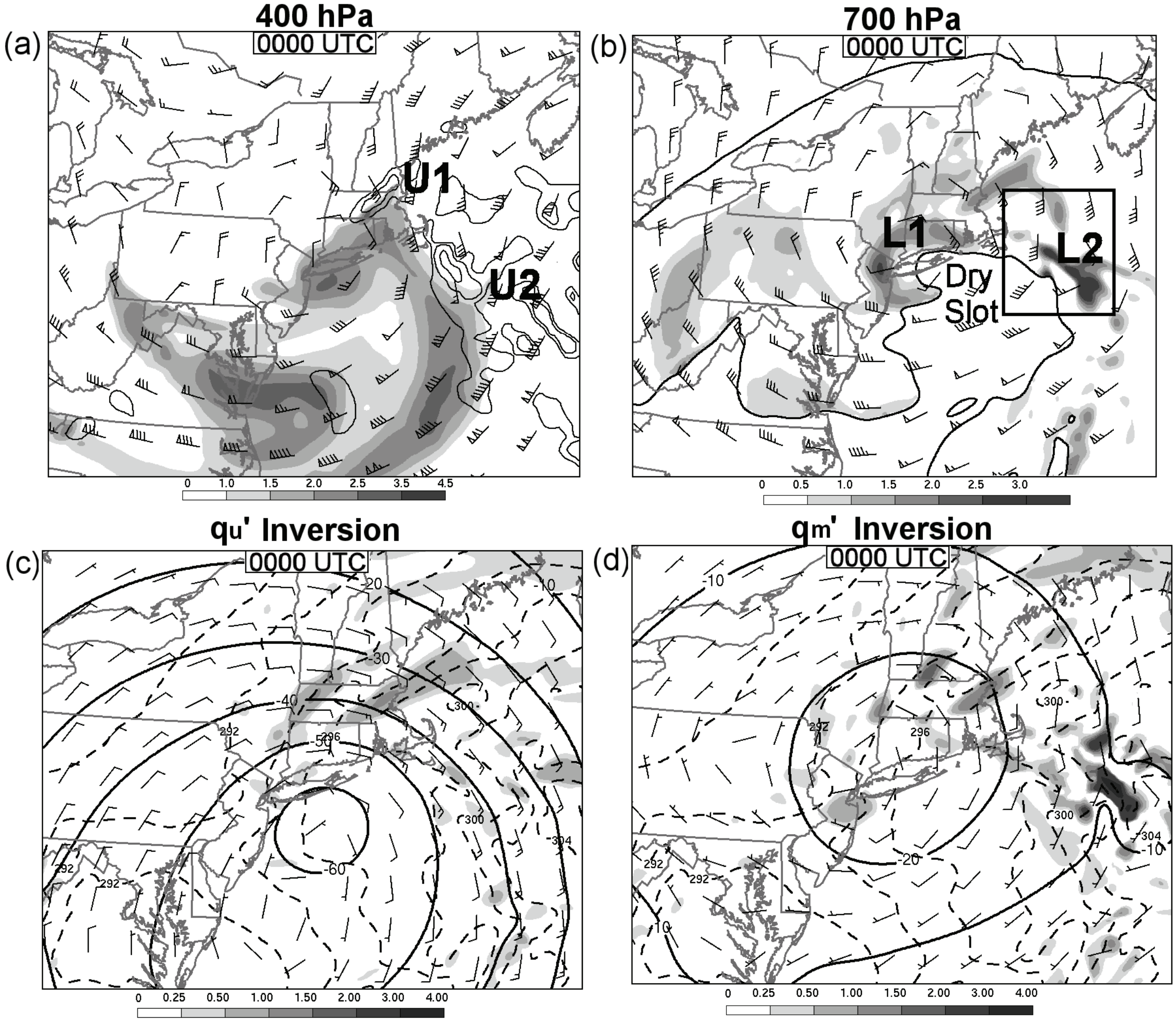

Figure 3.13 As in Fig. 3.10, except valid at 0000 UTC 25 Dec 2002. The region used for the inversion shown in Fig. 3.14 is outlined in (b).

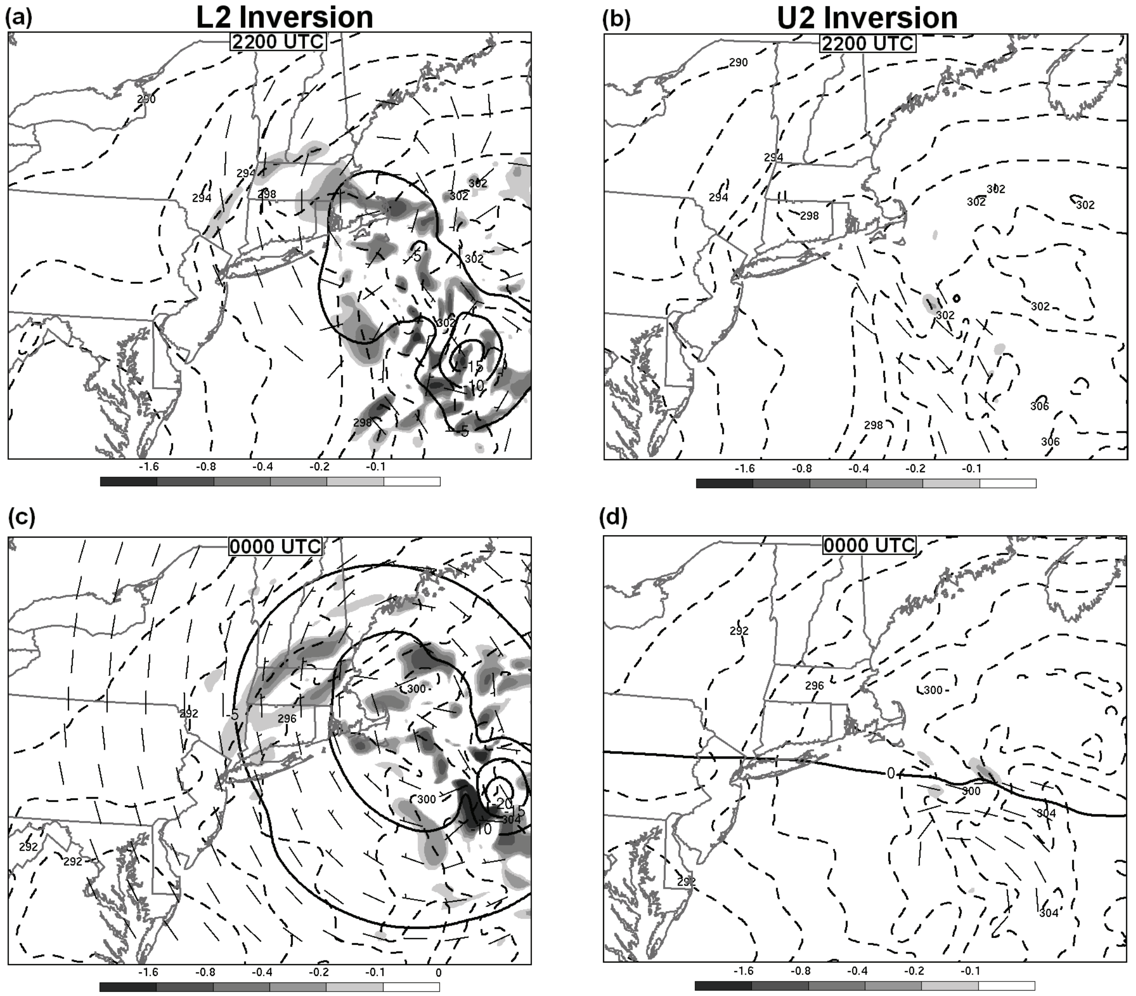

Figure 3.14 The 700-hPa balanced geopotential height (contoured ever 5 m) and wind (1 full barb = 10 kt) inverted from (a,c) L2 (see Fig. 3.13b), and (b,d) U2 at (a,b) 2200 UTC 25 Dec 2002 and (c,d) 0000 UTC 26 Dec 2002. The control run 700-hPa temperature (dashed) is contoured every 2 K. The resulting negative frontogenesis (frontolysis) is shaded according to the scale, starting at -0.1°C (100 km)$^{-1}$ (3 h)$^{-1}$.

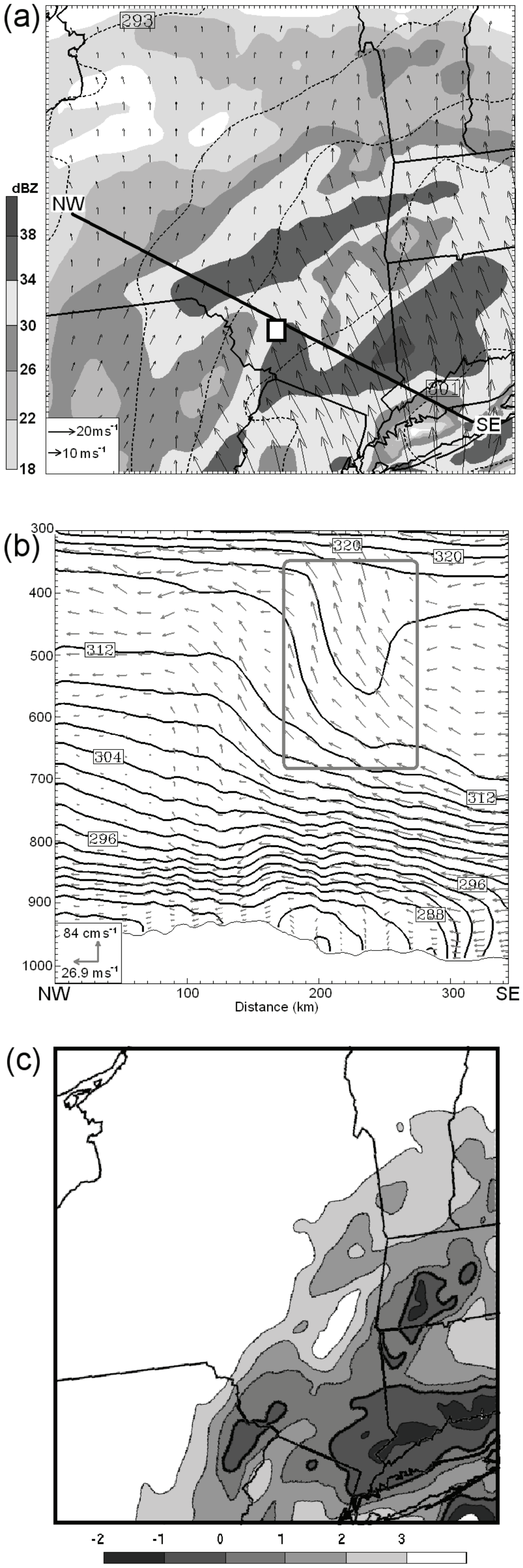

Figure 3.15. (a) 4-km MM5 18-h forecast simulated reflectivity (1-km MSL altitude; shaded according to scale), 3-km MSL wind (arrows), and potential temperature (dashed, contoured every 2 K). Analysis location for the stability budget marked by a white box. (b) 4-km MM5 18-h forecast cross section [orientation shown in (a)] of saturation equivalent potential temperature (black solid, contoured every 2 K), and velocity in the plane of the cross section (arrows). Box outlines general region of weak conditional stability. (c) 4-km MM5 18-h forecast saturation equivalent potential temperature difference [470 hPa minus 600 hPa)]. Negative values indicate conditional instability in the layer (zero contour thick).

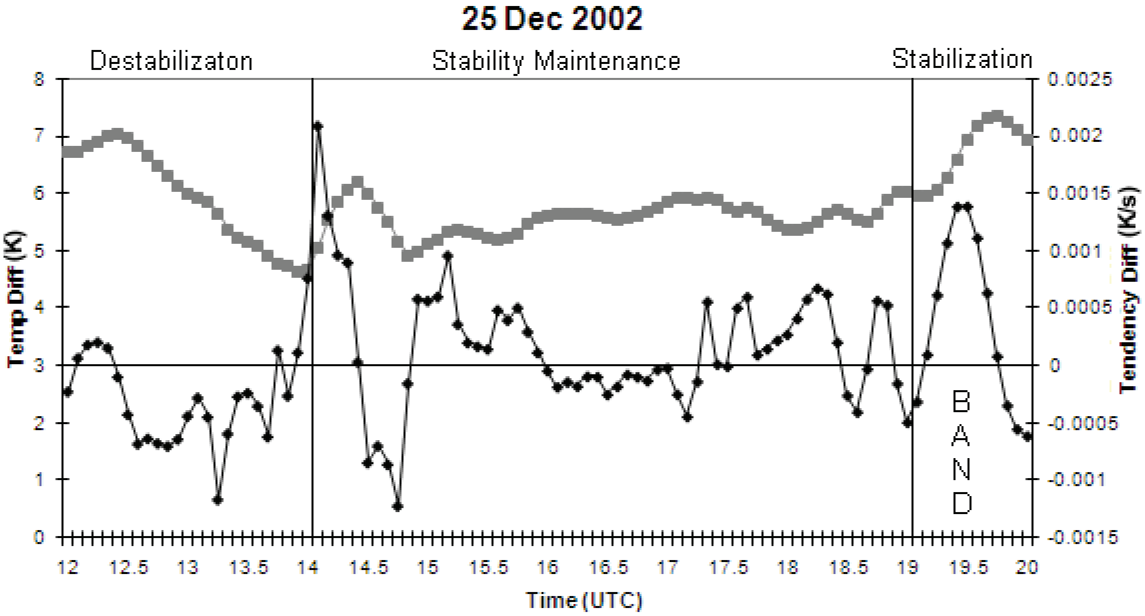

Figure 3.16 Time series of the potential temperature tendency (black) and potential temperature difference [470 hPa minus 600 hPa] (gray) for the stability budget analysis location shown in Fig. 15a during the 1200–2000 UTC 25 Dec 2002 time period. Key periods of destabilization, stability maintenance, stabilization, and band formation (BAND) are labeled.

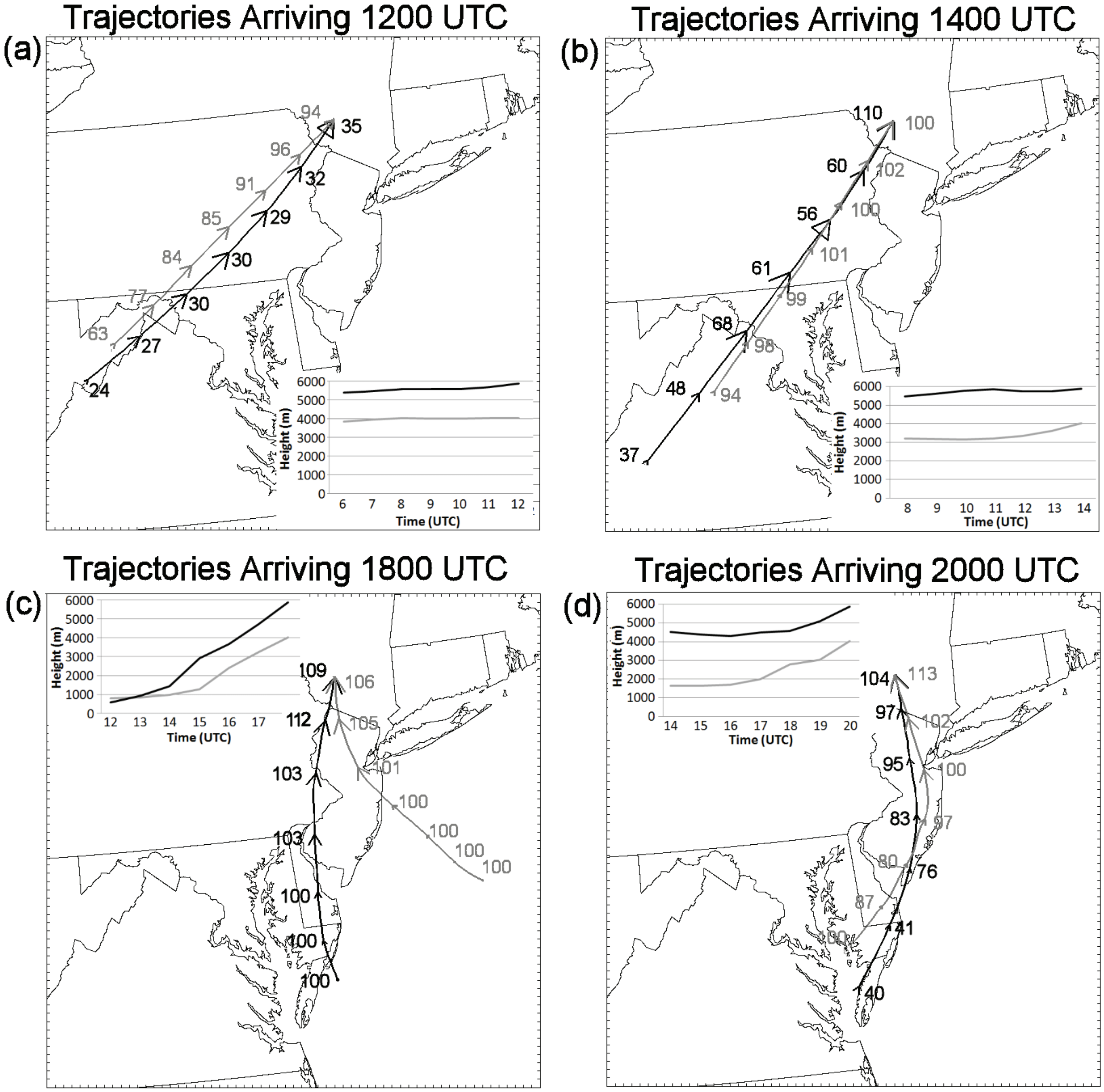

Figure 3.17 6-h back trajectories of parcels arriving at the stability budget box at (a) 1200 UTC, (b) 1400 UTC, (c) 1800 UTC, and (d) 2000 UTC 25 Dec 2002. The parcel arriving at the top (bottom) of the conditionally unstable layer is black (gray). RH w.r.t. ice is annotated for each trajectory every hour.

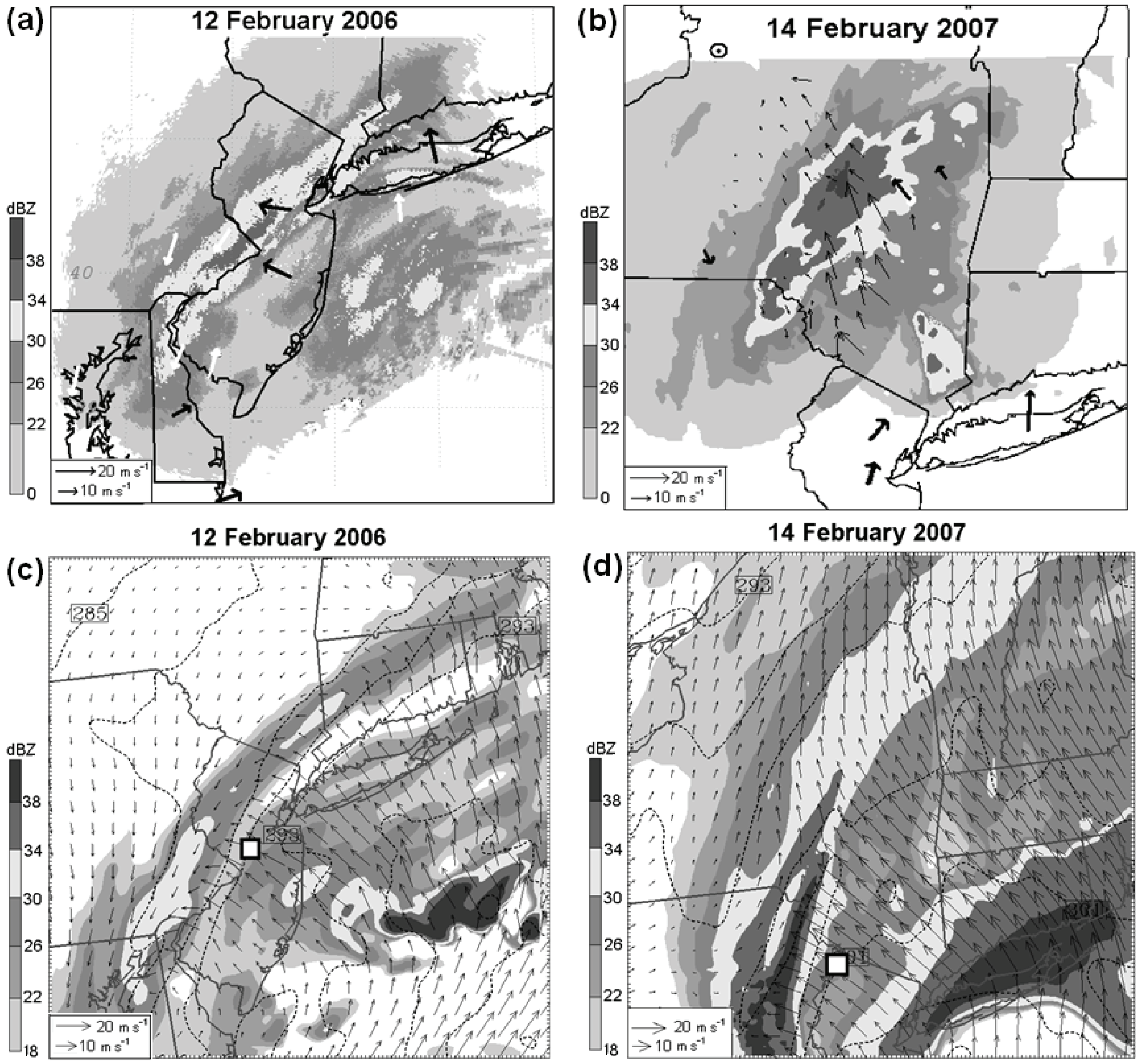

Figure 3.18 (a) Observed reflectivity (1-km MSL altitude; shaded according to scale) and 3-km MSL winds (arrows) valid at 1201 UTC 12 Feb 2006. In situ and remote sensing wind observations displayed as thick black arrows. Single-Doppler derived wind direction vectors displayed as white arrows. (b) As in (a), except valid for 1801 UTC 14 Feb 2007. Dual-Doppler winds displayed as this black arrows. (c,d) Corresponding 4-km MM5 simulated reflectivity (1-km MSL altitude; shaded according to scale), 3-km MSL wind (arrows), and potential temperature (dashed, contoured every 2 K). The stability analysis location for each case is marked by the white box.

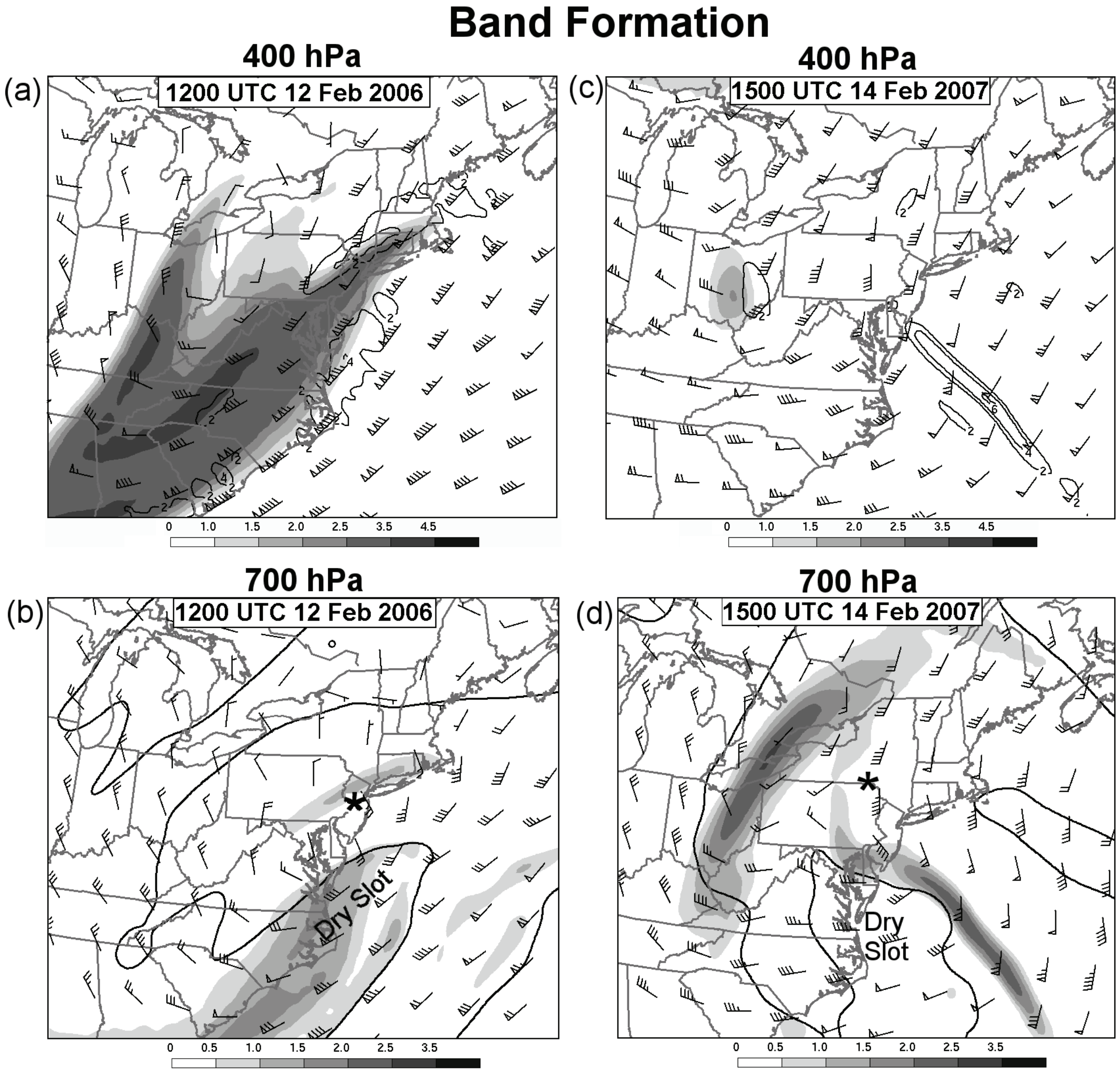

Figure 3.19 (a) 1200 UTC 12 Feb 2006 400-hPa PV perturbation (shaded according to scale every 0.5 PVU where 1 PVU = 10^{-6} K m^2 kg^{-1} s^{-1}), winds (1 barb = 10 kt), and PV advection (thin, contoured where positive every 2 x 10^{-5} PVU s^{-1} starting at 2 x 10^{-5} PVU s^{-1}). (b) As in (a), except for 700 hPa. The 70% isohume is overlaid. (c) As in (a), except for 1500 UTC 14 Feb 2007. (d) As in (c) except at 1500 UTC 14 Feb 2007. Band formation centroid position shown as a "*" in (b) and (d).

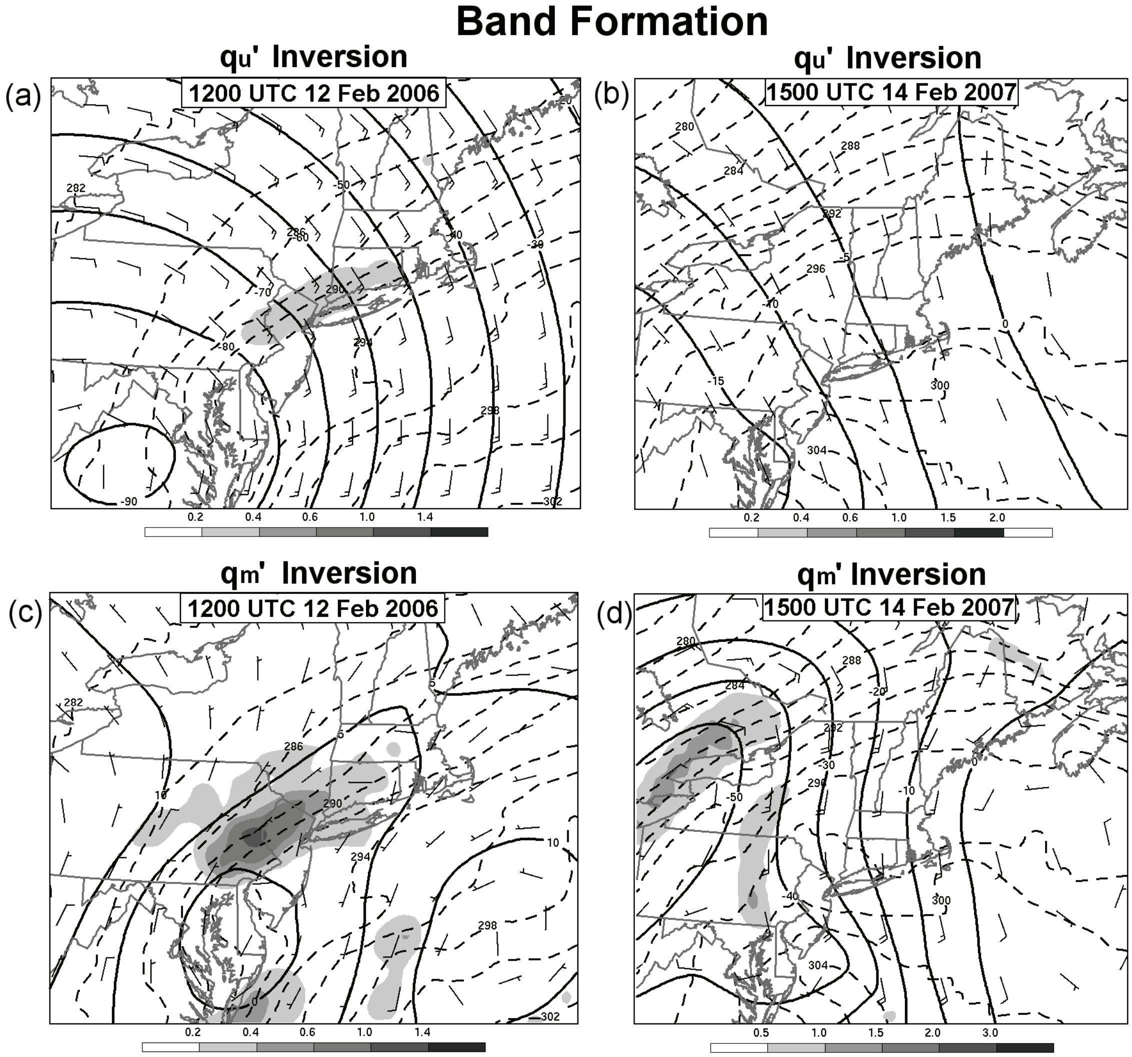

Figure 3.20 The 700-hPa balanced geopotential height (contoured every 10 m) and wind (1 full barb = 10 kt) inverted from q_u', and resulting frontogenesis [shaded according to scale in °C (100 km)$^{-1}$ (3 h)$^{-1}$] for (a) 1200 UTC 12 Feb 2006 and (b) 1500 UTC 14 Feb 2007. The control run 700-hPa potential temperature (dashed) is contoured every 2 K. (c,d) As in (a,b) except inverted from q_m'.

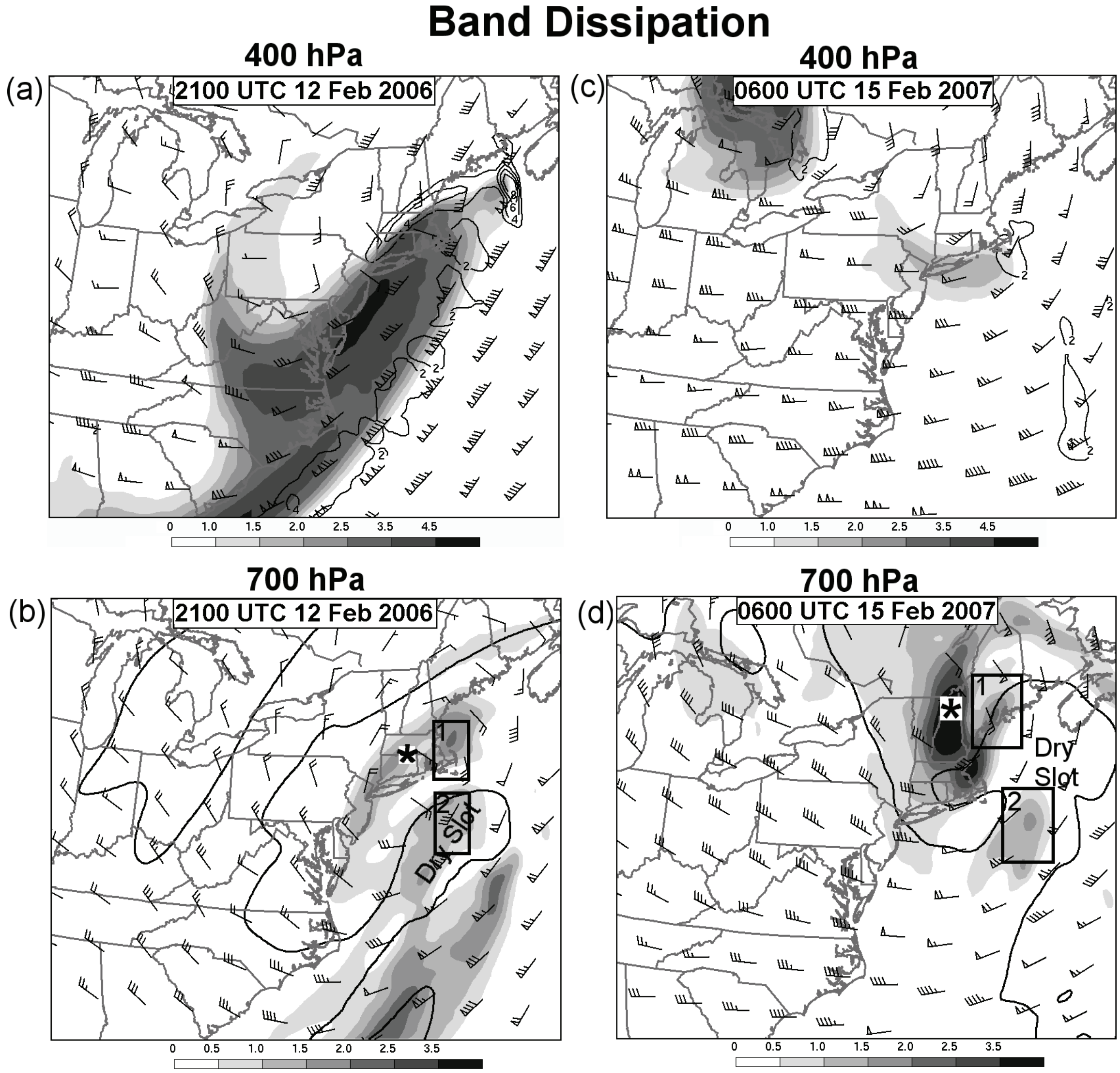

Figure 3.21 (a) 2100 UTC 12 Feb 2006 400-hPa PV perturbation (shaded according to scale every 0.5 PVU where 1 PVU = 10^{-6} K m^2 kg^{-1} s^{-1}), winds (1 barb = 10 kt), and PV advection (thin, contoured where positive every 2 x 10^{-5} PVU s^{-1} starting at 2 x 10^{-5} PVU s^{-1}). (b) As in (a), except for 700 hPa. The 70% isohume is overlaid. (c) As in (a), except for 0600 UTC 15 Feb 2007. (d) As in (c) except for 0600 UTC 14 Feb 2007. Band centroid position shown as a "*" , and respective inversion boxes for Fig. 3.23 shown in (b) and (d).

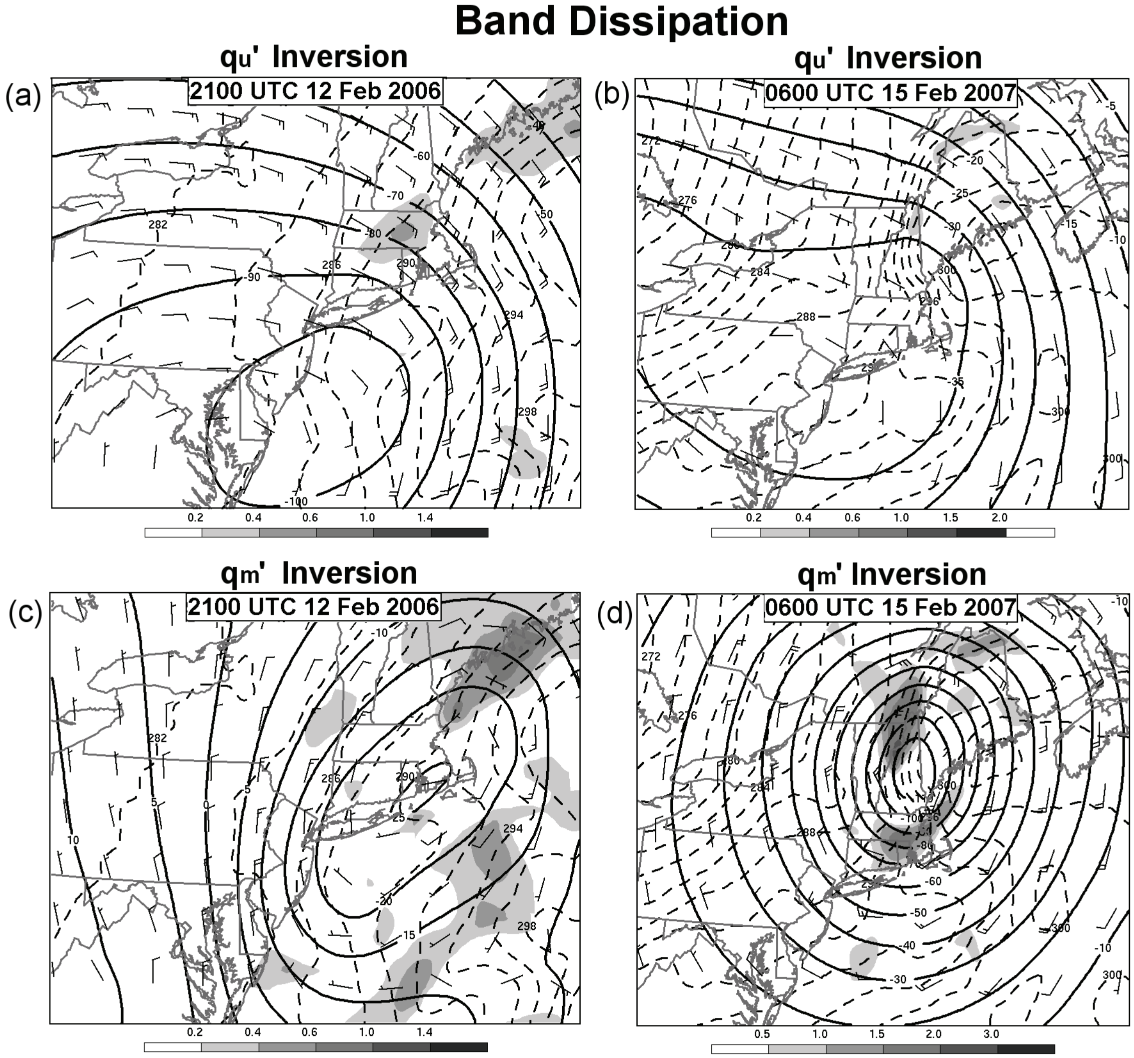

Figure 3.22 The 700-hPa balanced geopotential height (contoured every 10 m) and wind (1 full barb = 10 kt) inverted from q_u', and resulting frontogenesis [shaded according to scale in °C $(100\ \text{km})^{-1}$ $(3\ \text{h})^{-1}$] for (a) 2100 UTC 12 Feb 2006 and (b) 0600 UTC 15 Feb 2007. The control run 700-hPa potential temperature (dashed) is contoured every 2 K. (c,d) As in (a,b) except inverted from q_m'.

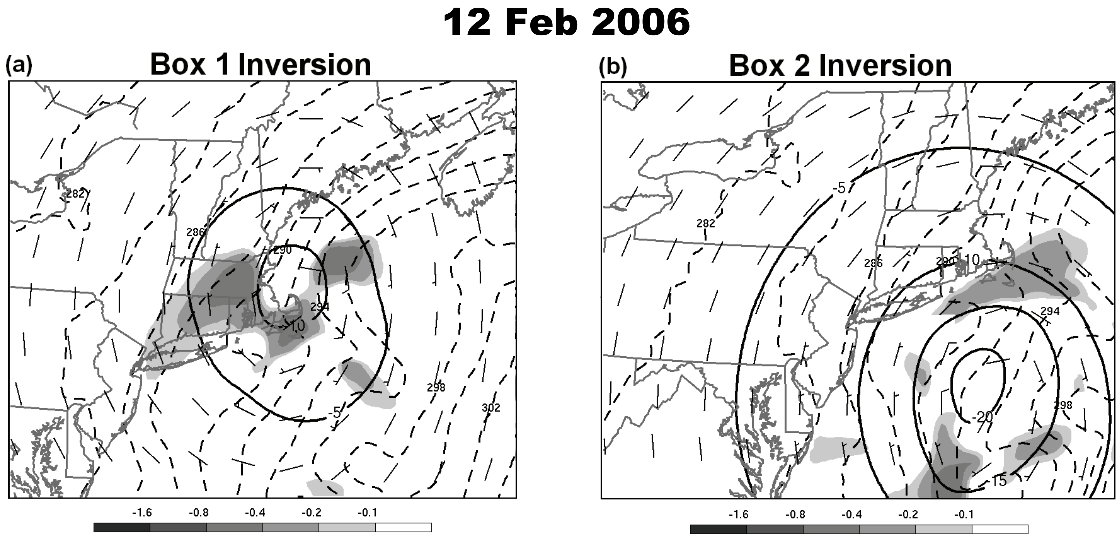

Figure 3.23 The 12 Feb 2006 700-hPa balanced geopotential height (contoured ever 5 m) and wind (1 full barb = 10 kt) inverted from (a) box 1 (see Fig. 3.21b), and (b) box 2. The control run 700-hPa temperature (dashed) is contoured every 2 K. The resulting negative frontogenesis (frontolysis) is shaded according to the scale, starting at -0.1°C (100 km)$^{-1}$ (3 h)$^{-1}$.

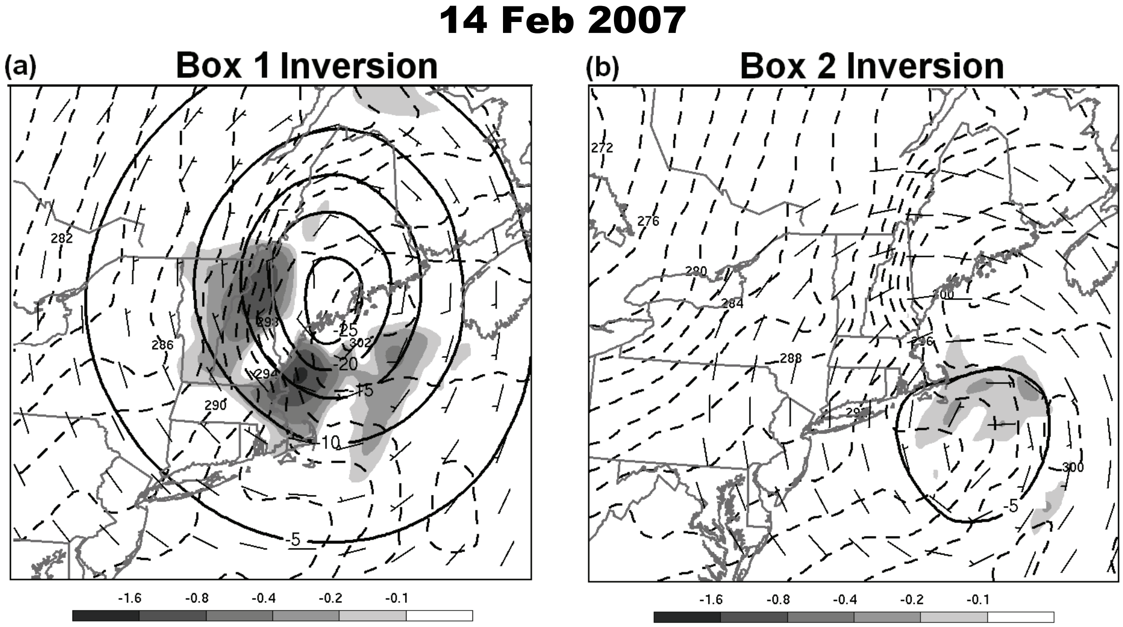

Figure 3.24 The 14 Feb 2007 700-hPa balanced geopotential height (contoured ever 5 m) and wind (1 full barb = 10 kt) inverted from (a) box 1 (see Fig. 3.21d), and (b) box 2. The control run 700-hPa temperature (dashed) is contoured every 2 K. The resulting negative frontogenesis (frontolysis) is shaded according to the scale, starting at -0.1°C (100 km)$^{-1}$ (3 h)$^{-1}$.

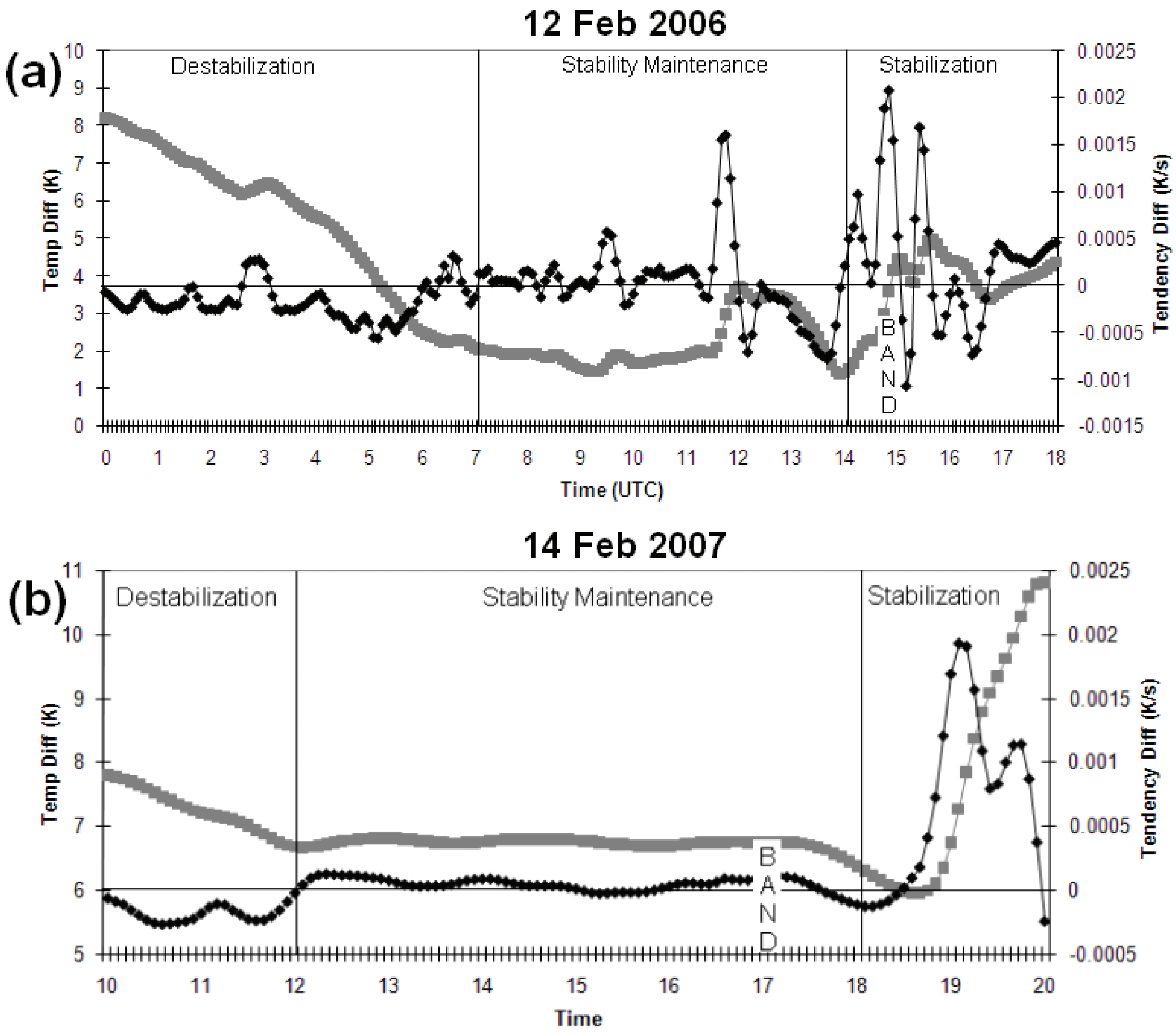

Figure 3.25 As in Fig. 3.16, except for (a) 0–18 UTC 12 February 2006 and (b) 10–20 UTC 14 February 2007.

Chapter IV:

Climatological and Composite Analysis of Mesoscale Band Evolution

4.1. Introduction

The observational and modeling case study results presented in chapters 2 and 3 highlighted a particular band life cycle. Band formation was coincident with the sharpening of a midlevel trough and associated increase in frontogenesis in an environment of conditional instability. Band maturity was marked by increasing conditional stability and a compensating increase in frontogenetical forcing, while band dissipation occurred as the frontogenetical forcing weakened and the conditional stability continued to increase. These results were based on only three cases. Thus it is important to generalize these findings with a larger number of cases. It is also important to understand how the frontogenetical forcing and stability evolves for a set of non-banding (null) cases as a comparison.

In a previous climatological and composite study based on the 1996–2001 cool seasons, Novak et al. (2004) constructed composites for single-banded events in the comma-head sector of northeast U.S. cyclones (their northwest quadrant). A schematic representation of a banded cyclone at the time of band formation from this work (Fig. 1.5b) exhibits a closed midlevel circulation with frontogenesis concentrated in the comma-head sector. However, Novak et al. (2004) was limited to 80-km Eta model analyses at 6-h temporal resolution, and thus could not address the mesoscale aspects of the frontogenesis and stability evolution during band life cycle. Higher temporal and spatial resolution analyses from multiple cases may help establish common mesoscale flow evolutions associated with banding events, and relate these evolutions to larger scale cyclone features, such as the trowal and upper PV distribution. These analyses may also help quantify the frequency of instabilities during band evolution, as reviewed in section 1.1b.

In the small sample of three banded cyclone events presented in chapter 3, there were a variety of upper (400 hPa) PV evolutions that supported band development. Banded events viewed from a PV perspective have been rare; however, the 25 Dec 2002 and 12 Feb 2006 cases studied in chapters 2 and 3, as well as the case studied by Martin (1998a,b), exhibited a PV hook, while the 14 Feb 2007 case did not. A larger set of cases may help identify the variety of upper PV evolutions that support band formation, and determine whether the PV hook is a common type.

To clarify the relevant dynamics of band formation in the comma-head sector of cyclones it is also instructive to examine null cases. Novak et al. (2004) showed that cases in which a midlevel closed low fails to form do not have banding in the comma-head region given the limited deformation and frontogenesis in this sector of the cyclone. However, not all cases that form a closed midlevel low develop bands in the comma-head. As reviewed in section 1.1c, Greenstein (2006) found that single-banded events (his "classic" type) had stronger and deeper frontogenesis and weaker conditional stability than events exhibiting more uniform reflectivity shields. Whether this finding can be shown for a larger set of cases with higher spatial and temporal resolution data is unknown.

The purpose of this chapter is to determine:

- whether the trough evolution and frontogenesis and stability evolution presented in chapters 2 and 3 is representative of a larger sample of banded events.
- how the evolution of midlevel frontogenesis and stability relate to larger scale cyclone features, such as the trowal and upper PV distribution.
- the relative frequencies of various instabilities during band evolution.
- what spectrum of cyclone types produce intense single bands, and
- distinguishing characteristics between cyclones with closed midlevel circulations that develop comma-head bands and those that do not.

To accomplish these goals, a dataset of banded and null (defined in section 4.2a) events during the 2002–2008 cool seasons is developed. Unique to this study is the use of high temporal (hourly) and spatial resolution (~20-km grid spacing) analyses. These analyses are used to explore the mesoscale forcing and stability evolution during banded events through statistical and composite analyses, with particular comparison to the case study findings presented in chapters 2 and 3.

Section 4.2 presents the case selection and analysis methodology. Section 4.3 presents the results from statistical analysis. Section 4.4 presents analysis of banded cyclone types, and section 4.5 explores the evolution of banded and null events. A discussion of the results and summary schematics are presented in section 4.6.

4.2 Data and methodology

a. Case selection

Following the methodology of Novak et al. (2004), heavy precipitation cases over the northeast U.S. were identified during the 2002–2008 cool seasons (Oct–Apr). As in Novak et al. (2004), the study domain was a latitude-longitude box covering 36.5–50N and 65–85W. The National Oceanic and Atmospheric Administration (NOAA) Daily Weather Maps series (NOAA 2008) were used to identify cases that exhibited daily (24-h) precipitation amounts greater than 25.4 mm of rain or 12.7 mm liquid equivalent in the case of frozen precipitation at any station in the domain. This resulted in the identification of 144 heavy precipitation cases or ~24 cases per season on average (Fig. 4.1), which is comparable to the seasonal average found by Novak et al. (2004) during the 1996–2001 cool seasons (~22 per season).

The focus of the current study is single-banded events occurring in the comma-head of cyclones. Single-banded events are defined as the occurrence of a linear reflectivity structure 20–100 km in width, > 250 km in length, with an intensity > 30 dBZ maintained for at least 2 h (Novak et al 2004, and section 1.1a). An example of a single-banded event was shown in Fig. 1.2. More than one single-banded event may occur during the same heavy precipitation case. Novak et al. (2004) found that a majority of single-banded events occurred in the comma-head sector of cyclones. To identify cases with likely comma-head signatures, the presence of a 700-hPa closed low was used as a proxy for the presence of a comma-head. Three-hourly NARR data was examined to identify cases exhibiting a midlevel (700 hPa) closed low at some time during their evolution over the study domain. Seventy-five cases met this criterion (52% of the identified heavy precipitation cases) (Fig. 4.1). The remaining 69 cases were not examined further, as they did not exhibit a 700-hPa closed low.

Two-kilometer resolution WSI Corporation national mosaic radar data and hourly Rapid Update Cycle (RUC) (Benjamin et al. 2004) analyses for the 75 cases were obtained for further study. The RUC data was archived on a 20-km horizontal grid spacing with 37 vertical levels (25-hPa resolution). The RUC model has undergone several changes over the time period of the 56 cases (specified at http://ruc.noaa.gov/RUC20.changelog.html), including a change from an optimal interpolation analysis scheme to a 3-d variational analysis on 27 May 2003, and a change in horizontal resolution from 20 to 13 km on 28 June 2005.

Radar data was examined for the 75 heavy precipitation cases with closed 700-hPa lows to identify single-banded events. Thirty-six single-banded events were identified in the comma-head of the sample set of cyclones (Fig 4.1). The band formation time (or start time) of each banded event is the time at which the reflectivity structure first meets the single-banded event criteria, and this time will be referred to as t=0. Start times of the banded events and their durations are listed in Table 4.1. Subsequent times prior to or after band formation will be designated (for example, t=+2 refers to 2 h after band formation, while t=−2 refers to 2 h prior to band formation) and the time of band dissipation will be referred to as t= end. Band maturity is considered the midpoint (in time) between t=0 and t=end. An example time line for a four-hour duration banded event is shown in Fig. 4.2. The 36 banded events were identified within 30 cases (3 cases exhibited multiple events).

The remaining 45 cases which exhibited a 700-hPa low, but failed to develop a single band in the comma-head were analyzed. Review of radar data revealed a spectrum of precipitation organizations. A transitory null event was defined as period when a 700-hPa closed low was developing or had entered the study domain (determined using RUC data), and only transitory banding occurred. Novak et al. (2004) defined transitory banding as the occurrence of a reflectivity structure that meets all respective criteria in a category (intensity, duration, shape) except one (usually the duration). For example, a linear reflectivity structure was observed in western New England at 0500 UTC March 24 2005 (Fig. 4.3c). This feature met the duration and shape thresholds for a single band, but not the 30 dBZ intensity threshold (Fig. 4.3c), and thus was categorized as a transitory null event. A null event was defined as a time period when a 700-hPa closed low developed in the study domain, but the precipitation shield did not exhibit single or transitory banding. Thus, in null events the precipitation shield met at most only 1 of the 3 single band criteria (intensity, duration, shape)[3]. An example of a null event is shown

---

[3] A null event definition of meeting none of the single band criteria was explored (strict nulls), but the sample was small (11 events) and there was no statistically significant difference in the frontogenesis and stability between the more generous null definition dataset (22 events).

for 0600 UTC 13 Apr 2007 (Fig. 4.3e). Twenty transitory null cases and 22 null cases were identified (Fig. 4.1). The beginning of the transitory null and null events (t= 0) was defined as the time when the 700-hPa closed low entered the study domain or when the low first formed. The start times of the 22 null events are listed in Table 4.2. The end of the transitory null and null events (t=end) was chosen five hours after their start times, which was the mean duration of the banded events. An example time line for a null event is shown in Fig. 4.2b. Three cases were not classified due to missing radar data. Particular focus will be placed on the 36 banded and 22 null events.

b. Cross section analysis

RUC analyses and radar data were used to characterize the environmental evolution of the 36 single-banded events, and compare with the 22 null events. Cross sections of Petterssen (1936) frontogenesis, θ_{es}, EPV (eqn. 2.2), and RH were taken normal to the most intense part of the observed band as in section 2.4d and Evans and Jurewicz (2009). Since the null events did not have a defined band, cross sections were taken normal to the 700-hPa frontogenesis maximum. If a 700-hPa frontogenesis maximum was not present, the cross section was oriented normal to the 1000–500-hPa thickness gradient through the meso-α scale precipitation area in the vicinity of the 700-hPa low. Example radar mosaic images and cross sections are shown for the banded (Figs. 4.3a,b), transitory (Figs. 4.3c,d), and null (Figs. 4.3e,f) event types. Cross sections were taken following the movement of the band centroid (Lagrangian framework) from four hours prior to the start of the banded event (t=−4 h) to one hour after dissipation (t=end+1). For the null events, cross sections were taken from four hours prior to the start of the null event (t=−4 h) to five hours after the start (t=end), the mean band dissipation time. In both the banded and null event samples, the cross-section orientation at t=0 was used for the preceding hours (i.e., t=−1, t=−2, t=−3, and t=−4). The cross-section orientation at t=end was used for t=end+1 for the banded events.

The frontogenesis maximum within the 800–500 hPa layer was recorded within 100 km of the observed radar band during the band life cycle (t=−4 h to t=end +1 h) for each event. The 800–500-hPa layer was chosen given the association of bands with midlevel frontogenesis (e.g., Sanders and Bosart 1985; Schultz and Schumacher 1999). Conditional stability was assessed in a 200-hPa layer above the frontogenesis maximum, as in section 2.4d. The difference in θ_{es} between the upper and lower level in this 200-hPa layer was recorded (small values represent weak conditional stability, large values represent strong conditional stability) during the band life cycle for each event. Instabilities were also assessed, and will be discussed in section 4.4b. The recorded values of frontogenesis and conditional stability at the time of the example cross sections are shown in Fig. 4.3.

Mean time series of frontogenesis and conditional stability were created for the banded and null events. Because the duration of banded events varied, only hours for which there were cross sections for at least half the banded events were included in the time series. This threshold was met for all hours up to and including t=+3 for banded events. All hours were included in the null event time series, since all events had cross sections.

A bootstrapping approach was used to obtain confidence intervals around the means (Zwiers 1990) for samples which were not normally distributed. For each sample (e.g., t=0 banded event frontogenesis values) a new sample of the same size was generated by randomly selecting from the original samples, and allowing for repeated selections. A new sample was generated 1000 times, and the 90% confidence intervals around the mean were determined by finding the 5th and 95th percentile of the means of all 1000 resamples. If the confidence intervals of the banded and null samples do not overlap, then they are significantly different at the 90% level.

c. Composite analysis

Composite analyses for the banded and null event evolution were developed. Although Novak et al. (2004) completed composites for single-banded events in the comma-head sector of cyclones based on the 1996–2001 cool seasons, the present work is unique given the fine temporal and spatial resolution of the RUC data (hourly 20 km analyses versus 6 hourly 80 km analyses). Additionally, the composite results are viewed in a constant pressure and PV perspective in the present work.

Subjective analysis of banded events showed that a 700-hPa trough extending poleward of the 700-hPa low center was nearly always observed within 100 km of the band (also identified in the case studies of chapters 2 and 3). The 700-hPa trough was also evident in many null events near the frontogenesis maximum. Thus, a 700-hPa trough-relative composite framework was utilized[4]. The trough-relative framework more directly elicits the evolution of the band environment than the surface-cyclone-relative framework used in Novak et al. (2004), since bands were more closely correlated with the 700-hPa trough than a particular distance from the surface cyclone.

In the trough-relative framework the 700-hPa low center serves as a common anchor point. The gridded fields are first moved such that the 700-hPa low center for each event is at 40°N and 70°W, which is the mean 700-hPa low position of the sample cyclones at t=0. The gridded fields are then rotated about this point such that the mesoscale 700-hPa trough extending poleward of the midlevel low is aligned north–south. This rotation was counter-clockwise (cyclonic), and varied from 0 (trough aligned north–south) to 90 degrees (trough aligned east–west). This technique was applied to NARR data during 1996–2008 to determine common banded-cyclone types in section 4.4, and applied to the RUC analyses during the 2002–2008 period to explore banded and null event evolutions in section 4.5.

4.3 Frontogenesis and stability evolutions

a. Mean time series

Mean time series of frontogenesis and conditional stability during the life cycle of the 36 banded events (Fig. 4.4) show similar trends as those found in the case studies of chapters 2 and 3. In particular, the mean frontogenesis increases during the early part of the band life cycle, reaching a maximum of 6.1 K $(100\text{ km})^{-1}$ $(3\text{ h})^{-1}$ at t=+2, and then decreases to 2.9 K $(100\text{ km})^{-1}$ $(3\text{ h})^{-1}$ by t=end+1 (Fig. 4.4a). There is a relative minimum in conditional stability at t= 0 [5.0 K $(200\text{ hPa})^{-1}$], and the conditional stability generally increases through the rest of the band duration to a maximum of 6.4 K $(200\text{ hPa})^{-1}$ at

---

[4] A similar composite framework has been applied by Weisman et al. (2002) for investigation of central U.S. inverted troughs.

t=end (Fig. 4.4b). Thus, the frontogenesis and stability evolution established in the case studies of chapters 2 and 3 (Figs. 2.16., 3.26, and 3.25) is common among single-banded events.

The null event time series shows that the frontogenesis is much weaker than the banded event time series. Null frontogenesis values peak near 3 K (100 km)$^{-1}$ (3 h)$^{-1}$ at t=0, and then weaken to near 2 K (100 km)$^{-1}$ (3 h)$^{-1}$ by t=end (Fig. 4.4a). The banded event frontogenesis value is larger than the null event frontogenesis value at the 90% confidence level between t=−3 and t=+3. The mean null event conditional stability at t=0 is 6.1 K (200 hPa)$^{-1}$, while the mean banded event conditional stability is 5.0 K (200 hPa)$^{-1}$ (Fig. 4.4b); however, this difference is not significant at the 90% level. Thus, the conditional stability may be a discriminator between banded and null events, but a more robust discriminator is the strength of the frontogenesis.

b. Individual event analysis

Individual events were analyzed to explore the variability of the stability and frontogenesis evolutions. Individual events were also analyzed to determine the relative frequencies of instabilities, and how these instabilities change during band evolution.

1) STABILITY EVOLUTION

Analysis of individual events revealed that 25 of the 36 banded events (69%) exhibited the lowest or equal to the lowest conditional stability of the band life cycle at t=−1h or t=0, consistent with the mean stability evolution. The mean conditional stability is positive. However, shallow conditionally unstable or conditionally neutral layers (as present in the case studies of chapter 2 and 3) may be masked by the use of a 200-hPa layer θ_{es} criterion, and other instabilities (such as symmetric and inertial instability) may be present. Thus, the stability state for each individual cross section was assessed.

Conditional, symmetric, and inertial stability was assessed in the region bounded below by the frontogenesis maximum, bounded above by the 70% RH contour, and bounded laterally by 2 grid points (40 km) on either side of the location of the frontogenesis maximum. The full wind was used in the calculation of the symmetric and inertial stability, as used in Novak et al. (2006) and discussed by Clark et al. (2002) and Schultz and Knox (2007). If a frontogenesis maximum was not present within the 800–500 hPa layer (a common occurrence among the null cases), the 800–400-hPa layer was assessed within 3 grid points (60 km) of the center of the cross section where RH was >70%. Stability states for a given hour of an event were assigned according to Table 4.3. For example, the hour was considered completely 'stable' if θ_{es} increased with height at a rate greater than 1 K (100 hPa)$^{-1}$, EPV was > 0 PVU, and the absolute vorticity was > 0. However, if θ_{es} *decreased* with height, then conditional instability was noted for that hour. If θ_{es} increased with height at a rate less than 1 K (100 hPa)$^{-1}$, then neutral conditional stability was noted for that hour. CSI was recorded when EPV <0 but θ_{es} increased with height. Inertial Instability (II) was recorded when the absolute vorticity was <0. Multiple instabilities could be present, as defined in Table 4.3.

The results show that only ~20% of the banded events exhibited stable conditions prior to band formation (Fig. 4.5). CI was present in ~30% of events prior to band formation while conditionally neutral conditions increased from less than 20% to ~40% at t=0 (Fig. 4.5). The frequency of CI was approximately double the frequency of CSI, highlighting the importance of shallow elevated layers of CI in band formation. Although previous work has generally focused on CI and CSI instabilities, inertial instability was also present in ~10% of events prior to band formation. As reviewed in section 1.1b, instabilities may appear in combination. Eight of the 36 banded events exhibited either a CI/II or CSI/II combination prior to band formation. After band formation, the frequency of CI, CSI, and II decreases, and reaches a minimum (9%) at the time of band dissipation, while 72% of events exhibit stability at the time of band dissipation (Fig. 4.5). These results are consistent with the observation of increasing conditional stability throughout the band life cycle in chapters 2 and 3.

2) FRONTOGENESIS EVOLUTION

Analysis of the frontogenesis maximum recorded within the hourly cross sections for each event showed that the frontogenesis at t = 0 was larger than or equal to the frontogenesis maximum at t = end in 78% (28) of the events. Perhaps of more interest is the remaining 22% (8) of the cases, where frontogenesis was stronger at the time of band dissipation than at the time of band formation. Five of these cases had stronger conditional stability at the time of band dissipation than band formation, implying that the ageostrophic response to stronger frontogenesis was limited by the increase in conditional stability . Three banded events had relatively weak frontogenesis at t=−1 and t=0, with values less than 2 $(100\ \text{km})^{-1}$ $(3\ \text{h})^{-1}$. However, analysis of stability in these events shows that all events exhibited either conditional instability or neutrality at this time. These results illustrate that not all cases exhibit the same forcing and stability evolution, but in these cases the band evolution behaves according to the fundamental coupled frontogenesis/stability relationship (Sawyer 1956; Eliassen 1962; Emanuel 1985; Thorpe and Emanuel 1985; Xu 1989; Hakim and Keyser 2001).

4.4 Banded cyclone types

In the small sample of three banded cyclone events presented in chapter 3, there were a variety of upper (400 hPa) PV evolutions that supported band development. To better understand the variety of upper PV evolutions that support band formation, band cyclone types were subjectively classified according to the upper PV distribution at t=0. Given the limited number of cases available over the northeast U.S. for type-classification in the RUC era (36), the dataset was extended to include the 1996–2001 cool-season single-banded events (northwest quadrant) from Novak et al. (2004). A total of 72 banded events were identified during the 1996–2008 cool seasons. Since a synoptic classification is not dependent on fine temporal and spatial resolution data, the 3 hourly NARR dataset was used. The NARR analysis closest to the time of band formation was selected for each of the 72 events, and events in each respective class were composited as described in section 4.2c.

Three synoptic types were identified: PV hook, cutoff, and diabatic. The PV hook type was most common, representing 74% of the total events (Table 4.4). The 25 Dec 2002 and 12 Feb 2006 cases studied in chapters 2 and 3 were classified as PV hook. In this type, the upper PV distribution exhibits a PV hook, or PV hook structure, with the band occurring on the poleward flank of the PV hook. The composite of these events shows an occluding surface cyclone (Fig. 4.6a), with 700-hPa frontogenesis exceeding 0.5 K $(100\ \text{km})^{-1}$ $(3\ \text{h})^{-1}$ northwest of the surface cyclone (Fig. 4.6b). The 700-hPa frontogenesis was oriented along a mesoscale trough extending poleward from the midlevel low as in the case studies of chapters 2 and 3. PV advection is found above this region (at 400 hPa) on the poleward flank of the PV hook (Fig. 4.6c). The PV hook has been associated with the trowal (Martin 1999; Han et al. 2007), with the notch of low PV corresponding to the occluded quadrant of developing cyclones (Posselt and Martin 2004). Indeed, the 700-hPa composite shows a midlevel potential temperature ridge (dashed blue on Fig. 4.6b, indicative of the trowal) in the vicinity of the midlevel trough. The band is also found in a region of 400-hPa divergence associated with the left-exit region of an upper (400 hPa) jet (Fig. 4.6d).

The second most common type, representing 14% of the total events, was the cutoff type (Table 4.4). This structure exhibits an isolated upper PV maximum. The composite of these events also exhibits an occluding surface cyclone (Fig. 4.6e), and 700-hPa frontogenesis along a mesoscale trough poleward of the 700-hPa low (Fig. 4.6f). However, the 700-hPa frontogenesis is much weaker than the PV hook cases, with only a small area exceeding 0.25 K $(100\ \text{km})^{-1}$ $(3\ \text{h})^{-1}$. The 400-hPa PV field shows that the cutoff is asymmetric, with a PV lobe extending northeast into New England (Fig. 4.6g). PV advection is found on the northern and western flank of this lobe (similar to the PV hook composite), locally forcing an elongated region of ascent. Also similar to the PV hook composite, the mean band is located in the left-exit region of an upper jet (Fig. 4.6h).

The third type was termed “diabatic”, which represented 12% of the total cases (Table 4.4). The 14 Feb 2007 case studied in chapter 3 was classified as diabatic. The diabatic type is particularly unique, with band formation occurring in the northwest quadrant of the surface cyclone, but to the *east* of the 400-hPa PV trough, and within 300 km of a saturated 700-hPa PV maximum (i.e., diabatic PV anomaly). The composite of these events exhibits a surface cyclone elongated in the north–south direction that is not yet occluded (Fig. 4.6i). Midlevel frontogenesis is found northwest of the surface cyclone, focused in a zone of speed convergence in southeasterly flow (Fig. 4.6j). The upper PV distribution shows that the primary upper trough is well west of the band formation region, although a weak extension is found in the vicinity of the banded event (Fig. 4.6k). The mean band occurs in a region of 400-hPa divergence, associated with coupled jets (Fig. 4.6l)

The above results show that single bands can occur in other synoptic patterns than the PV hook pattern, but that the band is found in the left-exit region of the upper jet, along the axis of the midlevel frontogenesis and upper PV advection. The midlevel frontogenesis and upper PV advection pattern is elongated, providing linear forcing for ascent. Given the common occurrence of the PV hook banded cyclone, the evolution of this cyclone type will be explored further through composite analysis of RUC data, and contrasted with the evolution of null events. The diabatic composite type is also further explored given its unique characteristics.

4.5 Banded and null event evolutions

The high spatial and hourly resolution of the RUC analyses allowed for composite investigation of the evolution of the PV hook, diabatic, and null events. There were 26 PV hook, 7 diabatic, and 22 null events during the RUC era. Composites were calculated as described in section 4.2c from t=−6 to t=end+2 for the PV hook and diabatic events, and from t=−6 to t=end for null events. Low positions and rotation angles were determined for each hour of each event.

To quantify changes in the composite frontogenesis field and diagnose changes in the thermodynamic and kinematic contributions to frontogenesis, a 3° x 2° latitude–longitude box average of frontogenesis, horizontal θ gradient, and normalized frontogenesis (eqn. 3.1) was calculated for the PV hook and null composites. Normalized frontogenesis quantifies the kinematic contribution to frontogenesis, while the θ gradient quantifies the thermodynamic contribution to frontogenesis. The diagnostic box was located along the mean band position, and is overlaid on the composite figures to be presented below.

a. PV hook banded cyclone evolution

Six hours prior to band formation in the PV hook banded event composite, a developing surface cyclone is positioned off the coast (Fig. 4.7a). Although a 700-hPa height trough is not evident, diffluent flow and associated speed convergence is present at this level in central New York, as southeast winds of 30–40 kt ahead of the midlevel low over eastern New York back to an easterly direction and slow to 10 kt over western New York (Fig. 4.7b). Additionally an east–west oriented thermal ridge, representative of the developing trowal, is found north of the 700-hPa low. The speed convergence in the presence of the temperature gradient on the western flank of the trowal results in frontogenesis over central New York. At 400-hPa a PV hook has not yet developed, however, PV advection is concentrated near and to the west of the surface cyclone, in the vicinity of the midlevel low (Fig. 4.7c). Upper divergence associated with the upper-level jet is weak over the band region at this time (Fig. 4.7d).

Six hours later at the time of band formation, the surface cyclone has deepened and is occluding (Fig. 4.7e). The 700-hPa frontogenesis maximum has increased dramatically over the past 6 h, as both the temperature gradient and normalized frontogenesis had increased (Fig. 4.8). The frontogenesis maximum is found just north of the 700-hPa low center, along the newly developed midlevel height trough and maximum thermal gradient (Fig. 4.7f). The flow is strongly frontogenetical as 30 kt southeast winds back to 15 kt northeast winds across the thermal gradient in central New York. Note that the frontogenesis maximum is found at the western terminus of the strong southeast flow, generally north of the trowal axis. At upper levels, the PV structure exhibits the PV hook structure, with a majority of the PV advection occurring in the comma-head region of the cyclone (Fig. 4.7g). The 400-hPa jet and associated divergence have strengthened over the last 6 h (Fig. 4.7h), consistent with greater upper-level forcing for ascent than 6 h earlier.

The cyclone continues to deepen during the band's evolution. At the time of band dissipation, the 1000-hPa and 700-hPa lows are 30 m deeper than at the time of band formation (e.g., cf. Figs. 4.7e,i). The frontogenesis is found on the northern flank of the trowal axis (Fig. 4.7j). Although the 700-hPa temperature gradient is approximately the same as at the time of band formation, the normalized frontogenesis is ~20% less (Fig. 4.8), resulting in a ~15% decrease in 700-hPa frontogenesis. Examination of the composite midlevel flow shows ~30 kt southeast winds turn to ~30 kt northeast winds (Fig. 4.7j). Thus, although there is deformation from the change in wind direction, the speed convergence is less than at the time of band formation. The case studies showed changes in the flow during band dissipation could be attributed to the upscale growth of a remote diabatic PV anomaly (typically east of the band). Conclusive evidence of this process occurring in the composite was elusive, which is likely a consequence of the diabatic PV anomalies occurring in the same general region (east of the band), but at different specific locations relative to the band.

At upper levels at t=end, PV advection continues to be present in the comma-head region (Fig. 4.7k); however, compared to conditions at t=0, the upper jet has weakened (by ~10 kt) and shifted ~100 km farther east of the band region (Fig. 4.7l). Accordingly, the 400-hPa divergence is ~ 3 times weaker than at t=0. The t=end+2 composite exhibits a farther separation between the band region and upper jet (not shown), suggesting upper-level forcing for ascent continues to shift east of the band region after band dissipation.

Cross sections through the band region during the band life cycle (orientations shown in Figs. 4.7d, h, and l) reveal that the midlevel frontogenesis maximum is the vertical extension of the surface occlusion. Six hours prior to band formation as the surface occlusion is forming, a sloping front is already present, embedded within a saturated region (Fig. 4.9a). Conditional instability is found below 700 hPa on the warm side of the frontogenesis maximum, whereas strong conditional stability is present in the immediate band environment, evidenced by the relatively flat θ_{es} contours (Fig. 4.9a). Ageostrophic westerly flow is found below the frontal zone, with ageostrophic easterly flow above the frontal zone and below the jet. Ascent is present above the sloping frontal zone. This cross section is akin to a vertically coupled upper- and lower-level jet–front system, schematically illustrated in Fig. 4.10, where the ageostrophic circulations induced from the front and jet system are coupled and support strong ascent.

Six hours later, the cross section at the time of band formation shows the composite frontogenesis has nearly doubled at all levels, and the θ_{es} gradient associated with the occluded front has increased (Fig. 4.9c). Significant drying has occurred on the eastern side of the cross section; however, the sloping frontal zone remains saturated (Fig. 4.9c). The coupled ageostrophic circulations appear to have strengthened, with the ascent at 600 hPa in the band region nearly double that 6 h earlier. The resemblance to a vertically coupled upper- and lower-level jet–front system (Fig. 4.10) is perhaps most apparent at this time.

The t=0 PV hook composite cross section also shows that the θ_{es} contours are much steeper in the immediate band environment compared to six hour earlier, suggesting destabilization occurred (cf. Figs. 4.9a,c). The case studies showed that the initial destabilization was primarily due to differential horizontal temperature advection. The PV hook composite also exhibits evidence of this process, with the 450–650-hPa layer conditional stability decreasing in the band region from ~7.5 K $(200\ \mathrm{hPa})^{-1}$ at t=−6 to ~6 K $(200\ \mathrm{hPa})^{-1}$ at t=0 (Figs. 4.11a,b). Warm air advection at 650 hPa increases dramatically in the band region during this period to over $3\ \mathrm{x}10^{-4}\ \mathrm{K\ s}^{-1}$ (Figs. 4.11d,e), while the 450-hPa warm air advection is more modest (~$1.5\ \mathrm{x}10^{-4}\ \mathrm{K\ s}^{-1}$) and does not increase (Figs. 4.11g,h). These results are consistent with destabilization due to differential warm air advection.

The cross section at the time of band dissipation still exhibits frontal characteristics, with sloping isentropes and active frontogenesis (Fig. 4.9e). The structure of the wind normal to the cross section is similar to that at t=0. However, the frontogenesis is ~30% less than that at t=0 (cf. Figs 4.9c,e). The upper jet has also shifted eastward, potentially disrupting the ageostrophic coupling present at the time of band formation (cf. Figs. 4.9c,e). The isentropes are also flatter than at t=0 (cf. Figs. 4.9c,e), suggesting stronger conditional stability. Indeed, the composite 450–650-hPa layer conditional stability in the immediate band region has increased to ~6.5 K (200 hPa)$^{-1}$ (Fig. 4.11c). The case study analysis in chapter 3 shows stabilization is primarily due to differential vertical advection associated with the release of instability, consistent with the stability mode evolution analysis (e.g., Fig. 4.5). In a composite sense, Fig. 4.11 also shows that the destabilizing effect of differential warm air advection weakens during band evolution, as the 650-hPa warm air advection has decreased to ~2 K (200 hPa)$^{-1}$ while the 450-hPa warm air advection remains near 1.5 K (200 hPa)$^{-1}$.

b. Diabatic cyclone evolution

Although the diabatic banded cyclone type was rare, its unique PV structure warrants further investigation. Seven diabatic type banded cyclone events occurred during the RUC era. One event (9 Dec 2005) met the type criteria, but the separation distance between the upper trough and diabatic PV anomaly was much smaller (~400 km) than the other six cases (>800 km). Thus, to create a cleaner composite evolution, this event was not included in the composite. Focus is placed on the PV evolution to relate to previous studies.

At t=−6 the 400-hPa PV anomaly is located ~1300 km southwest of the band formation region (Fig. 4.12a), in stark contrast to the 400-hPa PV distribution in the PV hook type (Fig. 4.7c). A saturated (RH >90%) 700-hPa PV anomaly (a diabatic PV anomaly) is located just off the east coast, well east of the upper trough (Fig. 4.12b). PV advection associated with the upper trough is negligible in the vicinity of this 700-hPa PV anomaly (cf. Fig. 4.12a,b). A cross section oriented through the 700-hPa and 400-hPa PV anomalies shows that the 700-hPa anomaly is separated from the 400-hPa PV anomaly (Fig. 4.12c).

During the next six hours, the 400-hPa PV anomaly advances northeast; however, at t=0 it remains >800 km southwest of the band formation region (Fig. 4.12d). Very weak 400-hPa PV advection is found in the band region (Fig. 4.12d). The diabatic PV anomaly strengthened as it advanced up the coast, and is found just south of the mean band formation location at t=0. A second 700-hPa PV anomaly associated with the upper trough is found farther west, over the eastern Great Lakes. This 700-hPa PV distribution is similar to the 14 Feb 2007 distribution at the time of band formation (e.g., Fig. 3.19d). Over the past 6 h, the separation distance between the 400-hPa PV anomaly and diabatic PV anomaly near the coast has decreased ~150 km (cf. Figs. 4.12c,f).

At t=end, the 400-hPa PV anomaly has advanced slightly closer to the band region. For example the 1.0 PVU contour had advanced from western Maryland at t=0 to southeast Pennsylvania at t=end (cf. Figs. 4.12d,g). The diabatic PV anomaly along the coast has strengthened (with PV values >1.8 PVU), and exhibits a northern elongation (Fig. 4.12h). This elongation is likely a reflection of the diabatic PV anomaly associated with the band itself. A cross section shows that the upper and interior PV anomalies were becoming coupled, with the 1.0 PVU contour extending from the surface nearly to the upper-PV reservoir (Fig. 4.12i).

The above composite suggests a two phased cyclone evolution where initially a distinct low-level PV anomaly exists with little upper reflection (t=−6), but evolves to be coupled with an upper anomaly (t=end). This cyclone evolution has been previously demonstrated in extratropical cyclones (e.g., Gyakum et al. 1992; Wernli et al. 2002; Moore et al. 2008). Although not explicitly investigated here, such events may be dominated by diabatic Rossby vortex processes (Montgomery and Farrell 1991; Moore and Montgomery 2004, 2008). Indeed, Moore et al. (2008) assert that a diabatic Rossby vortex played in integral role in the 24–25 Feb 2005 snow event over the eastern U.S. The composite cross section evolution (Figs. 4.12c,f, and i) is strikingly similar to the cross section evolution in their case (their Fig. 6). Future investigation of the frequency of such events over the eastern U.S. (regardless of whether they are banded) is encouraged.

c. Null cyclone evolution

The PV hook and null composites are similar synoptically; thus, a comparison between the PV hook and null composite is made when presenting the null cyclone evolution in this section.

At t=−6 the null composite 700-hPa frontogenesis maximum is nearly equivalent to the PV hook composite frontogenesis maximum at this time (Fig. 4.8). Like the PV hook composite, the frontogenesis maximum is found on the western flank the developing trowal (cf. Figs. 4.13b and 4.7b). Also, as in the PV hook composite, the upper PV distribution had not yet developed a hook, but PV advection was occurring above the surface cyclone (Fig. 4.13c) However, the upper jet and associated divergence were displaced ~100 km farther to the east than in the PV hook composite at this time (cf. Figs. 4.7d and 4.13d)

Six hours later (t=0), the null composite frontogenesis is approximately half that of the PV hook composite frontogenesis maximum (cf. Figs. 4.12f and 4.7f). Although the null composite 700-hPa low had deepened and a midlevel trough had formed during the past 6 h, as in the PV hook composite, the temperature gradient at t =0 is ~10% less and the normalized frontogenesis is ~30% less than the PV hook composite (Fig. 4.8). However, the difference in normalized frontogenesis does not appear until ~2 h prior to band formation (Fig. 4.8), suggesting forecasting techniques relying on precursor observational signals to distinguish banded and null events will have very short lead times. The difference in trends of normalized frontogenesis and θ gradient from t=-4 to t=0, may suggest a "tipping point" in the positive feedback between LHR and increasing frontogenetical forcing just prior to band formation. Close comparison of the composites reveals slightly weaker southeast winds (~5 kt) over eastern New York in the null composite than the PV hook composite, consistent with a weaker midlevel low in the null composite compared to the PV hook composite (cf. Figs. 4.7f and 4.13f). The upper jet and associated divergence are weaker compared to the PV hook composite (cf. Figs. 4.7h and 4.13h). However, in other respects, the composites are similar, with PV advection occurring in the comma-head portion of the null composite cyclone on the poleward flank of the upper PV hook (cf. Figs. 4.7h and 4.13h).

The cyclone in the null composite continues to deepen after t=0 (Fig. 4.13i). Weak 700-hPa frontogenesis is evident at t=0 in the null composite and is even less pronounced at t=end, despite the presence of a temperature gradient, midlevel height trough, and associated deformation (Fig. 4.13j). Diagnostics show that although the temperature gradient is similar to that at t=0, the flow was less frontogenetic (Fig. 4.8). As in the PV hook composite, the upper PV exhibited a PV hook, with PV advection occurring in the vicinity of the midlevel trough in the comma-head (Fig. 4.13k), but the jet is clearly farther east than even the PV hook composite at t=end (cf. Figs. 4.7l and 4.13l). To what degree the location of the jet is sensitive to the presence of a band and associated latent heating is unknown.

Comparison of the PV hook and null composite cross section evolution show that at all times the PV hook composite frontal environment exhibits deeper and stronger frontogenesis, coincident with a stronger frontal zone, especially below 700-hPa (Fig. 4.9). CI is also less prevalent in the null cross sections, as the isentropes are generally flatter than the PV hook composite between 500 and 850 hPa. The ascent is ~25% weaker at t=0 (cf. Figs. 4.9c,d), with potentially less vertical coupling of the jet−front system. The upper jet maximum in the null composite is also ~15% less than the PV hook composite (Fig. 4.9), suggestive of a weaker cyclone.

d) Distinguishing characteristics between banded and null events

The spatial composites and cross sections suggest that the PV hook banded cyclones are deeper than the null cyclones. To test this hypothesis, the central sea-level pressure for each banded cyclone was recorded from t=−6 to t=end+2, and from t=−6 to t=end for the null cyclones using the RUC analysis.

Figure 4.14 shows the mean sea level pressure (MSLP) for each banded cyclone type, all banded events combined, and all null events. All types exhibit cyclone deepening. Although the band time series is ~1.5 hPa deeper than the null time series, this result is not significant at the 90% confidence level using a two-tailed student t-test (Wilks 1995, section 5.2). However, the different cyclone types exhibit different deepening rates, ranging from the rapidly deepening diabatic cyclone (~12 hPa from t=−6 to t=end+2) to the modest deepening of the cutoff cyclone (~5 hPa) (Fig. 4.14). Although the deepening rate is similar to the null events, the PV hook cyclone central pressure is ~4 hPa deeper than the null cyclone MSLP at all times (Fig. 4.14). The result that the PV hook cyclone is deeper than the null cyclone is significant at the 90% confidence level. Thus the central pressure is a distinguishing characteristic between null and treble clef banded cyclone types.

Distinguishing characteristics between banded and null events include the strength of the frontogenesis, and to a lesser degree, the stability (e.g., Fig. 4.4). In general, banded events exhibit stronger frontogenesis and weaker stability than null events. However, there is a spectrum of environments associated with banded and null events. To illustrate this spectrum a scatter plot of the stability and frontogenesis values (time averaged from t=−1 to t=+1) for the 36 banded and 22 null events was developed (Fig. 4.15). Linear regression trend lines were calculated. The null event trend line shows that if a null event has large frontogenesis it typically also has large stability. For the banded events there is little relationship between increasing frontogenesis and stability given the large scatter in stability conditions. Thus there are the clearly different scenarios where the frontogenesis is strong and stability is weak (banding anticipated) or where the frontogenesis is weak and the stability is strong (no banding anticipated). However, there is also certainly overlap between the full null and banded event samples. Within this overlap one can see compensating cases where frontogenesis is strong, but the stability is also strong, or where frontogenesis is weak, but the stability is also weak. However, there are also several cases where the frontogenesis and stability are similar, yet one case exhibits banding and the other does not.

Assuming the RUC analysis frontogenesis and stability values are accurate and a representative sample, there are possible physical reasons for the overlap between banded and null event samples. For example, as shown in the composites the midlevel frontal environment is not independent of the upper-level forcing environment. Although both the PV hook and null composite band regions are found in the left-exit region of an upper jet, the PV hook composite jet and associated divergence is stronger. Additionally the null frontal zone and upper jet are more separated than the PV hook composite, inhibiting optimal coupling. It is possible that null events that exhibit relatively strong frontogenesis and weak stability may lack optimal coupling between the lower-level and upper-level forcing, while banded cases with weak frontogenesis and strong stability may exhibit compensating strong upper forcing. Future work exploring this hypothesis is discussed in section 5.3.

4.6 Discussion and summary schematics

This chapter has demonstrated that a common cyclone evolution (PV hook type) and associated band life cycle exists which is consistent with the 25 Dec 2002 and 12 Feb 2006 case study evolutions explored in chapters 2 and 3. A schematic depiction of the plan- and cross-sectional view of the common banded cyclone evolution is shown in Fig. 4.16.

Several hours prior to band formation, an area of weak midlevel frontogenesis is found in diffluent midlevel flow northwest of the developing surface cyclone and downshear of the upper PV anomaly (Fig. 4.16a). The band region exhibits an area of frontogenesis sloping into the cold air, associated with the cyclone's surface warm front (Fig. 4.16b). However, the frontogenesis is relatively weak, and the conditional instability is limited to the cyclone's warm sector. Given the weak frontogenesis and strong conditional stability, ascent is limited (Fig. 4.16b).

During the hours leading up to band formation, frontogenesis dramatically increases and the conditional instability is reduced, as shown schematically in Fig. 4.17. The conditional stability is reduced primarily by differential temperature advection in a layer centered near 500 hPa in moist flow ahead of the upper trough. The midlevel frontogenesis rapidly increases as a mesoscale trough develops. This trough extends poleward of the 700-hPa low (Fig. 4.16c). PV diagnostics shown in chapter 3 reveal that latent heating plays a large role in the development of the midlevel trough and associated frontogenesis, although PV advection along the sharp, elongated poleward edge of the upper PV hook also contributes to trough formation. The LHR of the heavy precipitation (not yet organized into a band) creates a diabatic PV anomaly which induces a frontogenetical circulation. The band develops within this heavy precipitation as frontal collapse occurs in a positive feedback between latent heating, associated flow and temperature changes, and resulting frontogenesis.

The band is found in the left-exit region of an upper jet, in a region of intense forcing for ascent associated with the midlevel frontogenesis maximum along the midlevel height trough and concentrated upper-PV advection along the poleward edge of the developing upper PV hook (Fig. 4.16c). The reduced stability and stronger frontal and jet forcing allows for optimal coupling of the ageostrophic circulations, inducing strong ascent (Fig. 4.16d). The most likely stability state during band formation is either conditionally neutral conditions or conditional instability, although CSI and II may also be present. The presence of an isolated shallow layer of conditional instability as found in the case studies is shown schematically in Fig. 4.16d. As shown in chapter 2, hydrometeor lofting and drift may alter the position of the surface band relative to the ascent maximum. This process, as well as hydrometeor growth, is shown schematically in Fig. 4.16d.

As band formation occurs the stability is restored (Fig. 4.17) due to the release of any present instabilities. However, frontogenesis continues to increase (Fig. 4.17) in response to the increased latent heating and associated induced circulation of the band itself, as shown in chapter 3.

Band dissipation commonly occurs as a consequence of weakening frontogenesis rather than a change in stability. The frontogenesis weakens as a consequence of kinematic flow changes associated with the upscale growth of remote diabatic PV anomalies (typically east of the band) (Fig. 4.16e). The flow in the band region is altered both in terms of wind direction and speed, resulting in reduced deformation/convergence and associated frontogenesis. At the same time, the separation distance between the upper jet and band region increases, inhibiting optimal coupling between the frontal and jet ageostrophic circulations (Fig. 4.16f). Whether the increasing jet−front separation is a contributing cause or effect of band dissipation is not known.

The above results are largely consistent with previous studies and conceptual schematics of band formation (e.g., Fig. 1.5). However, the high spatial and temporal resolution allow for an evolutionary view of the band formation and dissipation process. Features unique to this view include:

- the relation between band formation and development of the upper PV hook,
- the development of a sharp midlevel height trough (serving as a focus for the midlevel frontogenesis),
- feedback between LHR, frontogenesis, and band development,
- that the most likely stability state during band formation is either conditionally neutral conditions or conditional instability, while CSI and II are less common the contribution of remote diabatic PV anomalies to band dissipation via induced changes in flow and associated frontogenesis, and
- the occurrence of band formation in the left-exit region of the upper jet.

The coupled jet structure highlighted in Novak et al (2004, see Fig. 1.4b) was not readily apparent in the PV hook composite constructed with the RUC data. Composites over a larger domain using the NARR (not shown) do exhibit a weak secondary jet in the downstream ridge, as depicted in Novak et al. (2004). However, the large separation distance (>1000 km) between this downstream jet and the band region casts doubt as to the downstream jet's importance in band development for many events.

Not all banded cases exhibit the above cyclone evolution. A minority of banded cyclones may exhibit banding along the periphery of a closed, isolated upper PV maximum (cutoff cases) or banding to the east of the upper PV trough, but within 300 km of a saturated 700-hPa PV maximum (diabatic cases). However, in these scenarios the band was found in the left-exit region of an upper jet in an elongated area of forcing for ascent, as diagnosed by the midlevel frontogenesis and upper-level PV advection. Similarly not all banded events exhibit the frontogenesis and stability evolution shown in Fig. 4.17. However, in each case, the behavior of the band is consistent with the coupled frontogenesis–stability relationship.

Null events exhibited similar synoptic patterns to the PV hook banded events, except that the null events were characterized by a weaker surface cyclone, weaker midlevel frontogenesis, larger conditional and symmetric stability, and less coupling with upper-level forcing for ascent. The most robust (statistically significant) signal was a difference in midlevel frontogenesis intensity, however a scatter plot of frontogenesis and stability for all banded and null events showed that there was overlap of data points in the frontogenesis−stability phase space A portion of this overlap may be associated with varying degrees of coupling between the lower-level and upper-level forcing.

Band formation is a multi-scale problem that involves predicting the evolution of forcing for ascent and stability correctly at multiple levels in a moist atmosphere. The scatter plot results show that some cases may be clearly banded or nonbanded; however, other cases may be sensitive to the exact forcing magnitude, stability state, and jet–front coupling. Further evidence of this sensitivity is the result that differences between banded and null event 700-hPa temperature gradient and frontogenetical flow appear only ~2 h prior to band formation. This may suggest a “tipping point” in the positive feedback between LHR and increasing frontogenetical forcing just prior to band formation. Future work is needed to define the practical predictability limits of band prediction as well as identify meteorological features that influence band sensitivity to improve prediction, as discussed in chapter 5.

Tables

Table 4.1 2002–2008 cool-season banded event start times and durations.

Start time	**Duration (h)**
1800 UTC 16 Oct 2002	7
0700 UTC 17 Nov 2002	3
0400 UTC 12 Dec 2002	2
1900 UTC 25 Dec 2002	7
1900 UTC 7 Feb 2003	3
0200 UTC 21 Mar 2003	4
0900 UTC 11 Apr 2003	3
0500 UTC 12 Apr 2003	9
1600 UTC 6 Dec 2003	6
0300 UTC 7 Dec 2003	2
1000 UTC 7 Dec 2003	2
1700 UTC 7 Dec 2004	2
2300 UTC 26 Dec 2004	7
1400 UTC 8 Jan 2005	2
1400 UTC 23 Jan 2005	3
0700 UTC 1 Mar 2005	7
0600 UTC 29 Mar 2005	3
1700 UTC 9 Dec 2005	6
1000 UTC 4 Feb 2006	4
0900 UTC 12 Feb 2006	9
1600 UTC 20 Oct 2006	3
1900 UTC 16 Nov 2006	4
0800 UTC 24 Nov 2006	4
1500 UTC 14 Feb 2007	8
2200 UTC 16 Mar 2007	5
0600 UTC 17 Mar 2007	2
0000 UTC 16 Apr 2007	10
1700 UTC 3 Nov 2007	4
1500 UTC 26 Dec 2007	4
2100 UTC 26 Dec 2007	10
0400 UTC 1 Jan 2008	8
0400 UTC 2 Jan 2008	6
2300 UTC 27 Jan 2008	8
0700 UTC 27 Feb 2008	5
2000 UTC 1 Mar 2008	5
2300 UTC 4 Mar 2008	3

Table 4.2 Null event start times.

Start time
2300 UTC 13 Dec 2002
1400 UTC 1 Jan 2003
0600 UTC 2 Feb 2003
0800 UTC 17 Feb 2003
2000 UTC 14 Oct 2003
0200 UTC 4 Feb 2004
0900 UTC 1 Apr 2004
1900 UTC 13 Apr 2004
0800 UTC 1 Dec 2004
0000 UTC 11 Feb 2005
0000 UTC 9 Mar 2005
1800 UTC 12 Mar 2005
0600 UTC 2 Apr 2005
0400 UTC 9 Dec 2005
1300 UTC 16 Dec 2005
2200 UTC 29 Dec 2005
0700 UTC 2 Oct 2006
1000 UTC 5 Apr 2007
0100 UTC 13 Apr 2007
1200 UTC 1 Feb 2008
2100 UTC 6 Feb 2008
1200 UTC 8 Mar 2008

Table 4.3 Stability states where CI = conditional instability, CSI = conditional symmetric instability, and II = inertial instability.

Conditional Stability	**Inertially stable**	**Inertially stable and EPV <0**	**Inertially unstable and EPV <0**	**Inertially unstable and EPV <0**
>1 K (100 hPa)$^{-1}$	"Stable"	CSI	II	CSI/II
<1 K (100 hPa)$^{-1}$ but > 0 K (100 hPa)$^{-1}$	"Neutral"	CSI	II	CSI/II
<0 K (100 hPa)$^{-1}$	CI	CI	CI/II	CI/II

Table 4.4 Banded cyclone types and frequency

Type	**# of cases**	**% of total cases**
PV hook	53	74
Cutoff	10	14
Diabatic	9	12

Figures

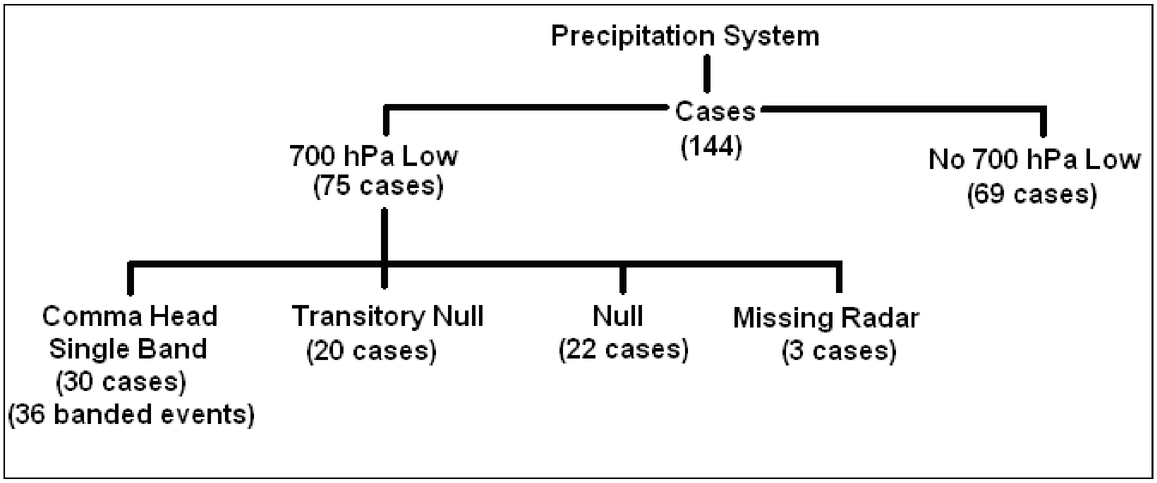

Figure 4.1 Chart of the study method and terminology. The number of each element is denoted in the parentheses.

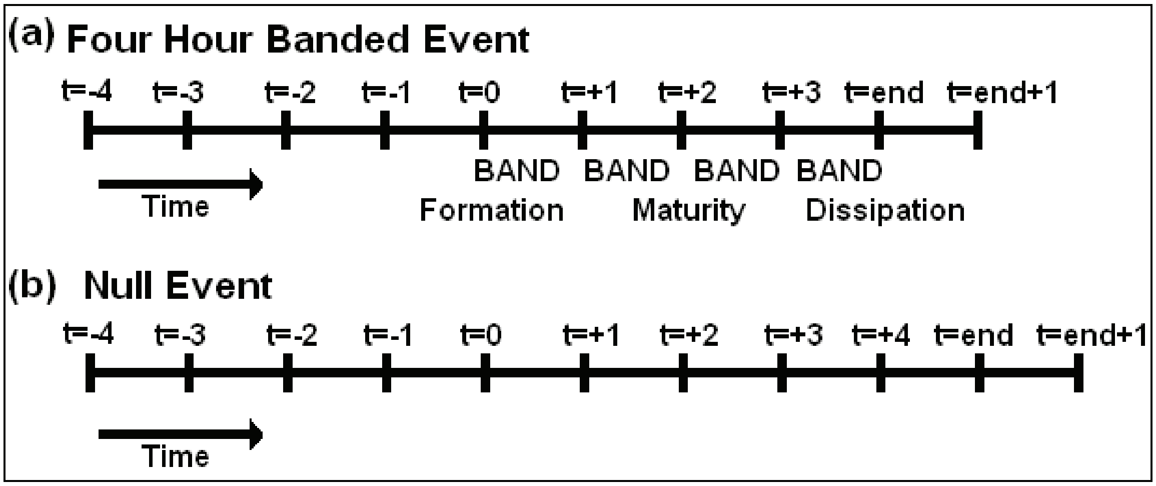

Figure 4.2 Example time lines for (a) a four hour banded event and (b) null event. Time increases to the right, with each tic mark representing one hour. The presence of a band and band life cycle stages are labeled in (a).

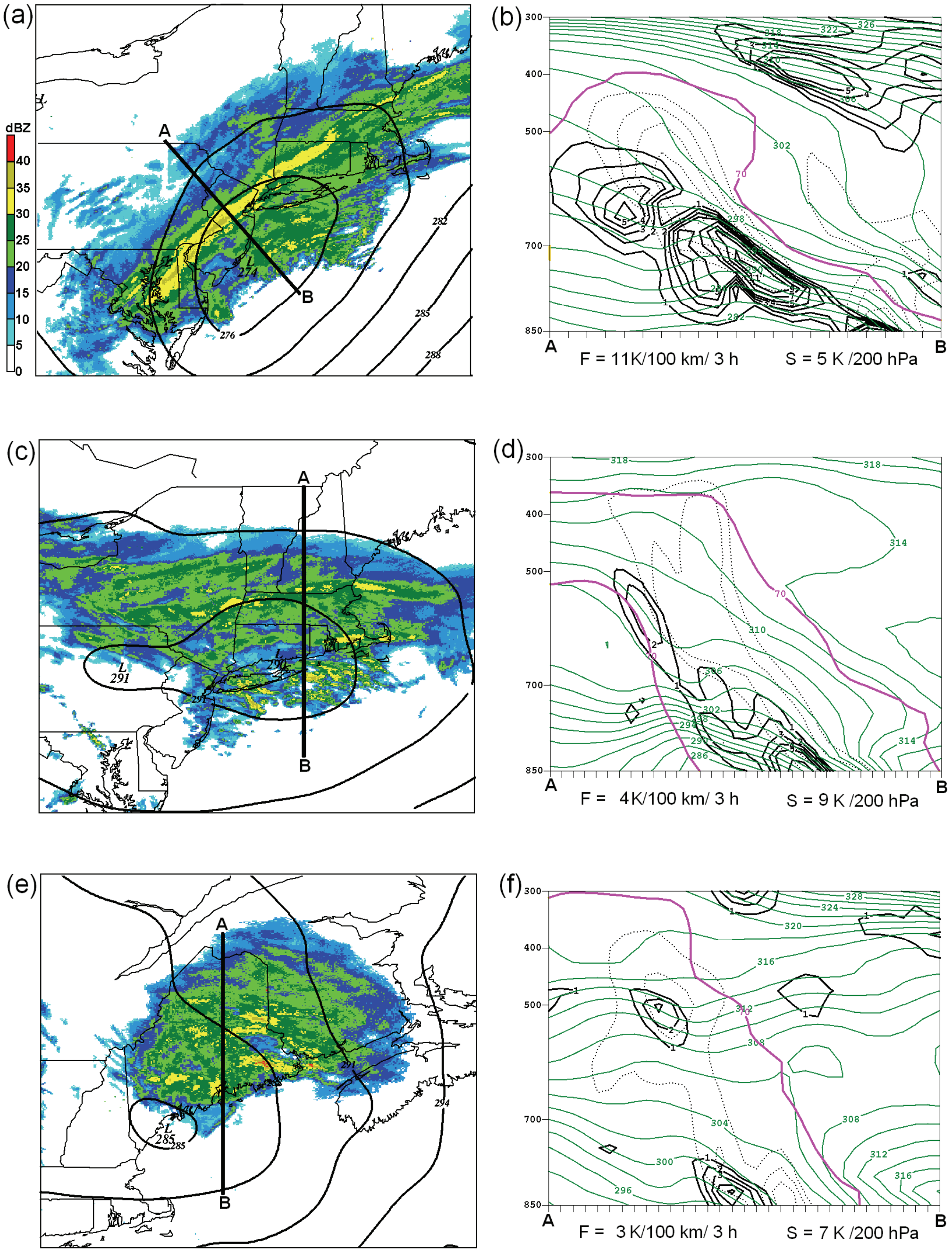

Figure 4.3 Plan-view and cross section examples of (a,b) banded, (c,d) transitory banded, and (e,f) null events valid at (a,b) 1200 UTC 12 Feb 2006, (c,d) 0500 UTC March 24 2005, and (e,f) 0600 UTC 13 Apr 2007. Plan-veiw fields plotted are WSR-88D radar mosaic (dBZ, shaded according to scale) and 700-hPa height (solid, contoured every 30 m). Cross section fields plotted are Petterssen frontogenesis [thick solid, positive values contoured every 1°C $(100\ \text{km})^{-1}$ $(\text{h})^{-1}$ starting at 1°C $(100\ \text{km})^{-1}$ $(\text{h})^{-1}$], saturation equivalent potential temperature (green solid, contoured every 2 K), ascent (dotted, contoured where positive every 10 cm s^{-1}), and the 70% isohume (thick purple). The recorded values of frontogenesis (F) and conditional stability (S) (see text) are shown below the cross section figures.

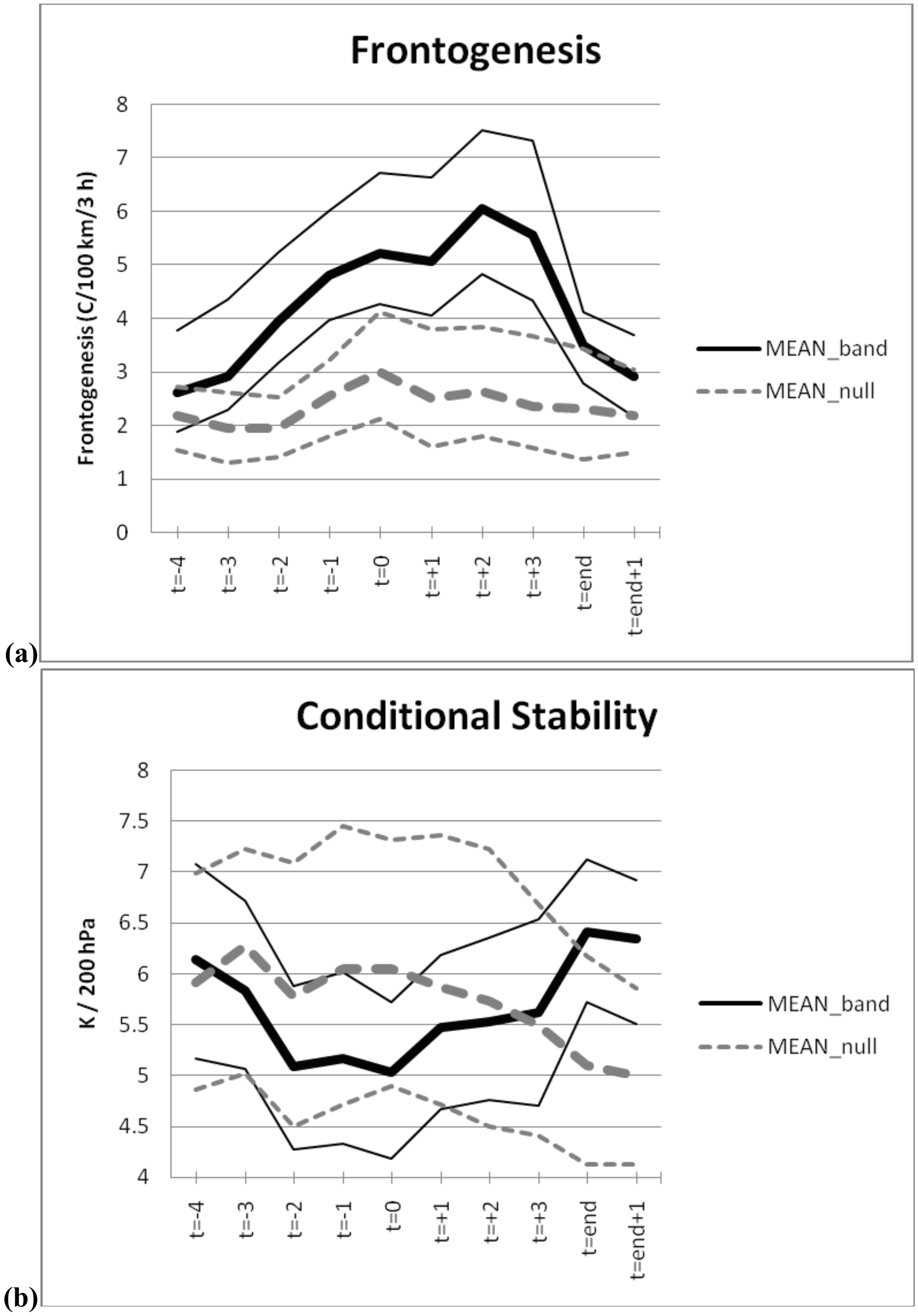

Figure 4.4 (a) Mean time series of frontogenesis (K 100 km^{-1} 3 h^{-1}) during the life cycle of the banded (thick black solid) and null (thick gray dashed) events with 90% confidence intervals overlaid (thin contours). (b) As in (a), except for the conditional stability (K 200 hPa^{-1}).

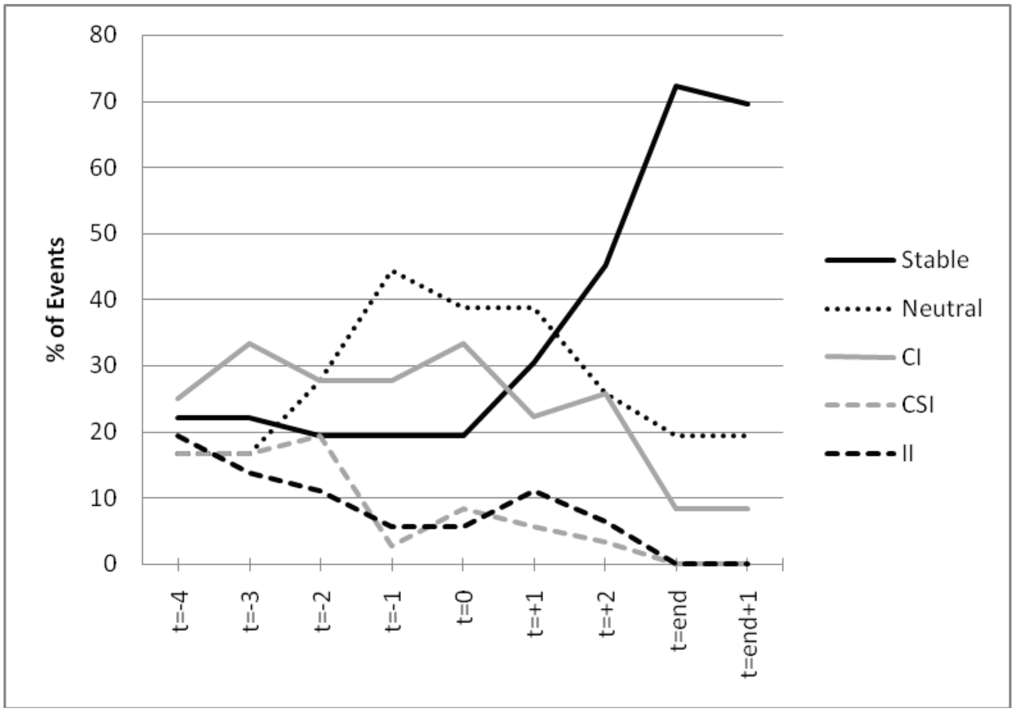

Figure 4.5 Percentage events meeting stable, neutral, conditional instability (CI), conditional symmetric instability (CSI), or inertial instability (II) thresholds as defined in Table 4.3 during the band life cycle of the 36 banded events.

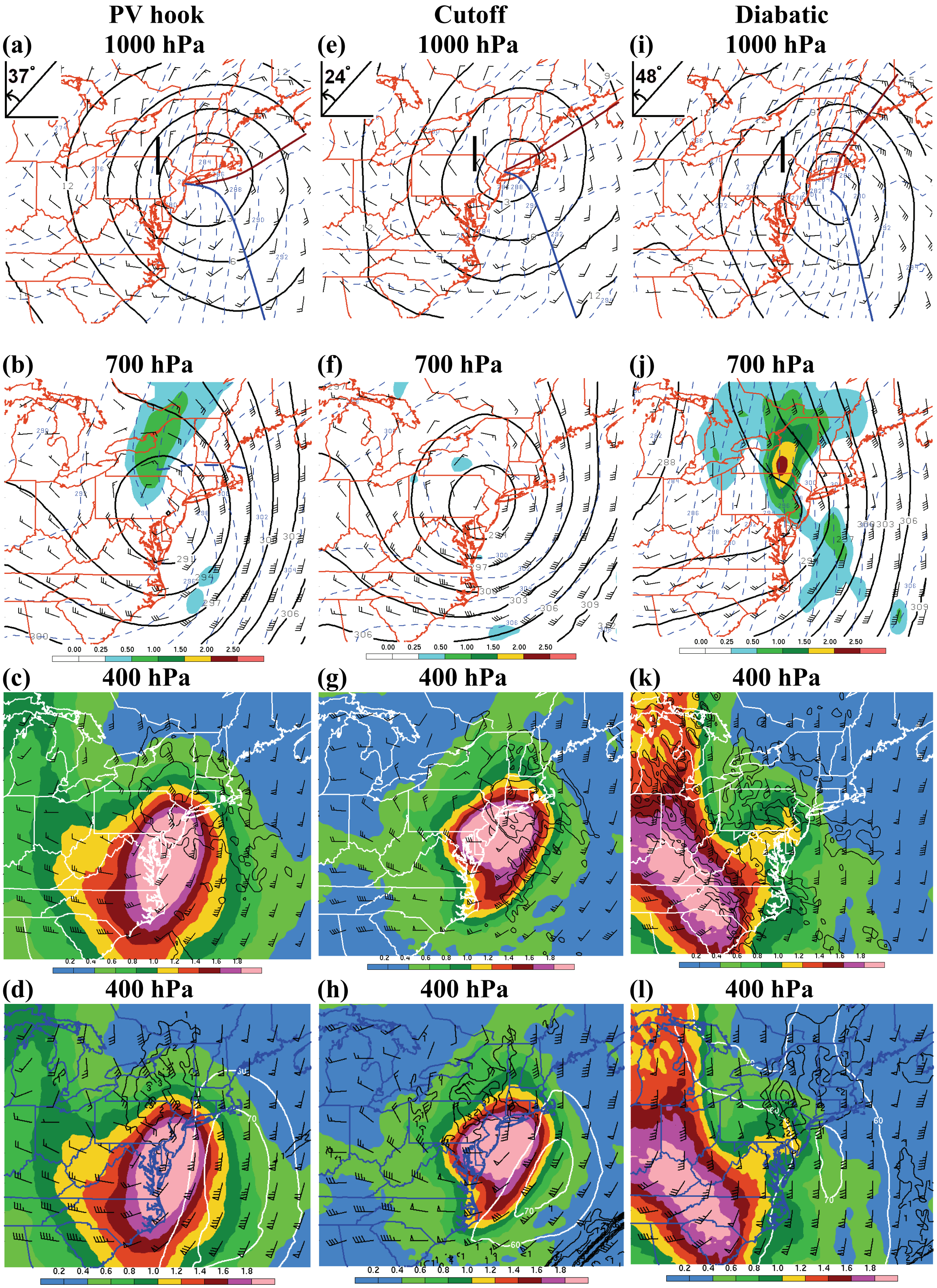

Figure 4.6 (Caption on next page.)

← Figure 4.6 NARR composite fields for (left) PV hook, (middle) cutoff, and (right) diabatic cyclone types near time of band formation, with mean composite rotation angle for each type shown at far left. (top) 1000-hPa height (solid, contoured every 3 m), potential temperature (dashed, contoured every 2 K), and winds (1 barb = 10 kt). Mean band position marked by black line. (middle top) 700-hPa frontogenesis (shaded), heights (thick solid, contoured every 30 m), potential temperature (blue, contoured every 2K), and winds. (middle bottom) 400-hPa potential vorticity (shaded according to scale in PVU), winds, and PV advection (solid, contoured every 1 x 10^{-10} PVU s^{-1}). (bottom) 400-hPa potential vorticity, winds, isotachs (white solid, contoured every 10 kt, starting at 60 kt), and divergence (black thin solid, contoured every 1 x 10^{-5} s^{-1}, starting at 1 x 10^{-5} s^{-1}).

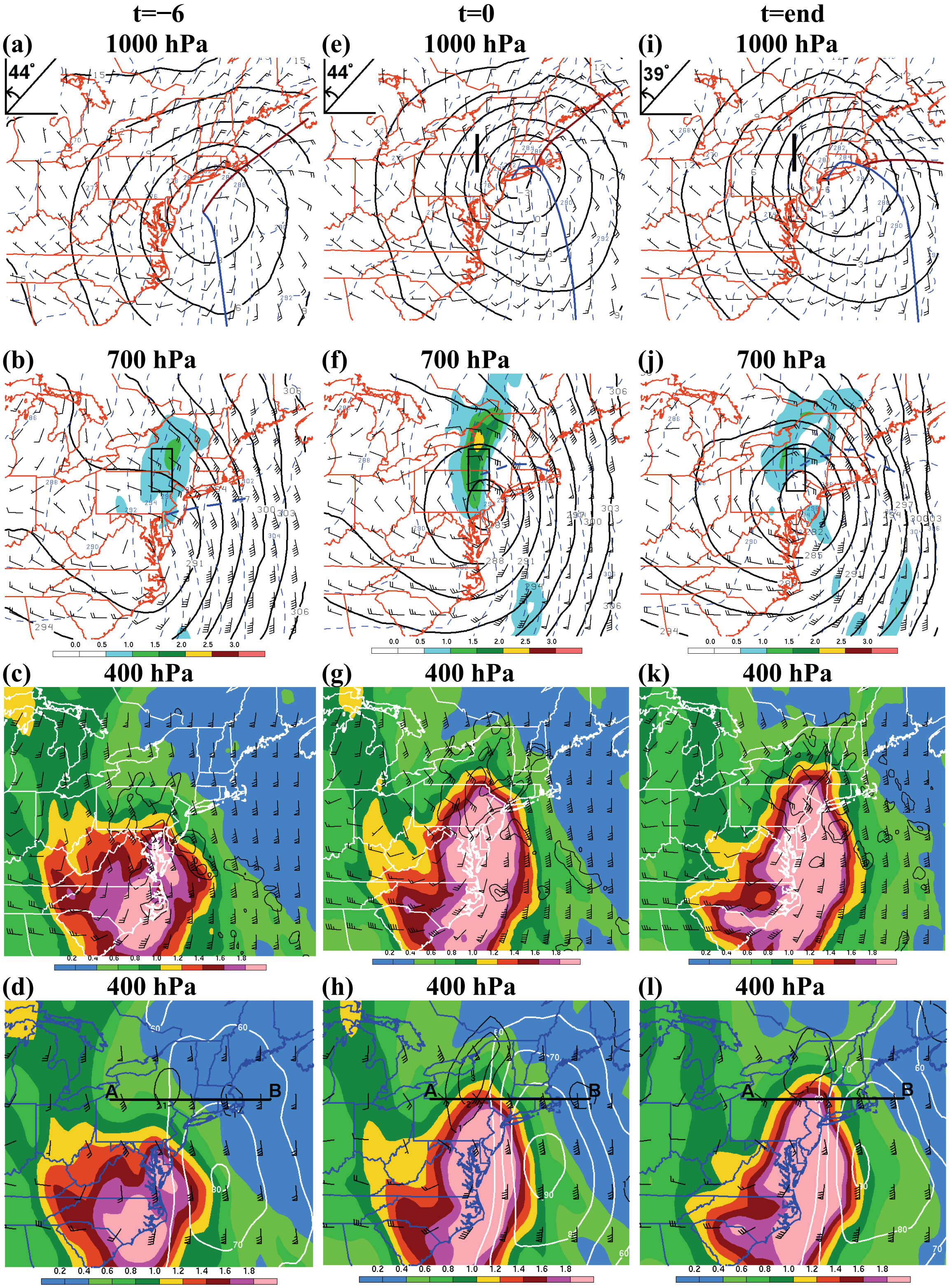

Figure 4.7 (Caption on next page.)

🡐Figure 4.7 As in Fig. 4.6, except for the PV hook banded event composite (left) t=−6, (middle) t=0, and (right) t= end. The trowal axis is denoted as a thick dashed blue line in panels b, f, and j. The diagnostic box is also shown in panels b,f, and j.

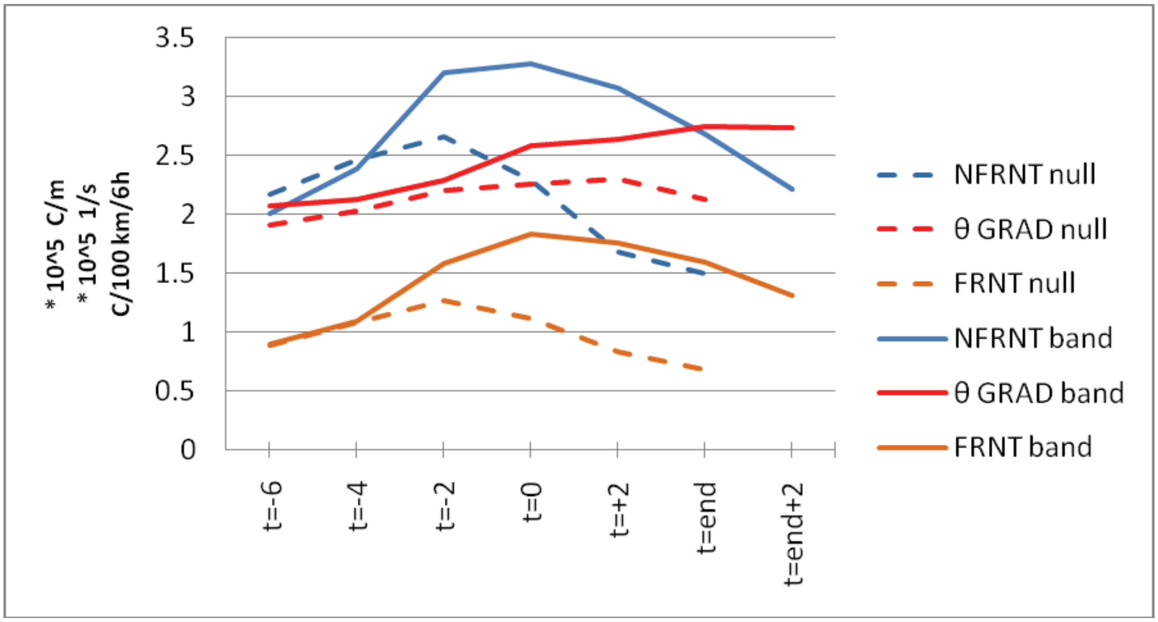

Figure 4.8. Time series of box-average values of frontogenesis (FRNT, orange), potential temperature gradient (θ GRAD, red), and normalized frontogenesis (NFRNT, blue) for the PV hook banded event composite (solid) and null composite (dashed).

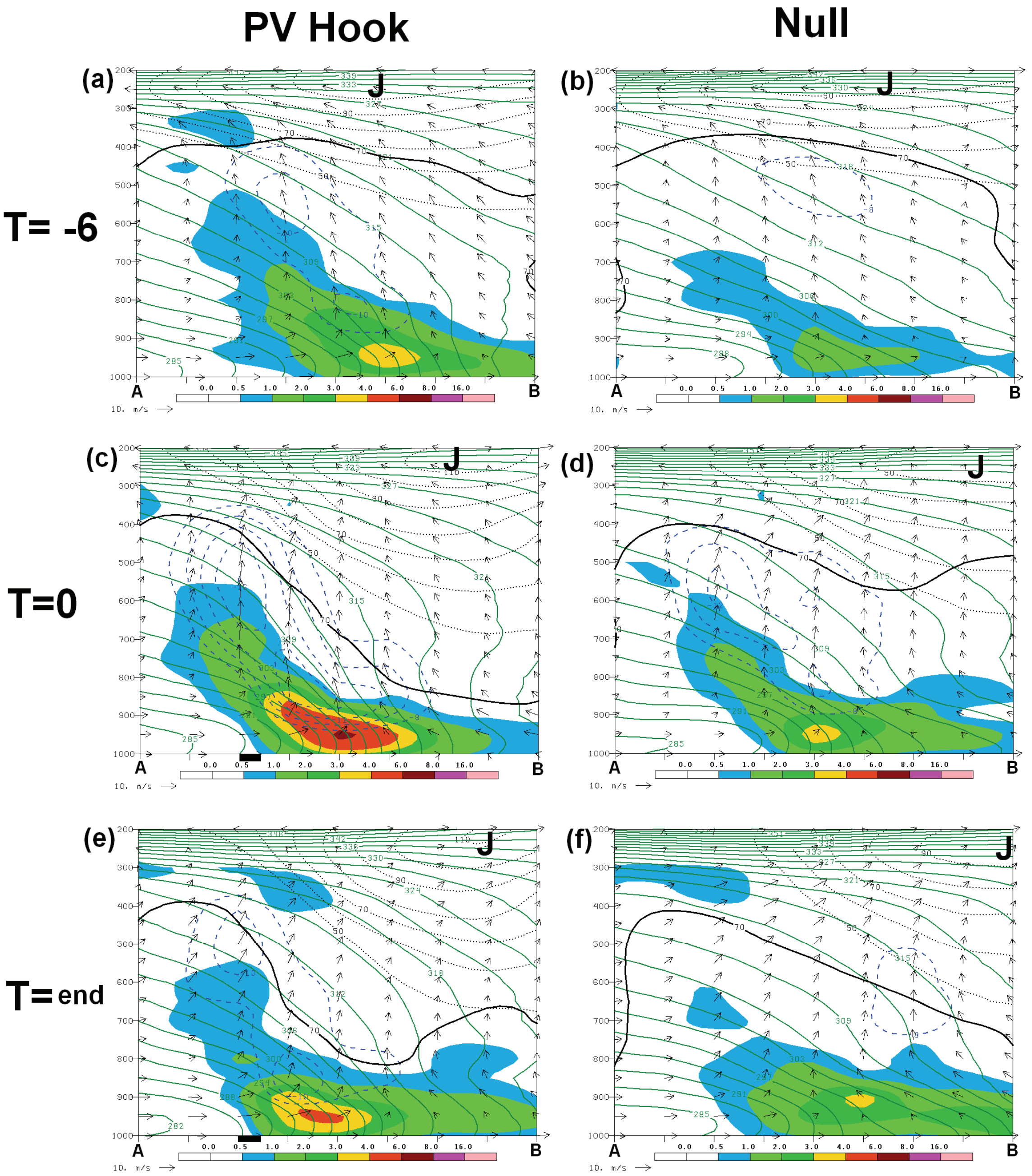

Figure 4.9 (left) PV hook and (right) null composite cross section (orientations shown in Figs. 4.7d and 4.13d) evolution of frontogenesis (shaded), saturation equivalent potential temperature (green solid), wind normal to the cross section [positive (south wind) contoured in black dotted every 10 kt starting at 50 kt], ascent (dashed blue, contoured every 2 Pa s^{-1}), 70% RH isohume (thick black), and ageostrophic wind in the plane of the cross section at (a,b) t=−6, (c,d) t=0, and (e,f) t= end. Mean band position shown as black bar along x-axis and upper jet axis labeled “J”.

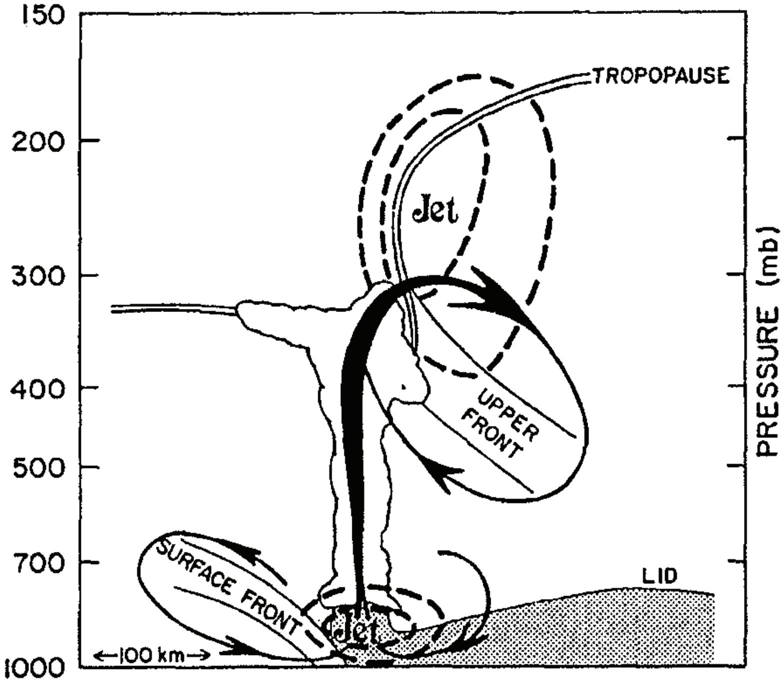

Figure 4.10 Schematic illustration of vertically coupled upper- and lower-level jet−front system. Isotachs are indicated by thick dashed lines surrounding the upper- and lower-level jets, frontal boundaries by thin solid lines, the tropopause by thin double lines, and moist boundary layer by the stippled region, and the transverse ageostrophic circulation by solid arrows. From Keyser (1999, Fig. 10d), as adapted from Shapiro (1982).

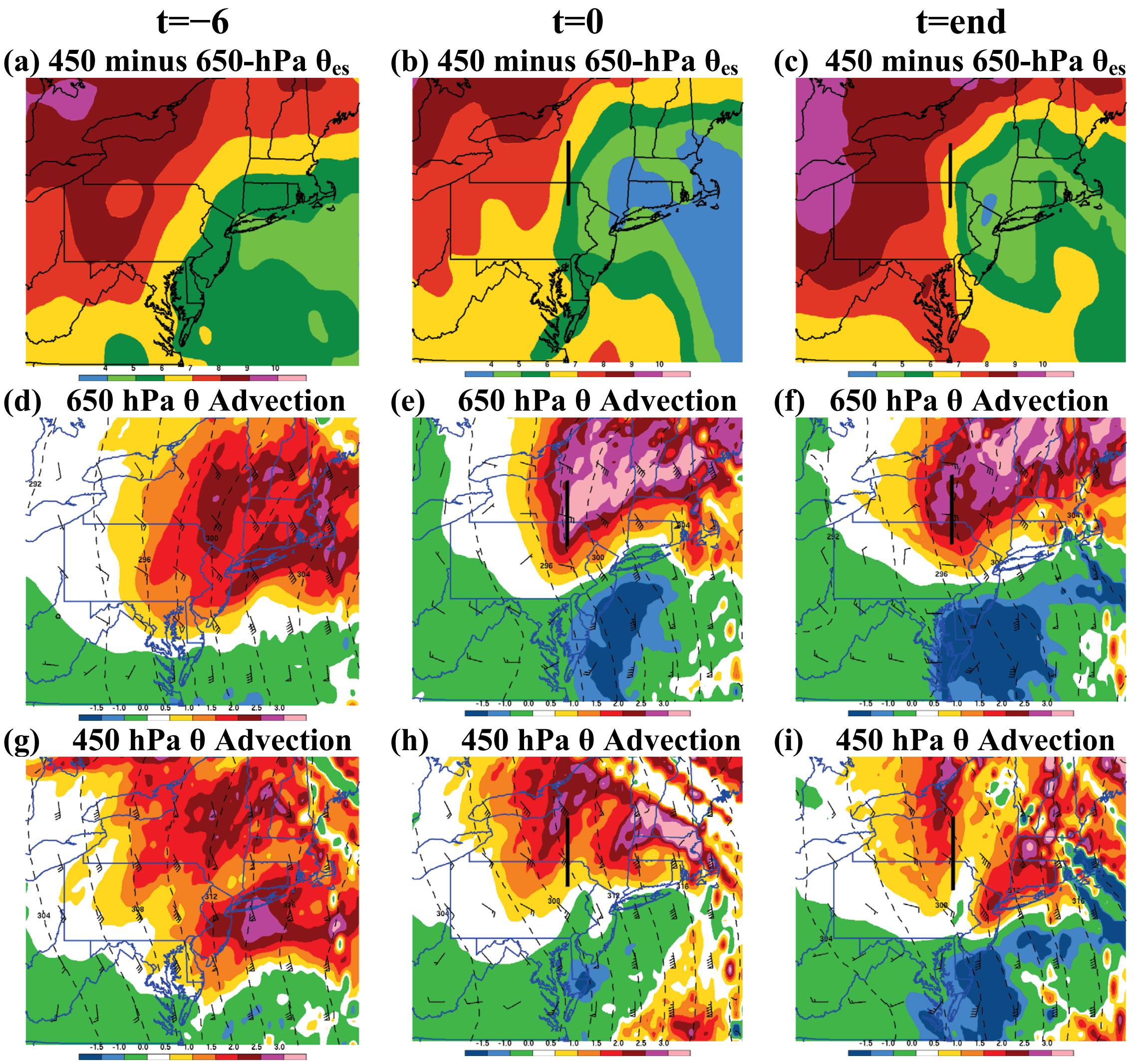

Fig. 4.11 (top) PV hook composite saturation equivalent potential temperature difference (450 hPa minus 650 hPa) evolution, shaded according to scale every 1 K. (middle) Corresponding 650 hPa potential temperature (dashed, contoured every 2 K), wind (1 full barb = 10 kt), and potential temperature advection (shaded according to scale every 0.5 x 10^{-4} K s^{-1}). (bottom) As in (c,d), except for the 450-hPa level. The mean band position is shown at t=0.

t=−6 t=0 t=end

(a) 400 hPa (d) 400 hPa (g) 400 hPa

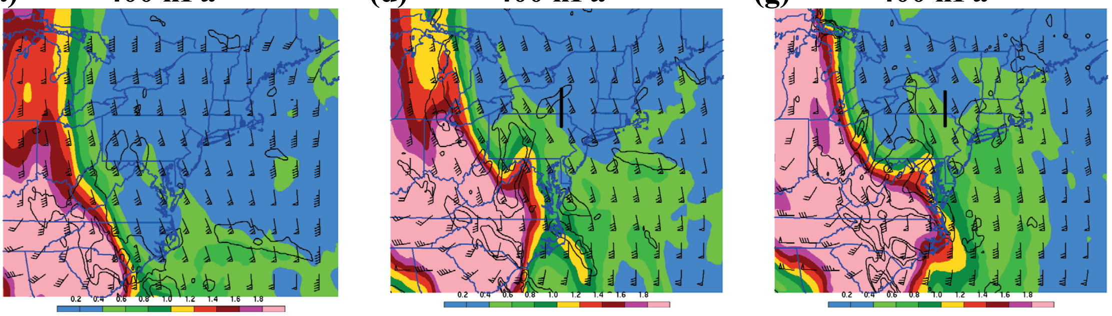

(b) 700 hPa (e) 700 hPa (h) 700 hPa

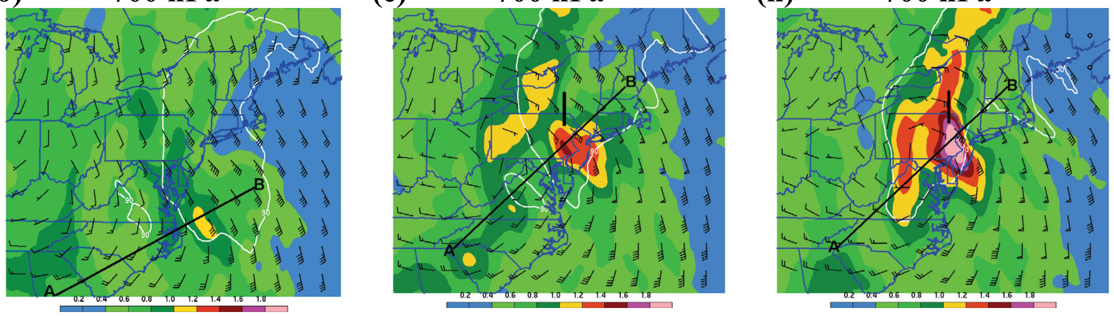

(c) Cross section (f) Cross section (i) Cross section

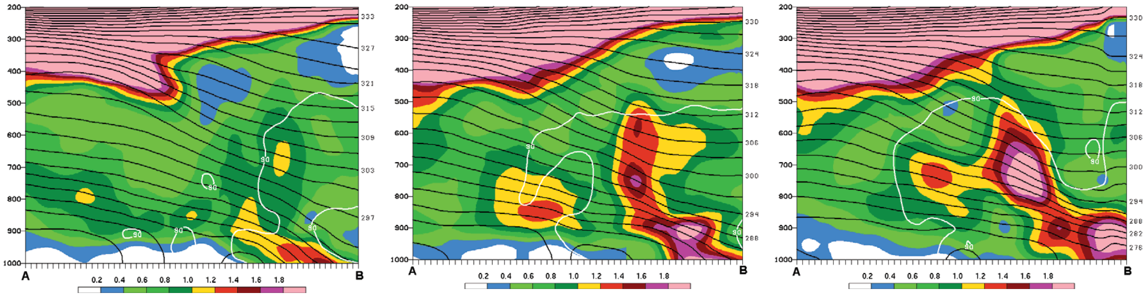

Fig. 4.12 RUC composite fields for the diabatic cyclone type. (top) 400-hPa potential vorticity (shaded according to scale in PVU), winds, and PV advection (solid, contoured every 1 x 10^{-10} PVU s^{-1}). (middle) 700-hPa potential vorticity (shaded according to scale in PVU), winds, and 90% isohume (thick white). (bottom) Cross section of PV (shaded according to scale in PVU), potential temperature (solid, contoured every 3 K), , and 90% isohume (thick white). Cross section orientation shown in middle panels, and mean band position (thick solid) shown in (d), (e), (g), and (h).

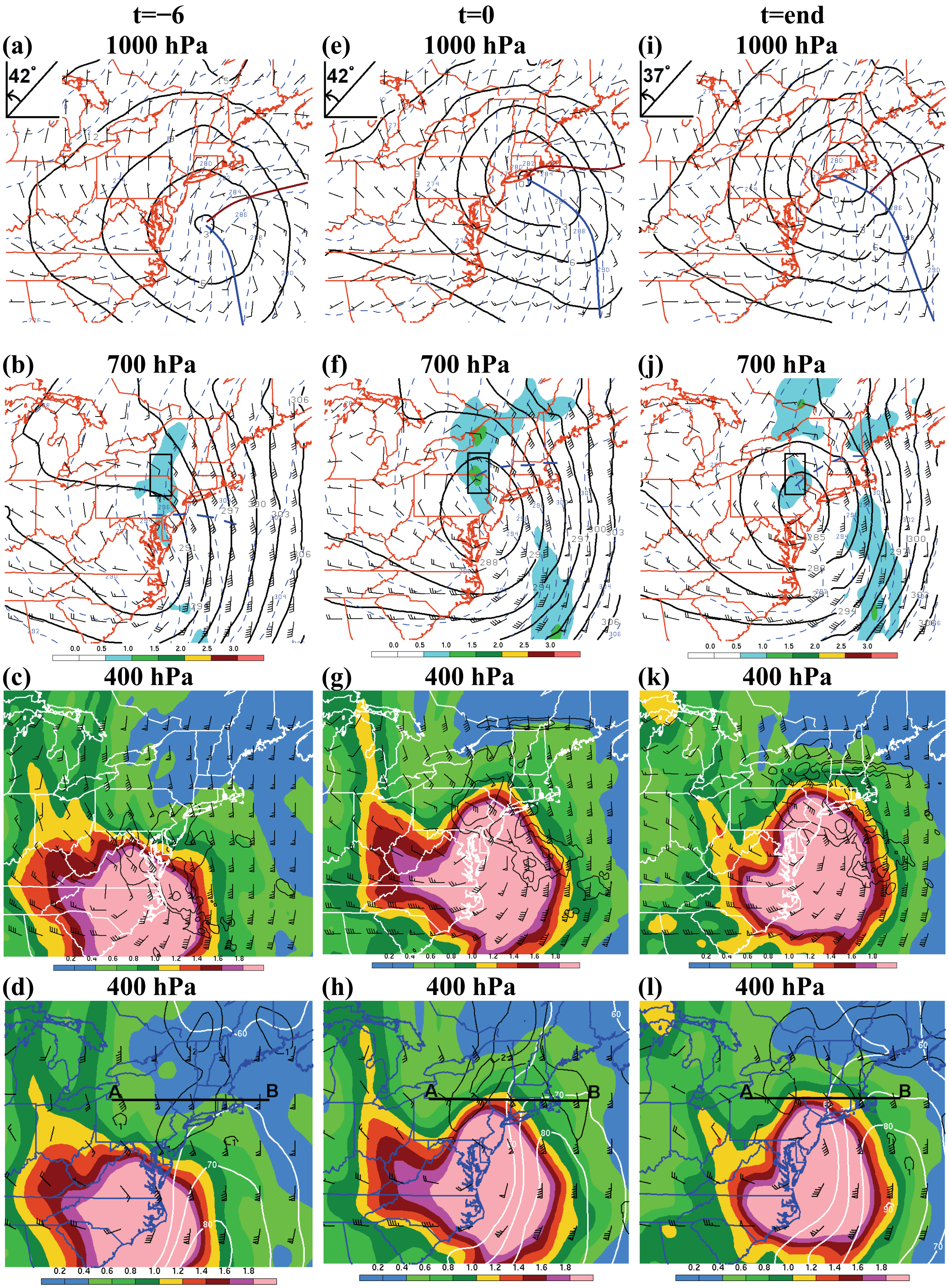

Figure 4.13 As in Fig. 4.6, except for the Null composite (top) t=−6, (middle) t=0, and (bottom) t=5. The diagnostic box is also shown in panels b,f, and j.

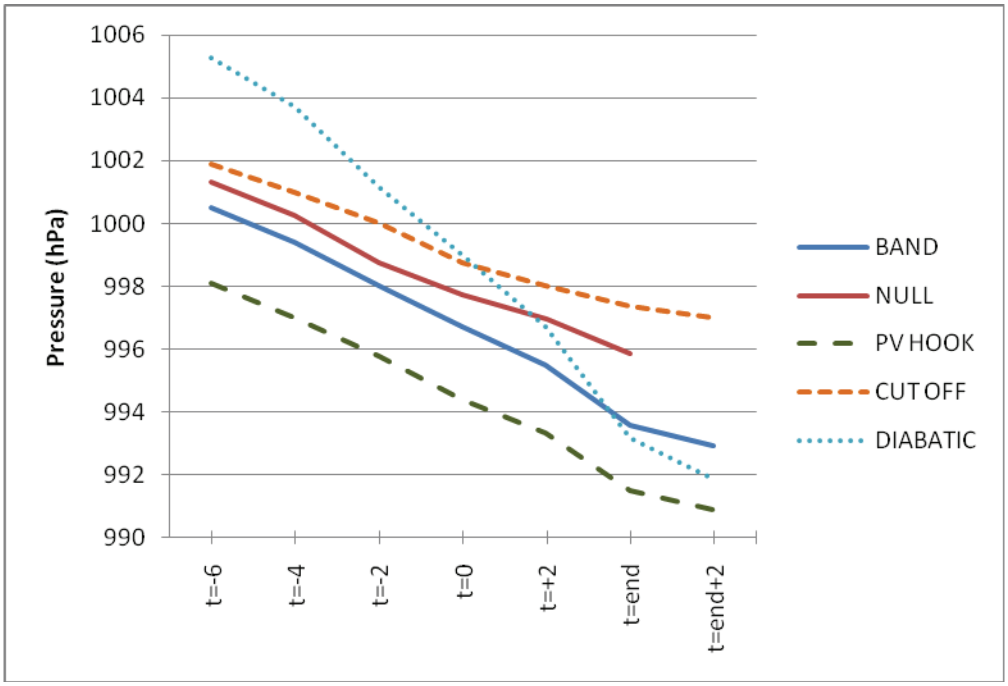

Fig. 4.14 Time series of the mean sea-level pressure for the full banded (blue solid) and null (red soild) cyclones, as well as PV hook (brown dashed), cutoff (orange dashed), and diabatic (blue dotted) cyclone types.

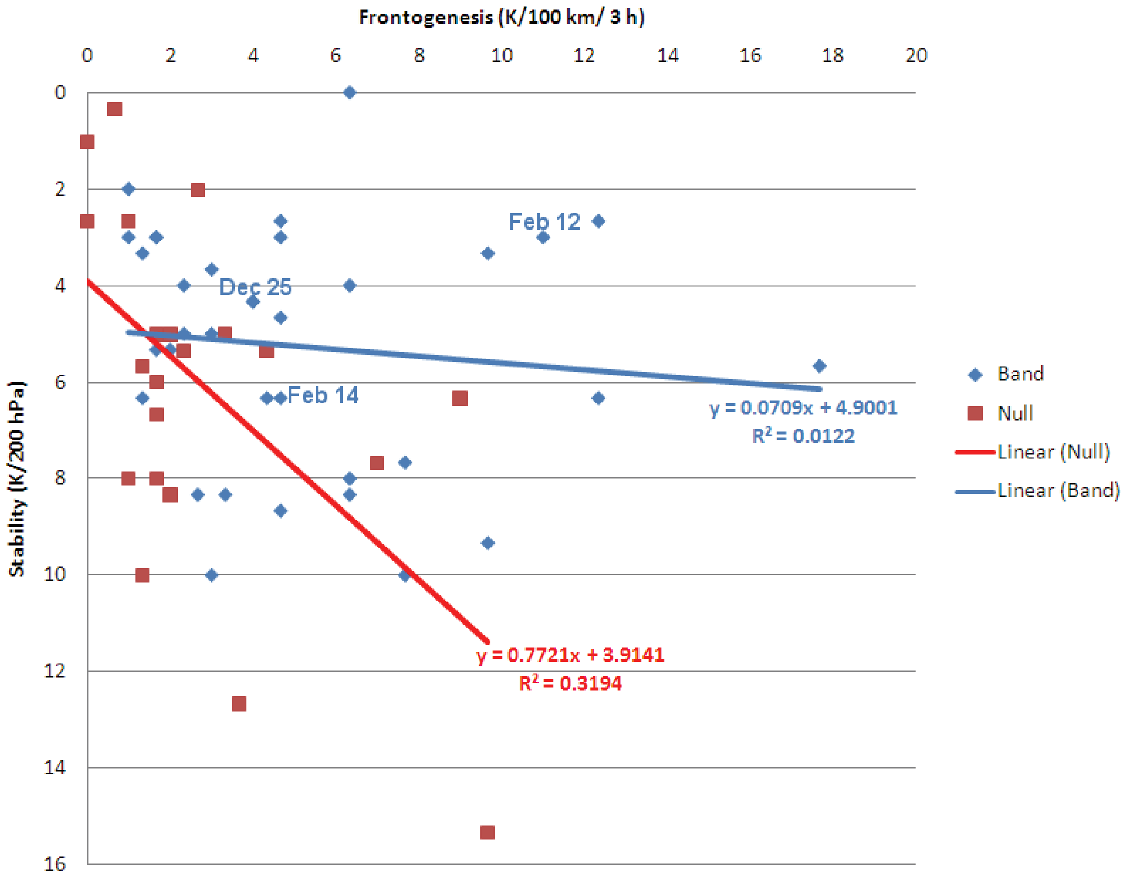

Fig. 4.15 Scatter plot the 3 h time-averaged stability and frontogenesis values centered on t=0 for the 36 banded (blue) and 22 null (red) events. The linear regression lines for the banded (blue) and null (red) are overlaid, with respective equations and R^2 values. The case studies presented in chapters 2 and 3 are labeled.

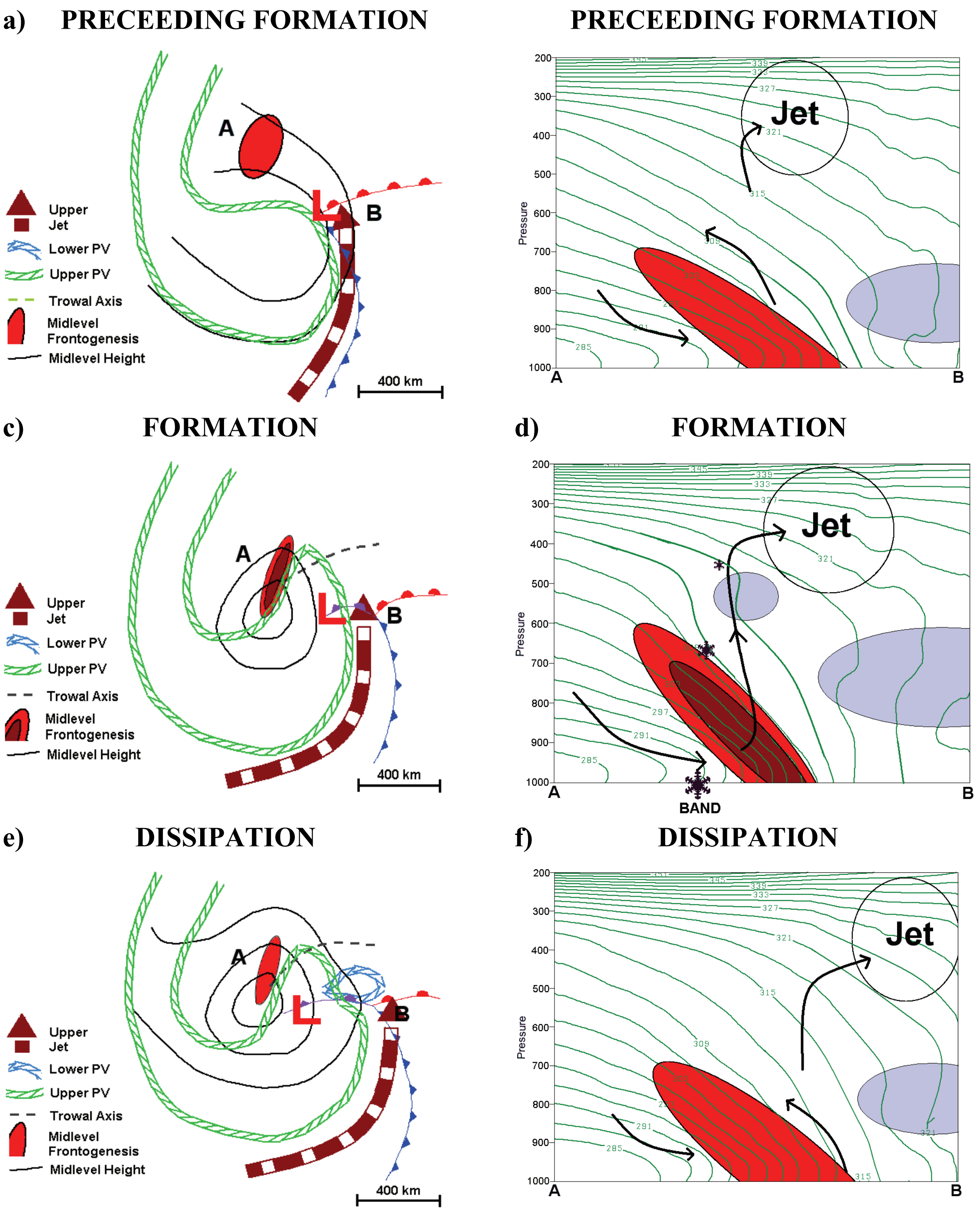

Fig. 4.16. Schematic depiction of the PV hook banded cyclone plan-view (panels a, c, and e) and cross-sectional (panels b, d, and f) evolution. Key features shown in plan-view depiction include upper jet (dashed thick arrow), lower PV anomaly (blue hatched outline), upper PV anomaly (green hatched outline), midlevel trowal axis (gray dashed), midlevel height (thin black), midlevel frontogenesis (red shading), and surface fronts and pressure centers. Cross section end points (“A” and “B”) marked. Key features shown in cross-sectional depiction include frontogenesis (red shading), isentropes (green solid), upper jet (labeled), conditional instability (gray shading), and ageostrophic circulation (arrows). Hydrometeor growth and drift depicted by snowflake in (d) (not drawn to scale).

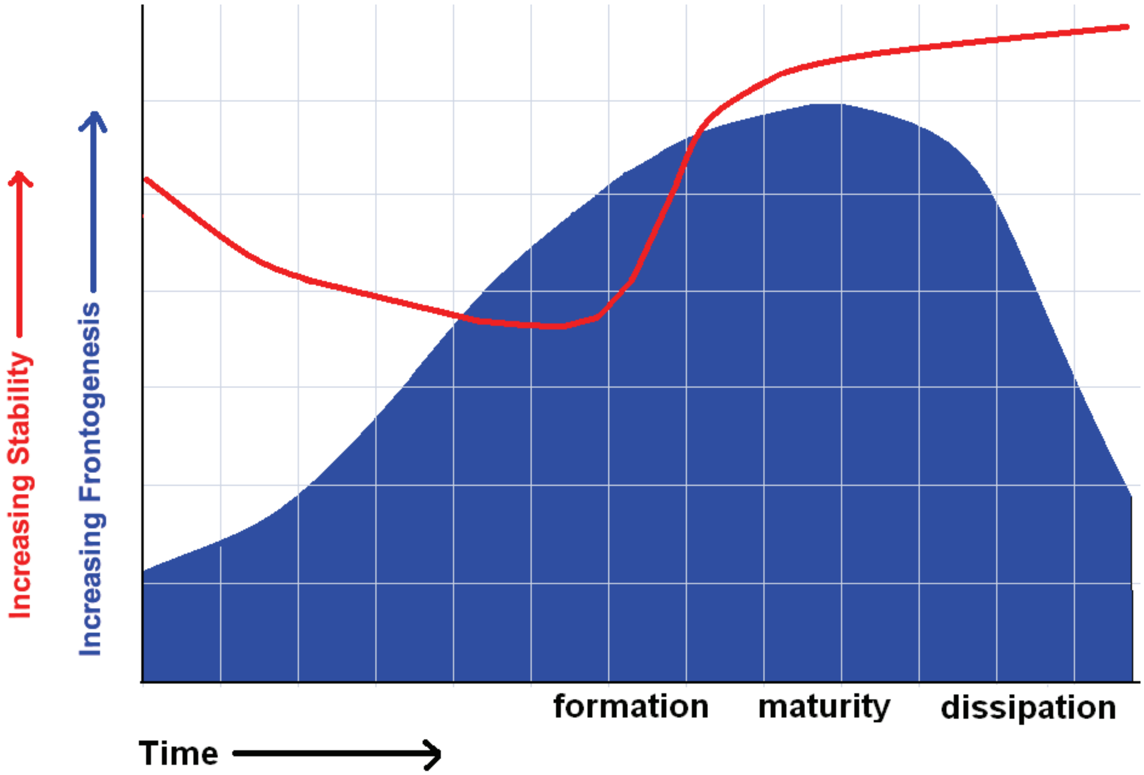

Fig. 4.17. Schematic time series of the midlevel frontogenesis and conditional stability evolution from several hours prior to band formation to band dissipation.

Chapter V:

Summary and Future Work

5.1 Summary

This thesis presents an investigation of the evolution and dynamical processes of solitary precipitation bands within the comma-head of northeast U.S. cyclones. The processes governing the development and evolution of banding events were identified using modern high-resolution observations, analyses, and model simulations, thermodynamic budgets, and sensitivity experiments. In doing so, the thesis has established a common band evolution from genesis to decay associated with changes in ambient ingredients (lift, stability, and moisture) and mesoscale flow patterns.

5.2 New contributions to mesoscale precipitation band research

This research applied non-conventional observations, such as a dual-Doppler wind synthesis from two operational WSR-88D radars, wind profilers, commercial aircraft soundings, and integrated precipitable water vapor observations, as well as high-resolution RUC analyses, model simulations down to 1.33 km, and high-resolution potential vorticity (PV) inversions to the investigation of the evolution and dynamics of solitary precipitation bands. These datasets highlighted aspects of band structure and processes unresolved by previous studies, including the development of a sharp trough to the north of the midlevel low center during band formation, the location of the band relative to the midlevel frontogenesis maximum, feedbacks between latent heat release (LHR) and band development, shallow layers of conditional instability, multiple instabilities, and the time-varying nature of frontogenesis and stability during band life cycle.

Analysis of these datasets revealed a common cyclone evolution (PV hook type) and associated band life cycle undocumented by previous studies. During the hours leading up to band formation, the conditional instability is reduced in the band region. Case studies and composites show stability reduction is primarily due to differential temperature advection in a layer centered near 500 hPa in moist flow ahead of the upper trough. Meanwhile, midlevel frontogenesis in the comma-head region of the developing cyclone dramatically increases as a mesoscale trough develops. This trough extends poleward of the 700-hPa low (Fig. 4.16c). Piece-wise PV inversions at 12 km grid spacing illustrate that the mesoscale trough and associated frontogenesis forms as a consequence of both dry and moist processes; however, LHR enhances the sharpness of the height trough and associated deformation and frontogenesis. The LHR of the heavy precipitation (not yet organized in a band) generates a diabatic PV anomaly, which induces a frontogenetical circulation. The upscale growth of the diabatic PV anomaly and associated flow supports stronger frontogenesis and ascent. The band develops within this heavy precipitation as frontal collapse occurs in a positive feedback between latent heating, associated flow and temperature changes, and resulting frontogenesis.

The band is found in a region of intense forcing for ascent associated with the midlevel frontogenesis maximum along the midlevel height trough, concentrated upper-PV advection along the poleward edge of the developing upper PV hook. The band is located in the left-exit region of an upper jet. The reduced stability and stronger frontal and jet forcing allows for optimal coupling of the ageostrophic circulations, inducing strong ascent.

Assessment of stability above the midlevel frontogenesis maximum (generally within the 700–400-hPa layer) showed that although CSI was observed in ~15% of events prior to band formation, shallow (~50–100-hPa) layers of conditional instability were more common (~30% of events). This result was not found in previous studies, such as Novak et al. (2004), who used grids at 80-km horizontal grid spacing with 50-hPa vertical resolution, and contrasts with other previous studies who have focused on CSI as the dominant stability mode associated with comma-head bands (as reviewed by Schultz and Schumacher 1999). The high-resolution data used in the current climatology partially resolved these shallow layers of conditional instability. Inertial instability (II) was also observed above the midlevel frontogenesis maximum in a minority of events (~10%), and it often co-existed with CI or CSI. II diagnosed in the 25 Dec 2002 snowstorm (chapter 2) was determined to be a consequence of the diabatic ridging associated with the band itself. To what degree the presence of shallow CI, CSI, or II layers affects band formation is unknown, but given the enhanced ascent associated with the release of these instabilities, the layers may be critical in some cases.

During band maturity intense midlevel frontogenesis is often offset by an increase in the stability associated with the release of any present instabilities. Frontogenesis and associated vertical motions increase largely as a consequence of latent heating associated with the band itself, which leads to the development of a midlevel trough, associated cyclonic wind flow, and a large temperature gradient. As shown in chapter 2, hydrometeor lofting and drift may alter the position of the surface band relative to the ascent maximum. Additionally, the large inertial stability near the level of frontogenesis (~700 hPa) favors an ascent core nearly coincident with the frontogenesis maximum. This environment of large inertial stability and strong frontogenetical forcing was not considered in previous theoretical work which predicts the ascent maximum 50–200 km on the warm side of the frontal forcing.

Band dissipation commonly occurs as frontogenesis weakens in the established stable environment. The frontogenesis weakens as a consequence of kinematic flow changes rather than changes in the temperature gradient. These kinematic flow changes occur as the upscale growth of a remote diabatic PV anomaly (typically east of the band) alters the midlevel flow around the cyclone. The flow in the band region is altered both in terms of wind direction and speed, resulting in reduced deformation/ convergence and associated frontogenesis in the three cases examined. Also during band dissipation, the separation distance between the upper jet and band region increases, inhibiting optimal coupling between the frontal and jet ageostrophic circulations.

The thesis has also established that a minority of banded cyclones may exhibit banding along the periphery of a closed, isolated upper PV maximum (cutoff cases) or banding to the east of the upper PV trough, but within 300 km of a saturated 700-hPa PV maximum (diabatic cases). However, in these scenarios the band region was found in an elongated area of forcing for ascent, as diagnosed by the midlevel frontogenesis, upper-level PV advection, and upper-level divergence in the left-exit region of an upper jet. Similarly not all banded events exhibit the frontogenesis and stability evolution shown in Fig. 4.17. However, in each case, the behavior of the band is consistent with the coupled frontogenesis–stability relationship.

Distinguishing characteristics between cyclones that have a closed midlevel circulation and develop bands (banded events) and those that have a closed midlevel circulation but fail to develop banding (null events) were investigated. Null events exhibited similar synoptic patterns to PV hook events, except null events were characterized by a weaker surface cyclone, weaker midlevel frontogenesis, larger conditional and symmetric stability, and less coupling with upper-level forcing for ascent. The most robust (statistically significant) signal was a difference in midlevel frontogenesis intensity. In the minority of null cases that have very strong frontogenesis, the stability is generally large, while in the minority of banded events that have weak frontogenesis, the stability is generally small. This result highlights the basic coupled relationship between forcing and stability. However a scatter plot of frontogenesis and stability for banded and null events showed that there was overlap of data points in the frontogenesis−stability phase space, possibly highlighting the importance of other aspects, such as coupling of lower- and upper- level forcing for ascent.

The scatter plot results show that some cases may be clearly banded or nonbanded; however, other cases may be sensitive to the exact forcing magnitude, stability state, and front-jet coupling. Further evidence of this sensitivity is the result that differences between banded and null event 700-hPa temperature gradient and frontogenetical flow appear only ~2 h prior to band formation. This may suggest a “tipping point” in the positive feedback between LHR and increasing frontogenetical forcing just prior to band formation. Thus, forecasting techniques relying on precursor observational signals to distinguish banded and null events will have limited lead times.

5.3 Suggested future work

This thesis focused on precipitation bands within cyclones over the northeast U.S. A similar analysis of banded events in other geographical locations should be conducted. It is expected that the frontogenesis and stability evolutions found here will also be present in other regions, however, the synoptic environments and evolutions in which they develop may differ. For example, intense snowbands have been observed in the central U.S. ahead of short waves embedded within northwest synoptic flow (Banacos 2003; Berndt and Graves 2009).

This thesis has focused on the band ingredients of frontogenesis, weak moist symmetric stability, and moisture; however, Jurewicz and Evans (2004), Greenstein (2006), and Evans and Jurewicz (2009) also consider conditions favorable for the production of dendritic snow crystals to be a band ingredient, supported by early results from the CYCLES project (i.e., Fig. 1.3). Ascent within a vertical layer near −15°C favors the development of dendritic snow crystals (Rogers and Yau 1989), which may enhance precipitation efficiency (Auer and White 1982). Greenstein (2006) found that the intersection of maximum ascent with the dendritic growth zone was not a clear distinguishing factor in precipitation organization for 20 northeast heavy snow events. Further clarification as to whether and to what degree enhanced depositional growth affects band organization and intensity is needed. Numerical simulations augmenting the dependence of depositional rate on temperature may assist in this investigation.

It is also important to determine to what degree jet−front coupling can help distinguish between banded and null events, since this may assist in prediction. Hakim and Keyser (2001) have explored the impact of coupled and uncoupled ageostrophic circulations in an idealized framework utilizing Green's function solutions in three different synoptic scenarios (horizontally coupled jets, vertically coupled jet−front, vertically uncoupled jet−front system, their section 3). However, determination of the full phase space of coupling is needed. This may be accomplished in the same idealized framework by varying the static and inertial stability, vertical and horizontal separation distance between point forcing sources, and intensity of the upper and lower forcing.

Given the dataset of observed events and their evolution developed in this thesis, aspects of band predictability can be systematically investigated. For example, the hypothesis that band occurrence is more predictable than band timing and location can be tested by simulating the observed events with a mesoscale short-range ensemble system (e.g., Jones et al. 2007; Grimit and Mass 2002), and tracking errors in band occurrence, location, and timing through use of objective feature-based verification methods (e.g., Davis et al. 2006a,b). Based on this dataset, the current skill in predicting band occurrence, timing, and location can be established by varying the ensemble lead time for each event and measuring errors and biases.

One suspected model bias is an underprediction of precipitation during banding events, as detailed in the 25 Dec 2002 event (chapter 2) and others (e.g., Novak and Colle 2007). Besides inaccuracies in initial condition and model physics schemes, the failure of a model to simulate the release of CI, CSI or II may be a contributing factor to the underprediction. Persson and Warner (1993) have shown in an idealized setting that horizontal resolutions less than 15 km and vertical resolutions less than 170 m are required to resolve the most unstable CSI modes. Brennan and Lackmann (2006) have hypothesized that since parameterized convection schemes will fail to trigger with shallow elevated CI layers, an underprediction in precipitation may be expected. Thus, models run at convective-permitting scales may improve prediction, and this hypothesis should be tested by comparing convective-permitting simulations with parameterized simulations for multiple events.

Since the predictability of an atmospheric feature decreases as the scale of the feature decreases (Dalcher and Kalnay 1987; Droegemeier 1997), the predictability of mesoscale bands may be limited to relatively short time scales. For instance, Zhang et al. (2003) suggested that deterministic mesoscale precipitation forecasts are impractical beyond 2–3 days due to the upscale error growth associated with moist convective processes. The sensitivity of band evolution to the growth of diabatic PV anomalies shown in this thesis reinforces this assertion. While recognizing the predictability limits inherent to mesoscale bands, the emergence of conceptual models of band development, new observational datasets, and numerical weather prediction advances have allowed band prediction in an operational forecast setting at short-range projections (Novak et al. 2006). Preliminary investigation has shown that the predictability of banding events is case dependent (Novak and Colle 2007). Thus, a key question is why some cases are more predictable than others, and can this be known a-priori? For example, does band predictability vary between PV hook, cut off, and diabatic banded cyclone types?

Another question is whether band predictability can be related to the evolution of synoptic and mesoscale features, such as the details of the shortwave associated with the cyclone. Adjoint (e.g., Errico et al. 2003, Kleist and Morgan 2005) and ensemble sensitivity approaches (Torn and Hakim 2008) have been used to understand how aspects of a forecast are sensitive to initial conditions (e.g., Errico et al. 2003, Kleist and Morgan 2005), and these approaches could be applied to the mesoscale banding problem. Of practical interest is whether targeted observations optimized for mesoscale short-range prediction may improve band prediction.

Although this thesis focused on solitary bands, Novak et al. (2004) also documented multi-banded precipitation events over the northeast U.S. These events are defined as the occurrence of three or more finescale (5-20 km in width) bands with periodic spacing and similar spatial orientation, with intensities greater than 10 dBZ over the background reflectivity. This structure was commonly found ahead of the occluded front. Novak et al. (2004) noted 10 cases where finescale bands in the multiband structure merged with a pre-existing single band. The idealized modeling results of Xu (1992) suggest that the single- and multi-banded structures are differentiated by the moist stability, magnitude and areal extent of the frontogenesis, moisture availability, and eddy viscosity; however, observational and model validation of these results has not been accomplished. As observational and model datasets push towards finer scales, such validation may be feasible.

References

Auer, A. H., Jr., and J. M. White, 1982: The combined role of kinematics, thermodynamics, and cloud physics associated with heavy snowfall episodes. *J. Meteor. Soc. Japan*, **60**, 591–597.

Banacos, P. C., 2003: Short-range prediction of banded precipitation associated with deformation and frontogenesis forcing. Preprints, *10th Conf. on Mesoscale Processes,* Portland, OR, Amer. Meteor. Soc.

Baxter, M.A., and C. E. Graves, 2006: A case example of the role of warm-sector convection in the development of mesoscale banded snowfall: 2003 November 22–24. Preprints, *23rd Conf. on Svr. Local Storms,* St Louis, MO, Amer. Meteor. Soc., 4.6.

Benjamin, S. G., G. A. Grell, J. M. Brown, T. G. Smirnova, and R. Bleck, 2004: Mesoscale weather prediction with the RUC hybrid isentropic-terrain-following coordinate model. *Mon. Wea. Rev.*, **132**, 473–494.

Bennetts, D. A., and B. J. Hoskins, 1979: Conditional symmetric instability – A possible explanation for frontal rainbands. *Quart. J. Roy. Meteor. Soc.*, **105**, 945–962.

——, and J. C. Sharp, 1982: The relevance of conditional symmetric instability to the prediction of mesoscale frontal bands. *Quart. J. Roy. Meteor. Soc.,* **108,** 595–602.

Berndt, E. B., and C. E. Graves, 2009: The evolution of mesoscale ingredients that created an intense mesoscale snowband on 15 March 2004 in Des Moines, Iowa. *Electronic Journal of Operataional Meteorology*, 2009-EJ1.

Bluestein, 1993: *Synoptic-Dynamic Meteorology in Midlatitudes*. Vol. 2: Observations and Theory of Weather Systems, Oxford University Press, 594 pp.

Brennan, M. J., and G. M. Lackmann, 2005: The influence of incipient latent heat release on the precipitation distribution of the 24–25 January 2000 U.S. east coast cyclone. *Mon. Wea. Rev.*, **133**, 1913–1937.

——, and ——, 2006: Observational diagnosis and model forecast evaluation of unforecasted incipient precipitation during the 24-25 January 2000 east coast cyclone. *Mon. Wea. Rev.*, **134**, 2033–2054.

Carlson, T. N.,1991: *Mid-Latitude Weather Systems*. Harper Collins Academic, 507 pp.

——,1980: Airflow through midlatitude cyclones and the comma cloud pattern. *Mon. Wea. Rev.*, **108**, 1498–1509.

Cao, Z., and H.-R. Cho, 1995: Generation of moist potential vorticity in extratropical cyclones. *J. Atmos. Sci.*, **46**, 1119–1132.

Charney, J. G., 1955: The use of primitive equations of motion in numerical prediction. *Tellus*, **7**, 22–26.

Cho, H-R., and Z. Cao, 1998: Generation of moist potential vorticity in extratropical cyclones. Part II: Sensitivity to moisture distribution. *J. Atmos. Sci.*, **55**, 595–610.

Clark, J. H. E., R. P. James, and R. H. Grumm, 2002: A reexamination of the mechanisms responsible for banded precipitation. *Mon. Wea. Rev.*, **13**, 3074–3086.

Dalcher, A., and E. Kalnay, 1987: Error growth and predictability in operational ECMWF forecasts. *Tellus,* **39A**, 474–491.

Davies, H. C., 1999: Theories of Frontogenesis, *The Life Cycles of Extratropical Cyclones*, M. A. Shapiro and S. Gronas, Eds., Amer. Met. Soc., 215–238.

Davis, C. A., and K. A. Emanuel, 1991: Potential vorticity diagnostics of cyclogenesis. *Mon. Wea. Rev.*, **119**, 1929–1953.

——, 1992: A potential-vorticity diagnosis of the importance of initial structure and condensational heating in observed extratropical cyclogenesis. *Mon. Wea. Rev.*, **120**, 2409–2428.

——, B. Brown, and R. Bullock, 2006a: Object-based verification of precipitation forecasts. Part I: Methodology and application to mesoscale rain areas. *Mon. Wea. Rev.*, **134**, 1772–1784.

____, ____, and ____, 2006b: Object-based verification of precipitation forecasts. Part II: Application to convective rain systems. *Mon. Wea. Rev.*, **134**, 1785–1795.

Droegemeier, K. K., 1997: The numerical prediction of thunderstorms: Challenges, potential benefits, and results from real-time operational tests. *WMO Bulletin,* **46**, 324–336.

Dudhia, J., 1989: Numerical study of convection observed during the winter monsoon experiment using a mesoscale two-dimensional model. *J. Atmos. Sci.*, **46**, 3077–3107.

——, 1993: A nonhydrostatic version of the Penn State–NCAR mesoscale model: Validation tests and simulation of an Atlantic cyclone and cold front. *Mon. Wea. Rev.*, **121**, 1493–1513.

Eady, E., 1949: Long waves and cyclone waves. *Tellus*, **1**, 33–52.

Eliassen, A., 1962: On the vertical circulation in frontal zones. *Geofys. Publ.*, **24**, 147–160.

Emanuel, K. A., 1985: Frontal circulations in the presence of small moist symmetric stability. *J. Atmos. Sci.*, **42**, 1062–1071.

Errico, R. M., and T. Vukicevic, 1992: Sensitivity analysis using an adjoint of the PSU–NCAR mesoscale model. *Mon. Wea. Rev.,* **120,** 1644–1660.

Evans, M., and M. L. Jurewicz, Sr., 2009: Correlations between forecasts of banded snow ingredients and observed snowfall for a spectrum of snow events. *Wea. Forecasting*, **24**, 337–350.

Greenstein, M.D., 2006: Mesoscale structure of precipitation regions in northeast winter storms. M.S. thesis, University at Albany, State University of New York, 116 pp. [Available from Dept. of Earth and Atmospheric Sciences, University at Albany, State University of New York, Albany, NY 12222.]

Grell, G. A., 1993: Prognostic evaluation of assumptions used by cumulus parameterizations. *Mon. Wea. Rev.*, **121**, 764–787.

——, J. Dudhia, and D. R. Stauffer, 1995: A description of the fifth-generation PSU/NCAR Mesoscale Model (MM5). NCAR Tech. Note 398+STR, 117 pp.

Godson, W. L., 1951: Synoptic properties of frontal surfaces. *Quart. J. Roy. Meteor. Soc.,* **77,** 633–653.

Grim, J.A., R. M. Rauber, M. K. Ramamurthy, B. F. Jewett, and J. A. Grim, 2007: High-resolution observations of the trowal–warm-frontal region of two continental winter cyclones. *Mon. Wea. Rev.*, **135**, 1629–1646.

Grimit, E. P., and C. F. Mass, 2002: Initial results of a mesoscale short-range ensemble forecasting system over the Pacific Northwest. *Wea. Forecasting*, **17**, 192–205.

Gutman, S. I., S. R. Sahm, S. G. Benjamin, B. E. Schwartz, K. L. Holub, J. Q. Stewart, and T. L. Smith, 2004: Rapid retrieval and assimilation of ground based GPS precipitable water observations at the NOAA Forecast Systems Laboratory: Impact on weather forecasts. *J. Meteor. Soc. of Japan*, **82**, 1–10.

Gyakum, J. R., P. J. Roebber, and T. A. Bullock, 1992: The role of antecedent surface vorticity development as a conditioning process in explosive cyclogenesis. *Mon. Wea. Rev.*, **120**, 1465–1489.

Hakim, G. J., and D. Keyser, 2001: Canonical frontal circulation patterns in terms of Green's functions for the Sawyer–Eliassen equation. *Quart. J. Roy. Meteor. Soc.*, **127**, 1795–1814.

——, D. Keyser, and L. F. Bosart, 1996: The Ohio Valley wave-merger cyclogenesis event of 25–26 January 1978. Part II: Diagnosis using quasigeostrophic potential vorticity inversion. *Mon. Wea. Rev.*, **124**, 2176–2205.

Han, M., R. M. Rauber, M. K. Ramamurthy, B. F. Jewett, and J. A. Grim, 2007: Mesoscale dynamics of the trowal and warm-frontal regions of two continental winter cyclones. *Mon. Wea. Rev.*, **135**, 1647–1670.

Hobbs, P. V., 1978: Organization and structure of clouds and precipitation on the mesoscale and microscale in cyclonic storms. *Rev. of Geophys. and Space Phys*., **16**, 741–755.

——, T. J. Matejka, P. H. Herzegh, J. D. Locatelli, and R. A. Houze, Jr., 1980: The mesoscale and microscale structure and organization of clouds and precipitation in midlatitude cyclones. I: A case study of a cold front. *J. Atmos. Sci.*, **37**, 568–596.

——, J. D. Locatelli, and J. E. Martin, 1990: Cold fronts aloft and the forecasting of precipitation and severe weather east of the Rocky Mountains. *Wea. Forecasting*, **5**, 613-626.

Holt, M. W., and A. J. Thorpe, 1991: Localized forcing of slantwise motion at fronts. *Quart. J. Roy. Meteor. Soc.*, **117**, 943–963.

Hong, S.-Y. and H.-L. Pan, 1996: Nonlocal boundary layer vertical diffusion in a medium-range forecast model. *Mon. Wea. Rev.*, **124**, 2322–2339.

——, J. Dudhia, and S-H Chen, 2004: A Revised Approach to Ice Microphysical Processes for the Bulk Parameterization of Clouds and Precipitation. *Monthly Weather Review*, **132**, 103–120.

Hoskins, B. J., 1974: The role of potential vorticity in symmetric stability and instability. *Quart. J. Roy. Meteor. Soc.*, **100**, 480–482.

Hoskins, B. J., M. E. McIntyre, and A. W. Robertson, 1985: On the use and significance of isentropic potential vorticity maps. *Quart. J. Roy. Meteor. Soc.*, **111**, 877–946.

Houze, R. A. Jr., P. V. Hobbs, K. R. Biswas, and W. M. Davis, 1976: Mesoscale rainbands in extratropical cyclones. *Mon. Wea. Rev.*, **104**, 868–879.

——, S. A. Rutledge, T. J. Matejka, and P. V. Hobbs, 1981: The mesoscale and microscale structure and organization of clouds and precipitation in midlatitude cyclones. I: Air motions and precipitation growth in a warm-frontal rainband. *J. Atmos. Sci.*, **38**, 639–649.

Jascourt, S. D., S. S. Lindstrom, C. J. Seman, and D. D. Houghton, 1988: An observation of banded convective development in the presence of weak symmetric stability. *Mon. Wea. Rev.*, **116**, 175–191.

Jones, M.S., B. A. Colle, and J. S. Tongue, 2007: Evaluation of a mesoscale short-range ensemble forecast system over the northeast United States. *Wea. Forecasting*, **22**, 36–55.

Jurewicz, M. L., and M. S. Evans, 2004: A comparison of two banded, heavy snowstorms with very different synoptic settings. *Wea. Forecasting*, **19**, 1011–1028.

Keyser, D., B. D. Schmidt, and D. G. Duffy, 1992: Quasigeostrophic vertical motions diagnosed from along- and cross-isentrope components of the Q vector. *Mon. Wea. Rev.*, **120**, 731–741.

Klazura, G. E., and D. A. Imy, 1993: A description of the initial set of analysis products available from the NEXRAD WSR-88D system. *Bull. Amer. Meteor. Soc.*, **74**, 1293–1311.

Kleist, D. T., and M. Morgan, 2005: Application of adjoint-derived forecast sensitivities to the 24-25 January 2000 U.S. east coast snowstorm. *Mon. Wea. Rev.*, **133**, 3148–3175.

Knight, D. J., and P. V. Hobbs, 1988: The mesoscale and microscale structure and organization of clouds and precipitation in midlatitude cyclones. I: Air motions and precipitation growth in a warm-frontal rainband. *J. Atmos. Sci.*, **45**, 915–930.

Koch, S. E., B. Ferrier, M. T. Stoelinga, E. Szoke, S. J. Weiss, and J. S. Kain, 2005: The use of simulated radar reflectivity fields in the diagnosis of mesoscale phenomena from high-resolution WRF model forecasts. *32nd Radar Meteorology Conference*, Albuquerque, New Mexico, CD-ROM, J4J.7.

Kocin, P. J., and L. W. Uccellini: Northeast Snowstorms. Volume 1: Overview. Meteor. Monogr., No. 54, Amer. Meteor. Soc., 296 pp.

Korner, S. O., and J. E. Martin, 2000: Piecewise frontogenesis from a potential vorticity perspective: Methodology and a case study. *Mon. Wea. Rev.*, **128**, 1266–1288.

Leise, J. A., 1982: A multidimensional scale-telescoped filter and data extension package. NOAA Tech Memo. ERL WPL-82, 19 pp.

Martin, J. E., 1998a: The structure and evolution of a continental winter cyclone. Part I: Frontal structure and the occlusion process. *Mon. Wea. Rev.*, **126**, 303–328.

——,1998b: The structure and evolution of a continental winter cyclone. Part II: Frontal forcing of an extreme snow event. *Mon. Wea. Rev.*, **126**, 329–348.

——,1999: Quasigeostrophic forcing of ascent in the occluded sector of cyclones and the trowal airstream. *Mon. Wea. Rev*., **127**, 70–88.

McTaggart-Cowan, R., E. H. Atallah, J. R. Gyakum, and L. F. Bosart, 2006: Hurricane Juan (2003). Part I: A diagnostic and compositing life cycle study. *Mon. Wea. Rev.*, **134**, 1725–1747.

Mesinger, F., and CoAuthors, 2006: North American regional reanalysis. *Bull. Amer. Soc.*, **87**, 343–360.

Michalakes, J., S. Chen, J. Dudhia, L. Hart, J. Klemp, J. Middlecoff, and W. Skamarock, 2001: Development of a next generation regional weather research and forecast model. *Developments in Teracomputing: Proceedings of the Ninth ECMWF Workshop on the Use of High Performance Computing in Meteorology,* W. Zwieflhofer and N. Kreitz, Eds., World Scientific, Singapore, 269–276.

Miller, J. E., 1946: Cyclogenesis in the Atlantic coastal region of the United States. *J. Meteor.* **3**, 31–44.

Mohr, C. G., L. J. Miller, R. L. Vaughn, and H. W. Frank, 1986: The merger of mesoscale datasets into a common Cartesian format for efficient and systematic analysis. *J. Atmos. Oceanic Technol.,* **3**, 143–161.

Moninger, W. R., R. D. Mamrosh, and P. M. Pauley, 2003: Automated meteorological reports from commercial aircraft. *Bull. Amer. Meteor. Soc*., **84**, 203–216.

Montgomery, M. T., and B. F. Farrell, 1991: Moist surface frontogenesis associated with interior potential vorticity anomalies in a semigeostrophic model. *J. Atmos. Sci*., **48**, 343–363.

Moore, J. T., C. E. Graves, S. Ng, and J. L. Smith, 2005: A process-oriented methodology toward understanding the organization of an extensive mesoscale snowband: A diagnostic case study of 4–5 December 1999. *Wea. Forecasting*, **20,** 35–50.

Moore, R. W., and M. T. Montgomery, 2004: Reexamining the dynamics of short-scale, diabatic rossby waves and their role in midlatitude moist cyclogenesis. *J. Atmos. Sci*., **61**, 754–768.

——, M. T. Montgomery, and H. C. Davies, 2008: The integral role of a diabatic rossby vortex in a heavy snowfall event. *Mon. Wea. Rev*., **136**, 1878–1897.

Morales, R. F., 2008: The historic Christmas 2004 south Texas snow event: Diagnosis of the heavy snow band. Natl. Wea. Dig., **32** (2), 135–152.

Morgan, M. C., 1999: Using piecewise potential vorticity inversion to diagnose frontogenesis. Part I: A partitioning of the Q vector applied to diagnosing surface frontogenesis and vertical motion. *Mon. Wea. Rev.*, **127**, 2796–2821.

Morcrette, C. J. and K. A. Browning, 2006: Formation and release of symmetric instability following Delta-M adjustment. *Quart. J. Roy. Meteor. Soc.*, **132**, 1073–1089.

NCAR, cited 2005: PSU/NCAR Mesoscale Modeling System Tutorial Class Notes and User's Guide: MM5 Modeling System Version 3. http://www.mmm.ucar.edu/mm5/documents/MM5_tut_Web_notes/MM5/mm5.htm

Nielsen-Gammon, J. W., and R. J. Lefevre, 1996: Piecewise tendency diagnosis of dynamical processes governing the development of an upper-tropospheric mobile trough. *J. Atmos. Sci.*, **53**, 3120–3142.

Nicosia, D. J., and R. H. Grumm, 1999: Mesoscale band formation in three major northeastern United States snowstorms. *Wea. Forecasting*, **14**, 346–368.

NOAA, 2002–2008: Daily weather maps weekly series. Washington D.C. GPO.

Novak, D. R., L. F. Bosart, D. Keyser, and J. S. Waldstreicher, 2004: An observational study of cold season-banded precipitation in northeast U.S. cyclones. *Wea. Forecasting*, **19**, 993–1010.

——, J. S. Waldstreicher, D. Keyser, and L. F. Bosart, 2006: A forecast strategy for anticipating cold season mesoscale band formation within eastern U.S. cyclones. *Wea. Forecasting*, **21**, 3–23.

——, B. A. Colle, 2005: Comparison of MM5 and WRF forecasts of the 25 December 2002 northeast U.S. banded snowstorm. *6th WRF / 15th MM5 User's Workshop,* 1.4.

——, and ——, 2007a: Assessing the predictability of band formation and evolution during three recent northeast U.S. snowstorms. Preprints, *22nd Conf. on Weather Analysis and Forecasting/18th Conf. on Numerical Weather Prediction,* Park City, U.T., Amer. Meteor. Soc.

——, ——,, and S. E. Yuter, 2007b: A high-resolution observational and modeling comparison of mesoscale band life cycle during three recent northeast U.S. snowstorms. Preprints, *22nd Conf. on Weather Analysis and Forecasting/18th Conf. on Numerical Weather Prediction,* Park City, U.T., Amer. Meteor. Soc.

Persson, P. O. G., and T. T. Warner, 1993: Nonlinear hydrostatic conditional symmetric instability: Implications for numerical weather prediction. *Mon. Wea. Rev.*, **121**, 1821–1833.

——, and ——, 1995: The nonlinear evolution of idealized, unforced, conditional symmetric instability: A numerical study. *J. Atmos. Sci*, **52**, 3449–3474.

Petterssen, S., 1936: Contribution to the theory of frontogenesis. *Geophys. Publ.*, **11** (6), 1–27.

Posselt, D. J., and J. E. Martin, 2004: The effect of latent heat release on the evolution of a warm occluded thermal structure. *Mon. Wea. Rev.*, **132**, 578–599.

Ralph, M. F. and CoAuthors, 2005: Improving short-term (0-48 h) cool-season quantitative precipitation forecasting. Recommendations from a USWRP workshop. *Bull. Amer. Soc*., **86**, 1619–1632.

Raymond, D. J., 1992: Nonlinear balance and potential-vorticity thinking at large Rossby number. *Quart. J. Roy. Meteor. Soc.*, **118**, 987–1015.

——, and H. Jiang, 1990: A theory for long-lived mesoscale convective systems. J. Atmos. Sci., **47**, 3067–3077.

Reed, R. J., and Y. –H. Kuo, 1988: Numerical simulations of an explosively deepening cyclone in the eastern Pacific. Mon. Wea. Rev., **116**, 2081–2105.

Reuter, G. W., and M. K. Yau, 1990: Observations of slantwise convective instability in winter cyclones. *Mon. Wea. Rev*., **118**, 447–458.

Roebber, P. J., S. L. Bruening, D. M. Schultz, and J. V. Cortinas Jr., 2003: Improving snowfall forecasting by diagnosing snow density. *Wea. Forecasting*, **18**, 264–287.

Rogers, E., T. Black, B. Ferrier, Y. Lin, D. Parrish, and G. DiMego, 2001: Changes to the NCEP Meso Eta Analysis and Forecast System: Increase in resolution, new cloud microphysics, modified precipitation assimilation, modified 3DVAR analysis. NOAA/NWS Technical Procedures Bulletin 488. [Available at: http://www.emc.ncep.noaa.gov/mmb/mmbpll/eta12tpb/. Also available from National Weather Service, Office of Climate, Water, and Weather Services, 1325 East-West Highway, Silver Spring, MD 20910.]

Rogers, R. R., and M. K. Yau, 1989: *A Short Course in Cloud Physics*. Pergammon Press, 293 pp.

Rutledge, S. A., and P. V. Hobbs, 1983: The mesoscale and microscale structure and organization of clouds and precipitation in midlatitude cyclones. VIII: A model for the “Seeder-Feeder” process in warm-frontal rainbands. *J. Atmos. Sci.*, **40**, 1185–1206.

Sanders, F., and L. F. Bosart, 1985: Mesoscale structure in the megalopolitan snowstorm of 11–12 February 1983. Part I: Frontogenetical forcing and symmetric instability. *J. Atmos. Sci*., **42**, 1050–1061.

——, 1986: Frontogenesis and symmetric stability in a major New England snowstorm. *Mon. Wea. Rev*., **114**, 1847–1862.

Sawyer, J. S., 1956: The vertical circulation at meteorological fronts and its relation to frontogenesis. *Proc. Roy. Soc. London*, **A234**, 346–362.

Schultz, D. M., D. Keyser, and L. F. Bosart, 1998: The effect of large-scale flow on low-level frontal structure and evolution in midlatitude cyclones. *Mon. Wea. Rev.*, **126**, 1767–1791.

——, D. M., and P. N. Schumacher, 1999: The use and misuse of conditional symmetric instability. *Mon. Wea. Rev*., **127**, 2709–2732; Corrigendum, **128**, 1573.

——, 2001: Reexamining the cold conveyor belt. *Mon. Wea. Rev.*, **129**, 2205–2225.

——, D. M., 2004: Cold fronts with and without prefrontal wind shifts in the central United States. *Mon. Wea. Rev.*, **132**, 2040–2053.

——, and J .A. Knox, 2007: Banded convection caused by frontogenesis in a conditionally, symmetrically, and inertially unstable environment. *Mon. Wea. Rev*., **135**, 2095–2110.

Shapiro, M. A., 1982: Mesoscale weather systems of the central United States. CIRES/NOAA Tech.1 Rep., University of Colorado, 78 pp.

Stensrud and CoAuthors, 2006: The New England high-resolution temperature program. *Bull. Amer. Soc*., **87**, 491–498.

Stewart, R. E., 1991: Canadian Atlantic Storms Program: Progress and plans of the meteorological component. *Bull. Amer. Meteor. Soc.*, **56**, 364–371.

Stoelinga, M. T., 1996: A potential vorticity-based study of the role of diabatic heating and friction in a numerically simulated baroclinic cyclone. *Mon. Wea. Rev.*, **124**, 849–874.

Stuart, N.A., R. H. Grumm, 2006: Using wind anomalies to forecast east coast winter storms. *Wea. Forecasting*, **21**, 952–968.

Thorncroft, C. D., B. J. Hoskins, and M. E. McIntyre, 1993: Two paradigms of baroclinic-wave life-cycle behavior. *Quart. J. Roy. Meteorol. Soc.*, **119**, 17–55.

Thorpe, A. J., and K.A. Emanuel, 1985: Frontogenesis in the presence of small stability to slantwise convection. *J. Atmos. Sci.*, **42**, 1809–1824.

——, and S. A. Clough, 1991: Mesoscale dynamics of cold fronts: Structures described by dropsoundings in FRONTS 87. *Quart. J. Roy. Meteor. Soc.*, **117**, 903–941.

Torn, R. D., and G. J. Hakim, 2008: Ensemble-based sensitivity analysis. *Mon. Wea. Rev.*, **136**, 663–677.

Wernli, H. S., S. Dirren, M. A. Liniger, and M. Zillig, 2002: Dynamical aspects of the life cycle of the winter storm 'Lothar' (24-26 December 1999). *Quart. J. Roy. Meteorol. Soc.*, **128**, 405–429.

Wetzel, S. W., and J. E. Martin, 2001: An operational ingredients-based methodology for forecasting midlatitude winter season precipitation. *Wea. Forecasting*, **16**, 156–167.

Wexler, R., and D. Atlas, 1959: Precipitation generating cells. *J. Atmos. Sci.*, **16**, 327–332.

Weisman, A., K. G. McGregor, D. R. Novak, J. L. Selzler, M. L. Spinar, and B. C. Thomas, 2002: Precipitation regimes during cold-season central U.S. inverted trough cases. Part I: Synoptic climatology and composite study. *Wea. Forecasting*, **17**, 1173–1193

Wiesmueller, J. L., and S. M. Zubrick, 1998: Evaluation and application of conditional symmetric instability, equivalent potential vorticity, and frontogenetical forcing in an operational forecasting environment. *Wea. Forecasting*, **13**, 84–101.

Wilks, D. S., 1995: *Statstical Methods in the Atmospheric Sciences: An Introduction.* Academic Press, 467 pp.

Xu, Q., 1989a: Extended Sawyer–Eliassen equation for frontal circulations in the presence of small viscous moist symmetric stability. *J. Atmos. Sci.*, **46**, 2671–2683.

——, 1989b: Frontal circulations in the presence of small viscous moist symmetric stability and weak forcing. *Quart. J. Roy. Meteor. Soc.*, **115**, 1325–1353.

——, 1992: Formation and evolution of frontal rainbands and geostrophic potential vorticity anomalies. *J. Atmos. Sci.*, **49**, 629–648.

Yuter, S. E., and Houze, R. A. Jr., 1995: Three-Dimensional kinematic and microphysical evolution of Florida cumulonimbus. Part I: Spatial distribution of updrafts, downdrafts, and precipitation. *Mon. Wea. Rev.*, **123**, 1921–1940.

Zhang, F., C. Synder, R. Rotunno, 2003: Effects of moist convection on mesoscale predictability. *J. Atmos. Sci.*, **60**, 1173–1185.

——, N. Bei, R. Rotunno, C. Snyder, and C. C. Epifanio, 2007: Mesoscale Predictability of Moist Baroclinic Waves: Convection-Permitting Experiments and Multistage Error Growth Dynamics. *J. Atmos. Sci.*, **64**, 3579–3594.

Zwiers, F.W., 1990: The effect of serial correlation on statistical inferences made with resampling procedures. *J. Climate*, **3**, 1452–1461.